

IONIZING RADIATION DETECTOR FOR ENVIRONMENTAL  
AWARENESS IN FPGA-BASED FLIGHT COMPUTERS

by

Todd Michael Buerkle

A thesis submitted in partial fulfillment  
of the requirements for the degree

of

Master of Science

in

Electrical Engineering

MONTANA STATE UNIVERSITY  
Bozeman, Montana

April 2012

©COPYRIGHT

by

Todd Michael Buerkle

2012

All Rights Reserved

APPROVAL

of a thesis submitted by

Todd Michael Buerkle

This thesis has been read by each member of the thesis committee and has been found to be satisfactory regarding content, English usage, format, citation, bibliographic style, and consistency and is ready for submission to The Graduate School.

Dr. Todd J. Kaiser

Approved for the Department of Electrical and Computer Engineering

Dr. Robert C. Maher

Approved for The Graduate School

Dr. Carl A. Fox

STATEMENT OF PERMISSION TO USE

In presenting this thesis in partial fulfillment of the requirements for a master's degree at Montana State University, I agree that the Library shall make it available to borrowers under rules of the Library.

If I have indicated my intention to copyright this thesis by including a copyright notice page, copying is allowable only for scholarly purposes, consistent with "fair use" as prescribed in the U.S. Copyright Law. Requests for permission for extended quotation from or reproduction of this thesis in whole or in parts may be granted only by the copyright holder.

Todd Michael Buerkle

April 2012

## ACKNOWLEDGEMENTS

I would like to take the time to thank all of the people that made this project possible. Firstly I want to thank my co-advisors Dr. Todd Kaiser and Dr. Brock LaMeres for selecting me to work on this project and the countless hours of help they have provided over the past few years. I also want to thank my other committee member Andy Olson for his guidance on this project. I have had a great deal of help from other graduate students during this research and I want to thank Justin Hogan, Jennifer Hane, and Ray Weber for their assistance with many aspects of this project. My family and friends have been invaluable during my graduate studies. I want to thank them for their continued love and support throughout my studies and heading into my new career. I also want to thank my fiancée Lindsay Vennes for her support and encouragement and for all of her patience with me during the course of this project. She helped keep me grounded during the last two years. Finally, I want to thank NASA for their financial contribution to this project as part of an EPSCOR grant. Without this, none of this work would have been possible.

## TABLE OF CONTENTS

1. INTRODUCTION TO COMPUTING IN SPACE .....	1
Introduction .....	1
Effects of Radiation on Digital Electronics .....	1
Improving Fault Tolerance in Aerospace Computing .....	3
Proposed Fault Tolerant Computing Solution.....	5
Many Tile Computer Architecture.....	5
Spatial Ionizing Radiation Sensor.....	7
Integration of Radiation Sensor with Many Tile Computer Architecture.....	8
Improvements over Current Designs .....	9
Thesis Overview .....	9
2. SILICON BASED RADIATION SENSORS .....	11
Current Designs Utilizing Radiation Sensors.....	11
Previous Radiation Sensor Designs Completed at MSU .....	12
Generation 1: Single Sided Sensor .....	13
Generation 2: Double Sided Sensor .....	15
Generation 3: Commercial Sensor .....	16
Generation 4: Double Sided Strip Sensor with Back Barrier Diffusions.....	19
3. SPATIAL RADIATION SENSOR SYSTEM DESIGN .....	22
Generation 5: Double Sided Strip Sensor with Front and Back Barrier Diffusions.....	22
Sensor Theory of Operation and Design .....	22
Radiation Sensor Performance Modeling .....	26
Amplifier Board.....	32
Electronic Circuitry Design.....	32
High Speed Event Detector Design .....	36
4. SPATIAL RADIATION SENSOR SYSTEM FABRICATION .....	40
Generation 5: Double Sided Strip Sensor with Front and Back Barrier Diffusions.....	40
Fabrication Process .....	41
Calculating Sensor Parameters .....	46
Simulated Heavy Ion Strike.....	48
Radiation Sensor Package Fabrication.....	53
Amplifier Board Implementation .....	55
Component Selection .....	55
Amplifier Board Fabrication .....	57
Additional PCB Designs .....	59

## TABLE OF CONTENTS – CONTINUED

High Speed Event Detector Implementation.....	61
5. RADIATION TESTING.....	63
Cyclotron Testing at Texas A&M University .....	63
Correlating Measured Data and the Developed Radiation Sensor Model .....	75
6. CONCLUSION AND RECOMMENDATIONS FOR FUTURE WORK.....	112
Conclusion.....	112
Recommendations for Future Work .....	113
REFERENCES CITED .....	115
APPENDICES.....	118
APPENDIX A: Radiation Sensor Fabrication Process .....	119
APPENDIX B: Cyclotron Testing Beam Parameters .....	128
APPENDIX C: SRIM Output Text File Example .....	130
APPENDIX D: Test Run Data .....	136
APPENDIX E: Radiation Testing Plots.....	156

## LIST OF TABLES

Table	Page
1. Depletion Widths Calculations .....	47
2. Sensor Current Calculations .....	51
3. Event Detector Performance Metrics .....	62
4. Amplifier Board Gains .....	64
5. Average Counts per Second for Test #7.....	68
6. Average Counts per Second for Test #2.....	71
7. Average Counts per Second for Test #8.....	73
8. Effective Particle Fluences for Tests 2, 7, and 8 .....	74
9. Output Pulse Widths for Front and Back Side Electronics for a Single Krypton Ion Strike .....	85
10. Calculation of the Ion Density for Test #2 .....	89
11. Ion Densities .....	90
12. Overlap Areas .....	93
13. Ion Counts for Test #2.....	94
14. Ion Counts for Test #7.....	95
15. Ion Counts for Test #8.....	95
16. Counts for Test #7.....	97
17. Counts for Test #2.....	97
18. Counts for Test #8.....	98
19. Front Side Predicted Versus Measured Counts for All Three Tests.....	99

LIST OF TABLES - CONTINUED

Table	Page
20. Back Side Predicted Versus Measured Counts for All Three Tests .....	100
21. Average Counts per Second for Test #19.....	106
22. Predicted Versus Measured Counts for Test #19.....	108

## LIST OF FIGURES

Figure	Page
1.1. Interaction of a Radiation Particle and Silicon .....	3
1.2. FPGA Reconfigurable Tiles.....	6
2.1. Cross Section of Generation 1 Sensor.....	13
2.2. Testing of Generation 1 Sensor.....	14
2.3. Cross Section of Generation 2 Sensor.....	15
2.4. Packaged Generation 2 Sensor.....	16
2.5. Cross Section of the Commercial Sensor .....	17
2.6. Cross Section of the Biasing Scheme.....	18
2.7. Commercial Sensor Testing.....	18
2.8. Commercial Sensor Picture .....	19
2.9. Cross Section of the Generation 4 Sensor .....	20
2.10. Generation 4 Testing .....	21
3.1. Fundamental Sensing Element (PN) .....	23
3.2. PN Junction at Equilibrium .....	25
3.3. Amplifier Chain Schematic .....	35
3.4. Event Detector Schematic.....	39
4.1. Fabrication Process Cross Sections.....	43
4.2. Cross Section of Fabricated Generation 5 Sensor.....	46
4.3. Radiation Sensors at the Full Wafer Level.....	46
4.4. Depletion Region Diagram .....	49

LIST OF FIGURES - CONTINUED

Figure	Page
4.5. LET vs. Range in Silicon for 25 MeV Kr Ion .....	50
4.6. Charge vs. Range in Silicon for 25 MeV Kr Ion .....	52
4.7. Hole Current Produced by a 25 MeV Kr Ion.....	53
4.8. Electron Current Produced by a 25 MeV Kr Ion .....	54
4.9. Radiation Sensor Package Board .....	55
4.10. Packaged Radiation Sensor.....	56
4.11. Amplifier Chain Schematic with Component Values .....	58
4.12. Amplifier Board .....	59
4.13. Amplifier Board with Components Loaded.....	59
4.14. Power Board.....	60
4.15. Voltage Translator Board .....	61
4.16. Radiation Sensor System Stack.....	62
4.17. FPGA Board.....	63
5.1. Large Aperture Testing Locations .....	67
5.2. Small Aperture Testing Locations .....	67
5.3. Radiation Test Data for Test #7 .....	68
5.4. Radiation Test Data for Test #2 .....	71
5.5 Radiation Test Data for Test #8 .....	73
5.6. Charge vs. Range in Silicon for 21.8 MeV Kr Ion .....	77
5.7. Hole Current Produced by a 21.8 MeV Kr Ion.....	77

## LIST OF FIGURES - CONTINUED

Figure	Page
5.8. Electron Current Produced by a 21.8 MeV Kr Ion .....	78
5.9. DxDesigner Simulation Schematic .....	79
5.10. Front Side, Low Gain Simulation Results .....	81
5.11. Front Side, Medium Gain Simulation Results .....	82
5.12. Front Side, High Gain Simulation Results .....	83
5.13. Back Side, Low Gain Simulation Results .....	84
5.14. Back Side, Medium Gain Simulation Results.....	85
5.15. Back Side, High Gain Simulation Results .....	86
5.16. Ion Density .....	88
5.17. Beam Line Detector Arrangement .....	91
5.18. Beam Spot Centered on a Strip for the Large Aperture .....	93
5.19. Beam Spot Centered on a Gap for the Large Aperture .....	94
5.20. Front Side Measured vs. Predicted for Test #7 .....	103
5.21. Front Side Measured vs. Predicted for Test #2.....	104
5.22. Front Side Measured vs. Predicted for Test #8.....	104
5.23. Back Side Measured vs. Predicted for Test #7 .....	105
5.24. Back Side Measured vs. Predicted for Test #2 .....	105
5.25. Back Side Measured vs. Predicted for Test #8 .....	106
5.26. Radiation Test Data for Test #19 .....	107
5.27. Beam Spot Locations for the Small Aperture.....	107

LIST OF FIGURES - CONTINUED

Figure	Page
5.28. Front Side Measured vs. Predicted for Test #19 .....	110
5.29. Back Side Measured vs. Predicted for Test #19 .....	110

## ABSTRACT

Ionizing radiation has a detrimental effect on digital electronics that operate in extraterrestrial environments. When electronics are struck by these high energy particles, the effect on the system can range from temporary faults to permanent damage. Modern reconfigurable digital designs are using new architectures which can utilize environmental awareness to increase the system's tolerance to faults caused by radiation strikes. These digital fabrics are capable of reprogramming circuitry based on information provided to the system by an external source. In this thesis the design, modeling, and characterization of a radiation sensor is presented. This radiation sensor is coupled with an FPGA based reprogrammable computer system to provide spatial information about radiation events to the computer. The radiation sensor uses a PN junction as its fundamental sensing element. As a high energy radiation particle passes through the sensor, the substrate is ionized (electron-hole-pairs are generated). The internal electric field of the PN junction separates these charge carriers which are then collected on the orthogonally placed electrodes on the top and bottom of the sensor. This XY grid of electrodes provides the spatial location of an ionizing radiation strike. These coordinates are then input into the computer system which analyzes the location and reconfigures the system to avoid the potentially damaged circuitry located at the strike coordinates. A high speed event detector is also implemented in the FPGA to aide in the sampling and storing of the incoming radiation strikes. This event detector samples the incoming data at a high rate to ensure that even fast output pulses are detected by the computer system. A model was developed to predict the response of this radiation sensor for a given radiation source. This model was used to predict the signals out of the top and bottom electrodes on the radiation sensor. Extensive testing was then performed using a high energy radiation source. The sensor was able to determine the location of the radiation strike and relay this information to the computer system. The model was also capable of predicting the sensor response with the desired degree of accuracy.

## CHAPTER ONE – INTRODUCTION TO COMPUTING IN SPACE

### Introduction

In the past few decades, the amount of electrical systems in space has greatly increased. These systems utilize a range of circuitry to accomplish many different tasks. The harshness of the space environment often makes these tasks difficult to complete accurately. One reason for this is the presence of high energy radiation particles such as protons, neutrons and heavy ions. These particles have the potential to cause temporary errors or permanent damage in the electrical systems. The effect of these particles on terrestrial electronics is limited by the shielding produced by Earth's magnetic field. In space, this field is absent and these particles are able to move freely. This inevitably leads to the collision of one of these high energy particles with some part of an electrical system in space. The effect of this collision is the greatest when the particle collides with a semiconductor based digital integrated circuit.

### Effects of Radiation on Digital Electronics

In many instances, the collision of a radiation particle with an integrated circuit (IC) does not produce a negative effect. If the energy of the incident particle is high enough or a certain location of the IC is struck, the result can be detrimental to the correct operation of the system. As the particle passes through the semiconductor, it ionizes the material, producing electron-hole-pairs. The result of this ionization is generally classified into two types of effects. These effects are distinguished by the outcome

produced in the device. Total Ionizing Dose (TID) results in permanent damage to the device and Single Event Effects (SEE) produce transient results that cause temporary errors and failures but no permanent damage [1,2].

The Total Ionizing Dose damage results when either electrons or holes become trapped in the bulk substrate or the dielectric material of an integrated circuit. After the creation of an electron-hole-pair, these two reciprocal charges try to recombine in order to return the material to equilibrium. Manufacturing imperfections and other variables such as the difference in electron and hole mobility can prevent these particles from recombining, leading these charge carriers to become trapped in an oxide layer within a particular device. Without the annihilation of these electrons and holes, an excess of charge can build up in the semiconductor material causing threshold voltage shifts, increased leakage currents, and degraded switching performance [3]. These effects could result in transistors always being turned on and a greatly increased power draw. Changes such as these compromise the performance of the device and result in permanent damage.

Single Event Effects are produced by high energy particles that ionize the substrate of individual devices. An example of this ionization is illustrated in Figure 1.1. This ionization produces free charge in or near the depletion region of the device. If enough charge is generated, the resultant current flow can produce an output that can be interpreted as a state change. Single Event Effects of this nature are also known as Single Event Transients (SET) due to the temporary nature of these effects. The state change produced during a Single Event Transient may be latched into a storage device in some cases. This logical fault is known as a Single Event Upset in the system. Single Event

Effects produce temporary logical faults and no permanent damage, but the errors produced by these effects are still detrimental to the performance of the system. Due to the critical failures that can be produced by these effects, many different strategies have been implemented to mitigate them.

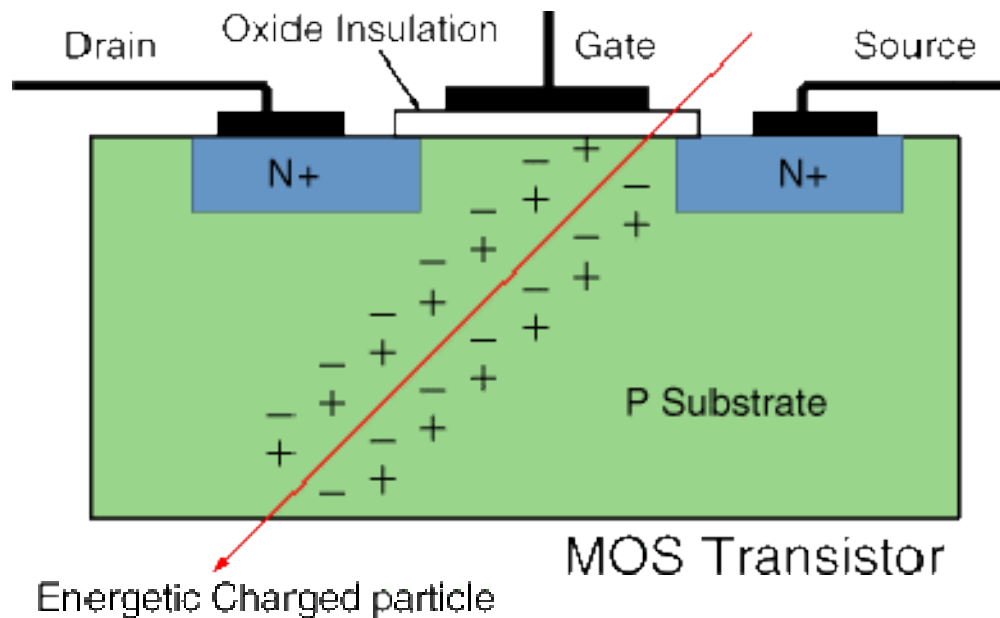


Figure 1.1 Example of the ionization of a transistor substrate [4].

### Improving Fault Tolerance in Aerospace Computing

The previously discussed faults both result from different effects produced by the ionization of a material by a high energy particle. For this reason, the methods employed to protect against and eliminate these effects are drastically different. One difficulty encountered when trying to mitigate TID effect is that devices are always vulnerable to this damage. Devices that are in use are just as likely to experience TID effects as are

devices that are inactive. This shows one major difference between TID and SEE and leads to the differences in how these failures are mitigated.

Mitigation of faults caused by TID usually involves implementing some form of shielding or altering the packaging of the device. This reduces the amount of charge that becomes trapped in the device. In other cases, the devices are redesigned so that they can still operate correctly in spite of the damage caused by TID. In this method, the lifetime damage of the device is predicted, and the component is redesigned so that correct operation is still achieved until this threshold is reached [3]. These mitigation strategies are some of the current approaches being employed to eliminate TID failures, but the approach used may change greatly depending on the application of the device.

Mitigation strategies for SEE are quite different than those used for TID. One of the more common approaches used involves implementing reconfigurable computing for fault mitigation. This strategy involves dynamically reconfiguring the computing system while still maintaining normal operation. The use of Field Programmable Gate Arrays (FPGAs) as the computing hardware allows for this dynamic reconfiguration. Real time reconfiguration enables the system to eliminate faults caused by SEE by reprogramming faulted circuits to a pre-fault state. Another strategy for limiting SEE involves the development of a computer architecture that contains extra, redundant circuits or tiles. This many tile system can then be reconfigured to remove faulted circuitry and activate an identical spare. Using these approaches and other similar methods, fault tolerance can be implemented for many different designs.

### Proposed Fault Tolerant Computing Solution

The solution utilized in this research to improve fault tolerance is a hybrid system that implements two different systems in the mitigation strategy. The first system is a many tile computer architecture developed on an FPGA, and the second is a spatial ionizing radiation detector.

#### Many Tile Computer Architecture

The fault tolerant computing solution developed here utilizes a many core computer architecture implemented on an FPGA. This computer architecture has the ability to receive an input from an external source in the form of spatial coordinates. The FPGA system is divided into tiles that are identical in size and structure. Each of these tiles contains a processor and can be partially reconfigured during operation. Partial reconfiguration (PR) is the act of reprogramming only a small section of the FPGA system. In this design, the size of a PR section would be an individual tile. Figure 1.2 demonstrates an FPGA architecture with 16 reconfigurable tiles. When a tile is partially reconfigured, contents of its configuration memory are restored and the circuitry within the tile is reset. In this way, faults in either the configuration memory or the tile circuitry can be repaired and the system can be restored to correct operation. Implementing partial reconfiguration provides a real time method to repair faults within the computer system. This FPGA design also implements another method to detect faults within the circuitry.

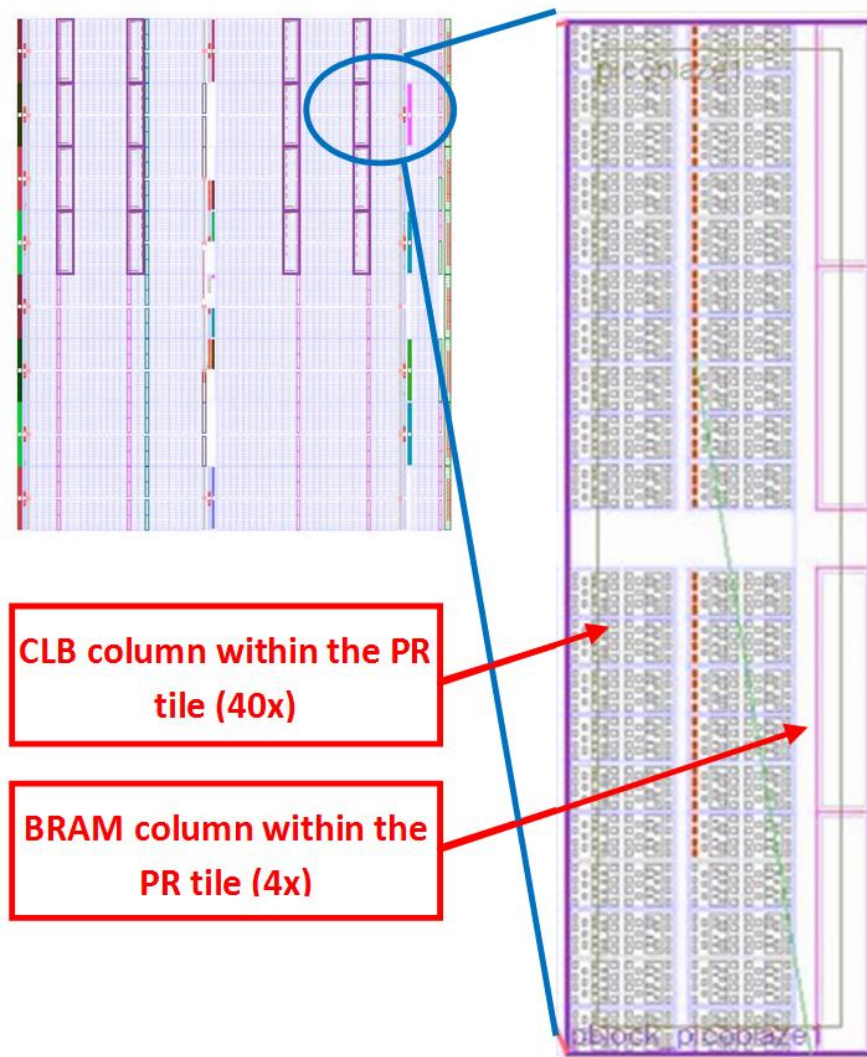


Figure 1.2 Illustration of an FPGA floor showing the 16 reconfigurable tile [5].

Another fault detection method utilized in the FPGA involves a voting system. During operation, three of the processors in the system are active at any one time. The rest of the processors in the FPGA are reserved as redundant spares. The three active processors are configured using triple modular redundancy (TMR). This approach takes the outputs of the three circuits and compares them all. If all three outputs are identical, no action is taken by the voting circuitry. If two outputs are the same and the third

differs, then the TMR determines that a fault has occurred in this third processor. Once the fault is detected, the two correct processors are allowed to continue operation while the faulted processor is deactivated and a spare is brought online and initialized. After the activation of the spare processor, the three active processors are allowed to continue operation while the faulted tile undergoes partial reconfiguration in the background. After PR is completed, the newly repaired tile is added back into the system as a spare that can be activated in the event of future faults.

In addition to the TMR process, the FPGA systems runs a background scan of all of the spare tiles configuration memory. The contents of this memory are compared to a golden copy that is located off chip in non-volatile memory. The circuitry that performs this scan is known as a scrubber. If the scrubber detects a fault in one of the spare tiles, PR is performed on that tile to return the tile to correct operation. This ensures that spare tiles are not activated with pre-existing faults.

Partial reconfiguration, triple modular redundancy, and the operation of the scrubber enable the FPGA computer system to detect faults and to recover from these events. These pieces provide the fault tolerance needed for this particular design and provide a platform for efficient and accurate aerospace computing.

#### Spatial Ionizing Radiation Sensor

In addition to the fault tolerance designed in the FPGA system, a sensor has been designed that can detect high energy radiation particles. This sensor is a silicon based device that detects high energy particles through the ionization produced when a particle penetrates the silicon lattice. The sensor has top and bottom electrodes that output this

generated charge. These top and bottom signals correspond to the X (top) and Y(bottom) coordinates respectively. The intersection of these channels allows the sensor to determine the location of the radiation particle strike. Since the radiation sensor is a semiconductor based device, the high energy radiation particle produces minimal permanent damage in the sensor. The generated charge is either collected or the electron-hole-pairs recombine. Either outcome returns the sensor to its original operating state and allows for the detection of more particles in the future. Combining the radiation sensor with the previously discussed FPGA computer architecture produces even greater fault detection in the system.

#### Integration of Radiation Sensor with Many Tile Computer Architecture

Positioning the radiation sensor directly over the FPGA can add even greater fault tolerance to the system. The radiation sensor outputs the exact coordinates of a radiation strike. These coordinates are then input into the FPGA computer system and the scrubber can jump to this location and fix the potentially faulted tile. In this way, the system takes a preemptive measure by correcting a location that is potentially faulted instead of waiting to observe the fault and then taking the necessary action. The radiation sensor will also act as a shield, to some extent, to the FPGA die. Lower energy particles will be completely blocked by the sensor. This eliminates some of the faults that could be caused by these lower energy particles.

### Improvements over Current Designs

The previously proposed solution offers many improvements over other fault mitigation strategies. Each of the individual components adds some improvements to the functionality of the system as a whole. The sensor allows for the coordinates of a radiation strike to be known almost instantaneously. This greatly improved functionality comes at very little additional cost since the sensor is made on a silicon wafer. The wafers themselves and the processing steps used to create the sensors are both inexpensive when compared to the cost required to implement other mitigation techniques. The FPGA computer system has many layers of fault detection and correction. The TMR circuitry and the scrubber ensure that both the active and spare tiles have no uncorrected faults. The greatest gain is achieved by combining these systems into one. This produces even more layers of fault protection and yields a system that can quickly detect faults, reconfigure the active tiles, repair the faulted tiles, and continue operating as if no fault had even occurred.

### Thesis Overview

The work presented in this thesis is focused on the radiation sensor and the integration of this device with the FPGA system. The radiation sensor and corresponding electronics as well as the interface between the sensor and the FPGA computer system are described in great detail. Chapter two provides some background information on current radiation sensor designs used in other research areas. Also, this section looks at past generations of the radiation sensor that is the focus here. Chapter three provides a

detailed description of the components in this design and includes a mathematical model of the radiation sensor. These different components include the radiation sensor, the radiation sensor electronics, and an FPGA based high speed event detector. Chapter four shows the prototyping of the various components and the printed circuit boards designed for these components. Chapter five shows the analysis of the results collected at the Texas A&M Cyclotron Institute. A mathematical correlation that relates the expected performance to the recorded data is also derived here. Finally, chapter six includes a project summary and recommendations for future work.

## CHAPTER TWO – SILICON BASED RADIATION SENSORS

### Current Designs Utilizing Radiation Sensors

The research described here has been focused on the design of a silicon sensor with the sole purpose of detecting high energy radiation particles that would be encountered in a space environment. In other areas of research, silicon sensors are used in different systems. Silicon based radiation sensors are common in many nuclear physics experiments. Some of these experiments involve using the radiation sensor as a spectrometer. In this application, various radiation sources are used to stimulate the sensor. The sensor is then used to produce an energy spectrum of the source by observing the outputs of the sensor. This enables better understanding of the emission properties of the radiation source [6].

Radiation sensors are also often used in particle accelerators and colliders. The silicon sensors are designed to detect various types of high energy particles. In accelerators, these sensors are positioned along the beam line to observe the flux (particles per second per area) and uniformity of the beam. This provides vital information to those using the beam for experiments. In colliders, a stack of silicon sensors is sometimes used. Each of these sensors is capable of providing the two dimensional location of the particle. By creating a stack, the three dimensional particle track can be observed. This can provide information such as how the high energy particle behaves in certain environments or how multiple particles interact with each other. One

place where this application is extensively used is at the Large Hadron Collider at CERN [7].

The use of radiation sensors in medical applications is a relatively new research area that has steadily grown in recent years. One novel usage of silicon sensors is in medical imaging instrumentation. Most medical imaging devices accomplish photon detection by using arrays of photomultipliers. The goal of this research effort is to replace these multipliers with silicon radiation sensors. The hypothesis is that this exchange will produce imagers with higher energy and position resolution as well as lower power consumption. A majority of the research is still in the early stages, but the potential outcomes could greatly improve current medical imagers and patient treatment [8]. These three areas are just a few of the many ways that silicon based radiation sensor are used in research. This number is sure to continue growing due the inexpensive nature of silicon and the extensive amount of knowledge about silicon fabrication techniques.

#### Previous Generations of Radiation Sensor Designs Completed at MSU

The current generation of the radiation sensor, is part of an ongoing research project that started a few years ago. Four previous radiation sensor generations have been studied extensively throughout this project. The results of this analysis lead to the current version of the design. Three of these previous generations were designed at Montana State University by former graduate students and were then fabricated using the Montana Micro-fabrication Facility (MMF). The other previous generation was a purchased commercial radiation sensor. This purchased sensor provided insight to the

operation of radiation sensors and aided in the fabrication of future generations of sensors. Each generation differs from the previous ones as more functionality is added. The current radiation sensor is the result of the efforts spent on the design and characterization of previous sensors.

### Generation 1: Single Sided Sensor

The first generation of the radiation sensor was designed by a former graduate student. Figure 2.1 shows a cross section of this sensor design.

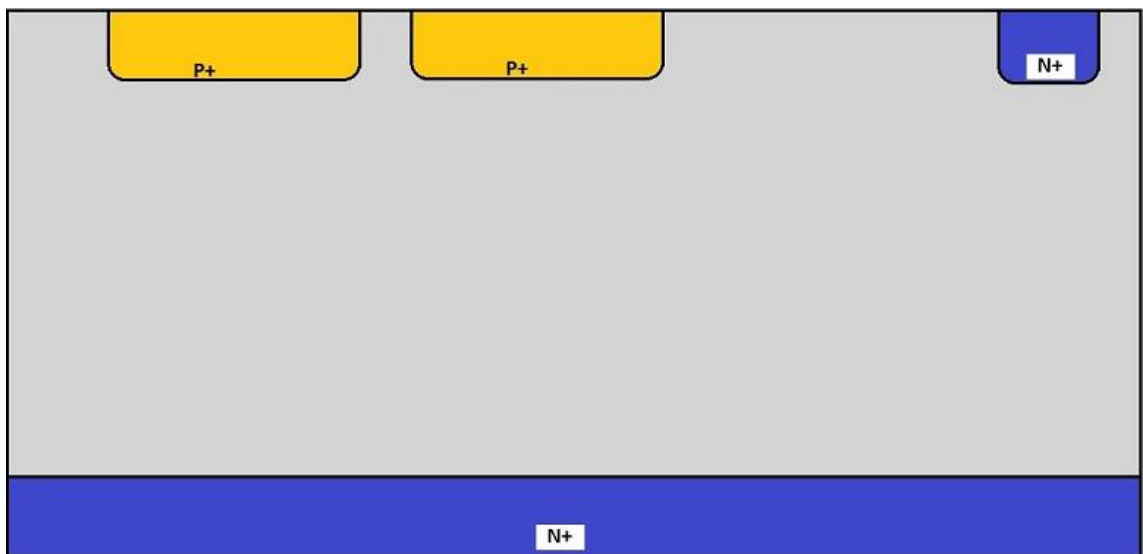


Figure 2.1 Cross section of the first generation radiation sensor [9].

This sensor was fabricated using the MMF at Montana State University. The radiation sensor was a single sided device meaning that the spatial sensing was only one dimensional for this sensor. An N-type wafer was used for the substrate for these wafers. The front side of the sensor was doped with parallel strips of P-type material (boron). These strips were the sensing elements for this design. In addition to the parallel strips, a

small region on the front of the wafer was doped with N-type material (phosphorous). This doped region produced a body contact for the device. The entire back side of the wafer was doped with N-type material. Surface contacts were then made on the front side strips and back side plane using aluminum [9].

Testing of the first generation sensor involved illuminating it with a red laser. The output from the sensor was fed through an op-amp circuit and then an LED. When the connected channel was illuminated, the LED lit up. This proved that the sensor was capable of producing a logic high when struck with a high energy source. Figure 2.2 shows a packaged version of this sensor being tested.

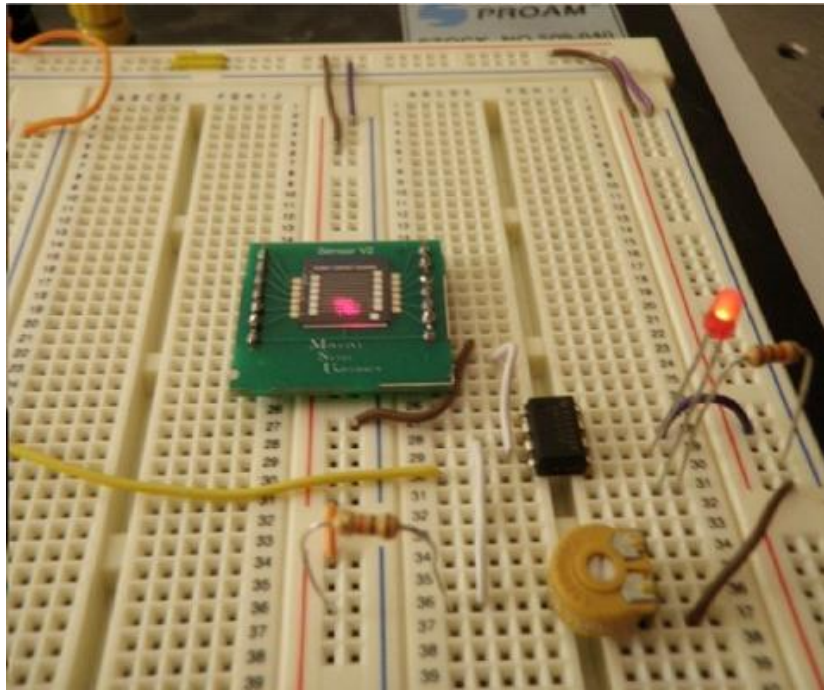


Figure 2.2 Packaged generation 1 sensor testing [9].

### Generation 2: Double Sided Sensor

The second generation of the radiation sensor was the first attempt at a double sided device. This would produce a sensor that was capable of sensing high energy particles in two dimensions. An N-type wafer was again used as the substrate for this sensor. For this design, the front and back side were doped with P-type material (boron) in parallel strips. The front side strips were rotated 90 degrees with respect to the back side strips meaning that the front and back side channels produced an orthogonal grid of channels. Small regions on both the front and back were doped with N-type material (phosphorous) in order to produce the desired body contacts. Figure 2.3 displays the cross section of this radiation sensor.

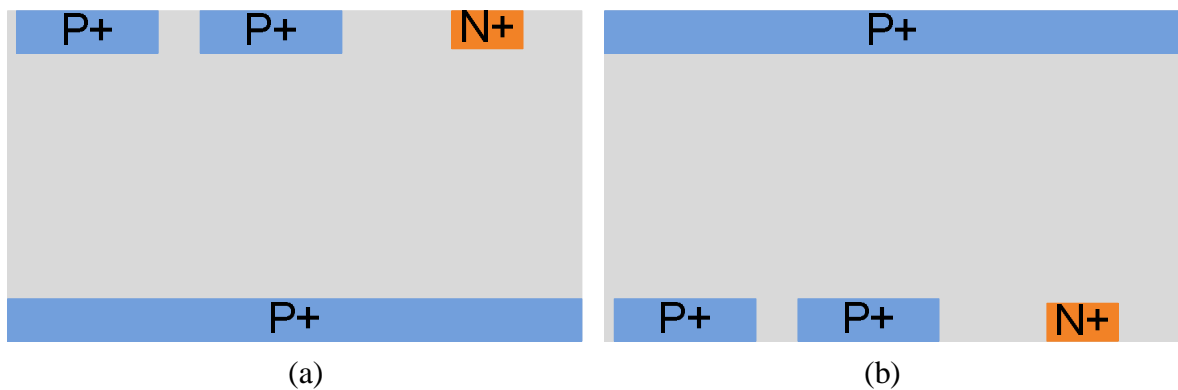


Figure 2.3 Cross section of the second generation radiation sensor when viewed (a) perpendicular to the top strips, (b) perpendicular to the bottom strips.

This generation was tested with an infrared (IR) laser because silicon is highly transparent to these wavelengths, which allowed both sides of the sensor to be stimulated. The testing of this sensor revealed that this design was actually a drift sensor and not a strip sensor as originally intended. This led to limited functionality of the sensor when the IR laser was used. In a drift sensor, the generated electrons are repelled by the

electrons in the P+ doped channels. This repulsion pushes the electrons towards the N+ areas, which was the body contact in this design. Ideally, the holes would then be collected by a P+ region on only one side of the sensor. Since these regions exist on both sides, accurate detection was impossible with this design. This made it clear that a drift sensor would not work for this design and a different design would be needed for future generations. The future generations were now designed based on a strip sensor design [9]. Figure 2.4 displays a packaged generation two sensor.

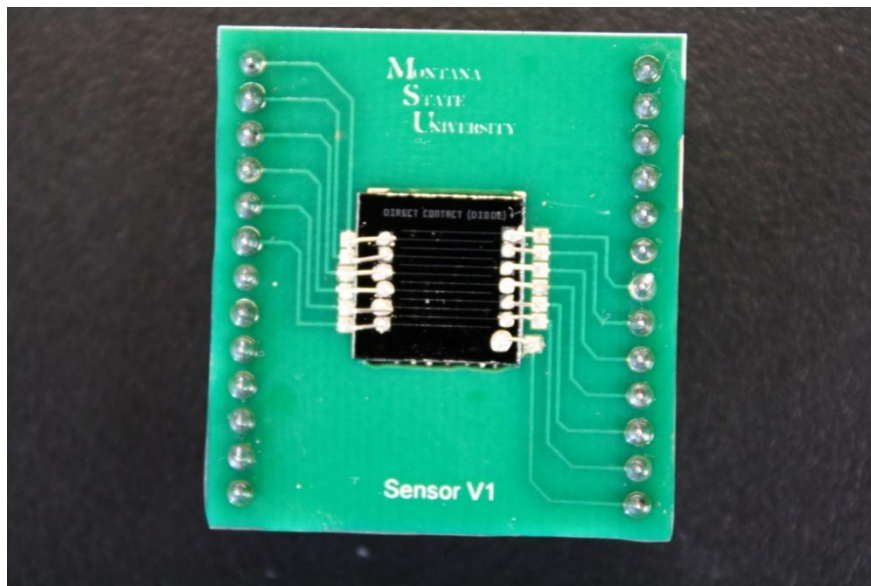


Figure 2.4 Packaged generation two radiation sensor [9].

### Generation 3: Commercial Sensor

The third generation sensor in this research project was a commercial device that was purchased from Micron Semiconductor. This sensor was fabricated with 16 top side channels and 16 bottom side channels. Testing of this device provided some insight into

how to design an effective strip sensor. The cross section of this commercial sensor can be seen in Figure 2.5.

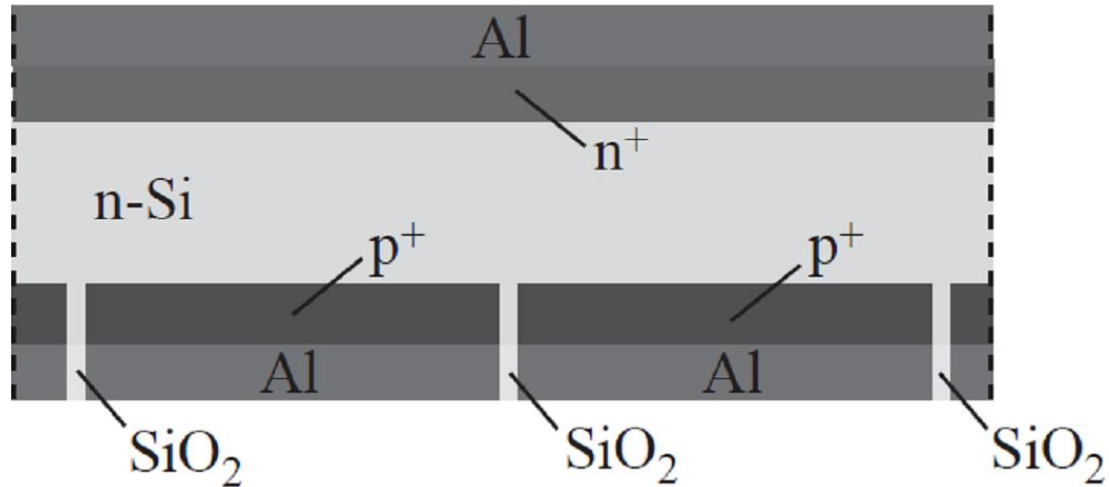


Figure 2.5 Cross section view of the commercial sensor purchased from Micron Semiconductor. Only one top side channel is seen because the P+ channels and N+ channels are perpendicular [10].

The performance of this sensor was also tested using an IR laser. A reverse bias voltage was applied to the sensor to aid in the collection of the generated charge. The circuitry used for this biasing can be found in Figure 2.6. With this stimulus, the outputs on the front and back side strips were observed. Figure 2.7 shows a normalized plot of all of the front and back side channel outputs. The shape of this plot clearly shows that the IR laser was aimed at the middle of the sensor during these measurements. The testing of this purchased sensor yielded useful information. This information was then leveraged in to the next generation design. Pictures of the packaged commercial sensor can be seen in Figure 2.8.

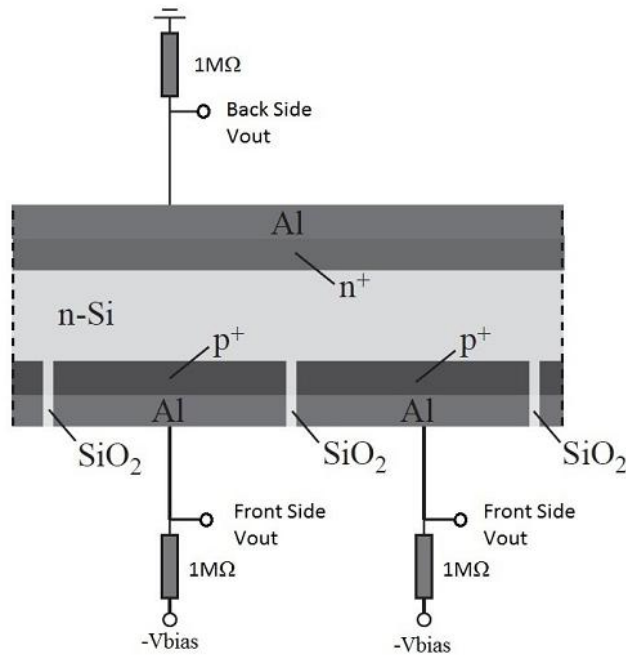


Figure 2.6 Cross section view of the testing setup that shows the applied reverse bias voltage [10].

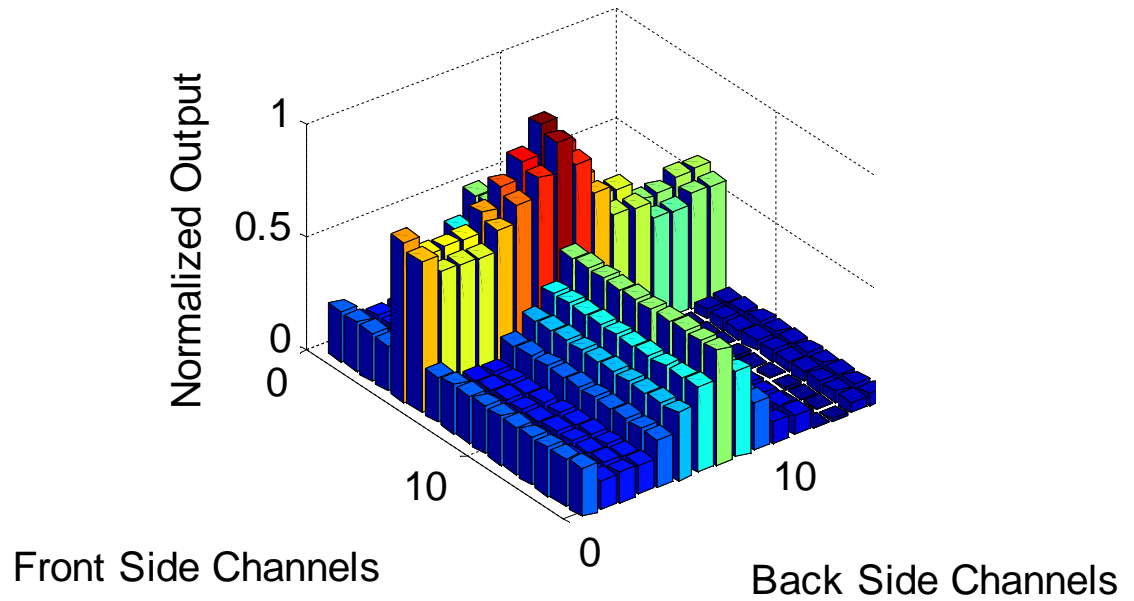


Figure 2.7 Outputs for all of the channels on the commercial sensor using an IR laser [9].

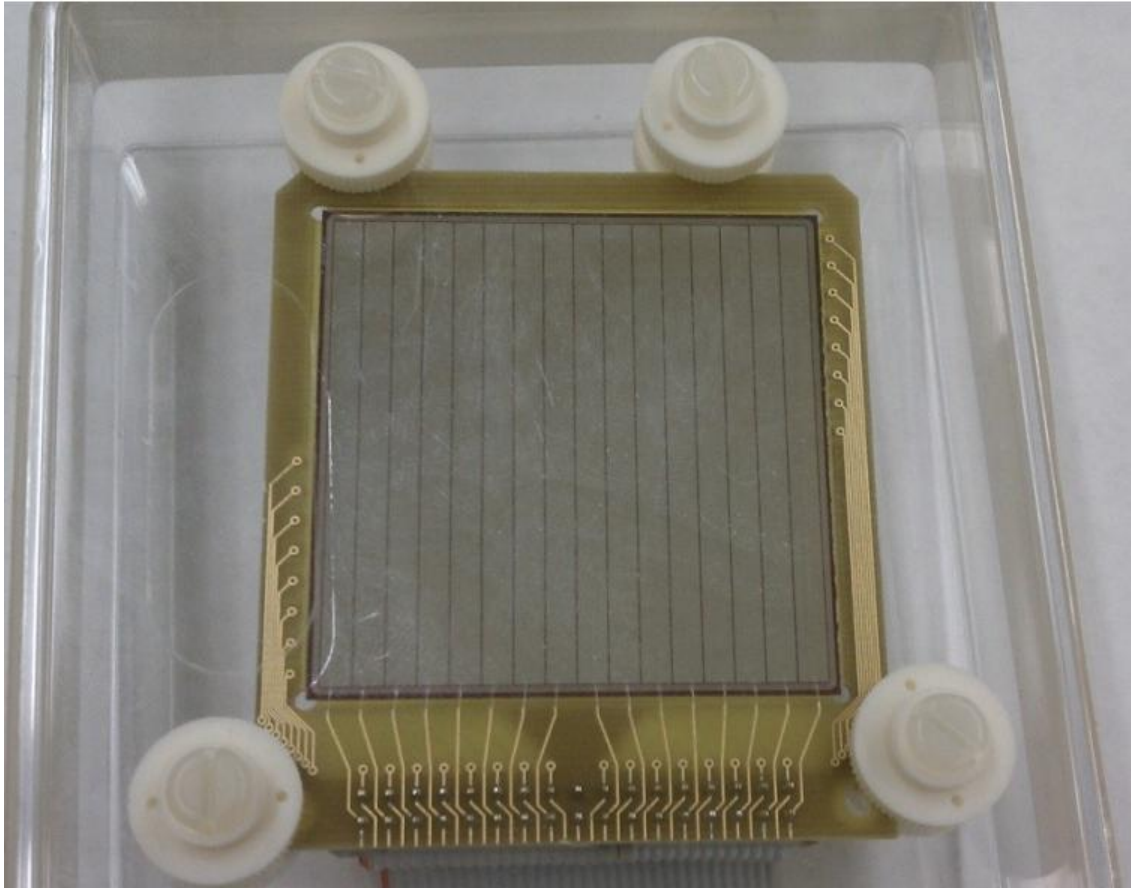


Figure 2.8 Picture of the radiation sensor purchased from Micron Semiconductor [9].

#### Generation 4: Double Sided Strip Sensor with Back Side Barrier Diffusions

The design of the generation 4 sensor is strongly leveraged off of the purchased sensor. This design is the first successful attempt at creating a double sided strip sensor. The fabrication process used to create this sensor is very similar to that used in the creation of the generation 5 sensor. For this reason, the fabrication sequence will not be described in detail until chapter three where the generation five sensor is described. Additional information on the fabrication sequence used for the generation 4 sensors can be found in a previous graduate student's thesis [9]. The only difference in fabrication

between generation 4 and 5 is that generation 4 only has barrier diffusions on the back side of the sensor. The generation 5 sensor has barrier diffusions on both the front and back side of the sensor. The purpose of these diffusions will be explained in greater detail later. A cross section of the generation 4 sensor is shown in Figure 2.9.

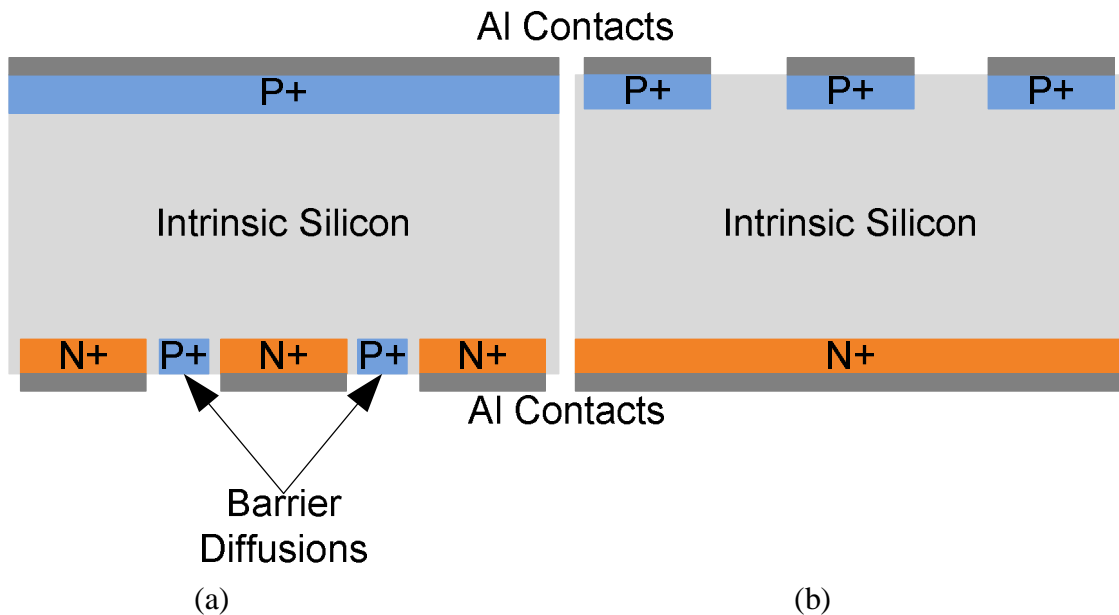


Figure 2.9 Cross section of the fourth generation radiation sensor when viewed (a) perpendicular to the bottom strips (b) perpendicular to the top strips.

As with the previous generations, this sensor is tested using an IR laser. The testing setup used is the same as that seen in Figure 2.6. Figure 2.10 shows the results of this testing. The plot shows that the new fabrication sequence correctly produced a strip sensor whose performance is very similar to that of the purchased sensor. This is a major accomplishment and led to further advances in the future generation of the radiation sensor. Combining the results obtained from these previous generations led to the current state of the radiation sensor.

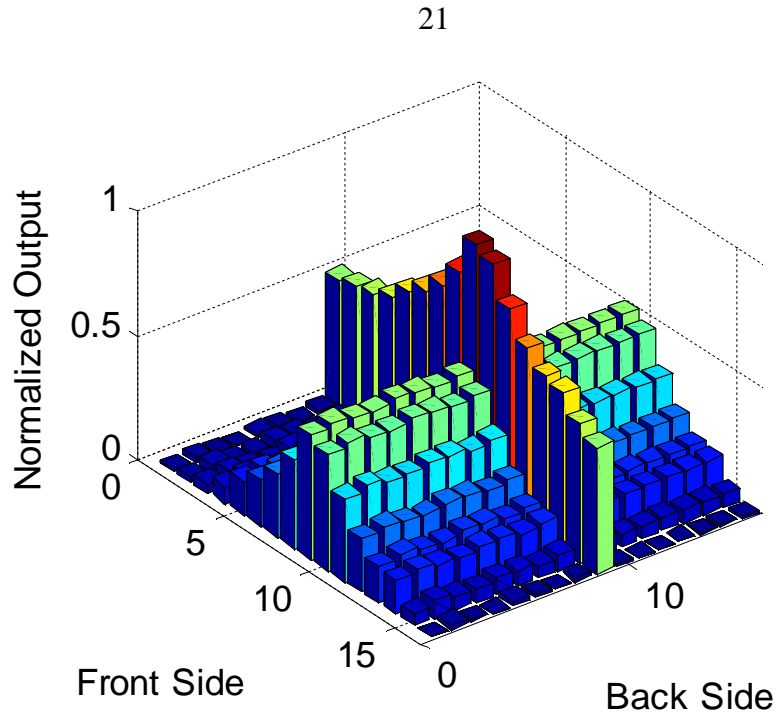


Figure 2.10 Plot showing the outputs of the generation 4 sensor when the IR laser was used as the stimulus [9].

## CHAPTER THREE – SPATIAL RADIATION

## SENSOR SYSTEM DESIGN

Generation 5: Double Sided Strip Sensor  
with Front and Back Barrier Diffusions

The goal of this research project is to design a sensor which can detect the position of ionizing radiation strikes with energy levels sufficient to cause single event effects in modern digital electronics. This sensor is designed for integration with a many tile computing system implemented on an FPGA to provide environmental information to the system in order to improve its fault tolerance. Signals are collected on each side of the sensor. The top of the sensor produces the X coordinates and the bottom produces the Y coordinates. These coordinates are then input into an FPGA based computer system created with redundant tiles arranged in a grid. Based on the strike location, the computer system takes the necessary actions to reconfigure the active tiles and avoid using tiles in the location of the radiation strike. This ensures that only undamaged tiles are used by the system and eliminates potential faults caused by the radiation strike. Additional circuitry then repairs the potentially faulted regions of the computer fabric. Following is a description of the generation 5 radiation sensor theory of operation, design, and a mathematical model.

Sensor Theory of Operation and Design

The design of this radiation sensor has been based on techniques and practices that were developed for use in nuclear spectroscopy experiments. In this field, it is

essential to be able to precisely measure the position of very fast ionizing particles. These particles are typically short lived and occur rarely, making it imperative to register every particle and not miss any due to imperfections in the detector [11-14]. Semiconductor radiation sensors have been developed to monitor the paths of these particles as they exit a reaction. Conversely, this design uses the same techniques to monitor the position of ionizing radiation as it enters electronics in aerospace computer systems. This sensor is designed to sense high energy radiation particles such as protons, alpha particles, and heavy ions. These particles produce the greatest ionization in the sensor and are capable of easily traversing the entire thickness of the sensor.

The fundamental sensing element in this radiation sensor is a PN junction.

Figure 3.1 shows a cross-section of this element.

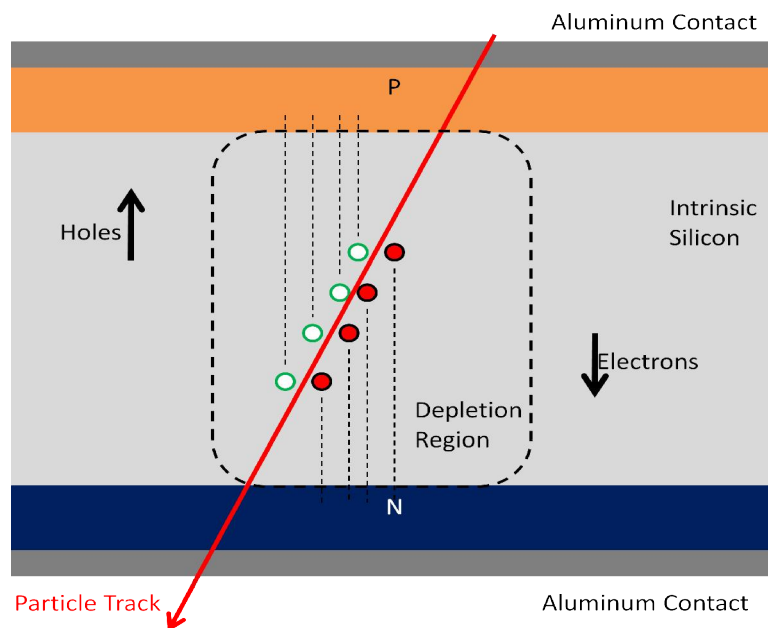


Figure 3.1 Cross section of a PN junction, which serves as the sensing element in the designed radiation sensor.

A PN junction is created in the silicon substrate by doping opposite sides of the wafer with P+ material (boron) and N+ material (phosphorous). The diffusion of these dopants produces free charge carriers in the substrate. The N-type dopant brings in an excess of electrons and the P-type dopant brings in an excess of holes to the silicon lattice. If these doped regions are sufficiently close, diffusion occurs in an attempt to reach equilibrium. The electrons diffuse to the P-side and the holes diffuse to the N-side of the silicon. This transfer leaves behind dopant ions which causes the N-side to have excess positive charges due to the phosphorous ions and the P-side to have excess negative charges due to the boron ions. The positive ions on the N-side and the negative ions on the P-side interact to produce an internal electric field. This field opposes the diffusion of free charge carriers and eventually equilibrium is reached by the junction. At equilibrium, the electric field produces a region void of charge which is known as the depletion region. Any charge inside of this region will be swept out due to the force of the electric field. The charges that are able to diffuse eventually come into contact with a charge of the opposite polarity. This leads to the recombination of these traveling charges, which eliminates any charge that diffused. Figure 3.2 shows a PN junction at equilibrium.

The ionizing radiation passes through the sensor creating electron-hole-pairs at an average rate of 3.3 eV of energy absorbed per electron-hole-pair generated. In a silicon based device, the energy transferred from a 1MeV particle would produce 48.4 fC of charge, which is more than enough to flip the state of a modern logic circuit [11-14]. Within a diffusion length of the depletion region, the intrinsic electric field sweeps the

charges toward their corresponding electrodes, electrons to the N+ side of the substrate and holes to the opposite P+ side.

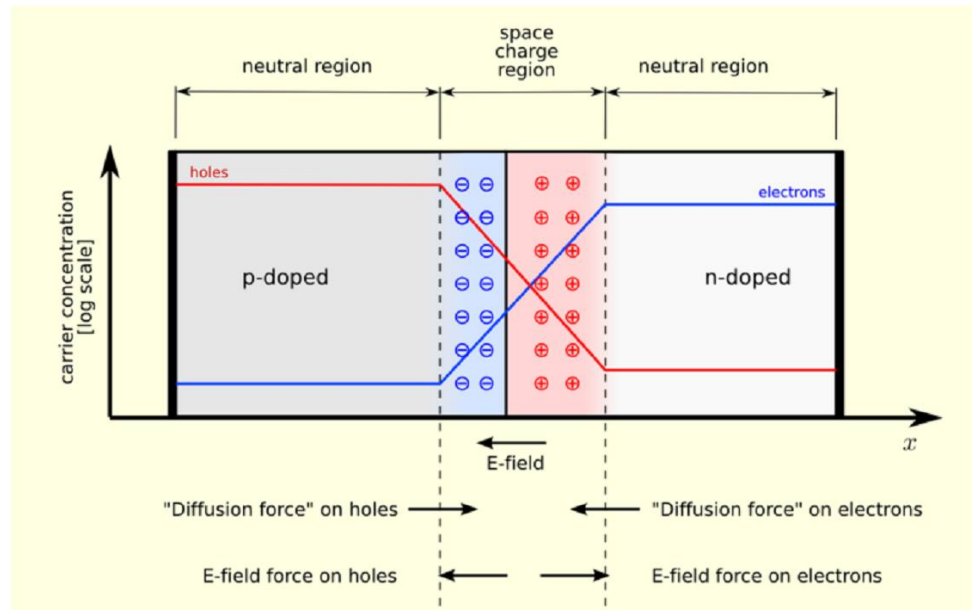


Figure 3.2 Diagram of a PN junction once equilibrium has been reached [9].

The energy of the radiation particle and the size of the depletion region inside of the sensor determine the amount of charge ultimately collected.

The design selected for the current generation of the radiation sensor builds on that of a double sided strip detector. The strip detector is used as the basis for this design because of its simplicity, speed, and ease of production. These strip detectors can also have high resolution due to the nature of the design [15-16]. The principle of the strip detector is very similar to the PN junction sensing described previously. The electrodes in the radiation sensor are broken up into narrow strips running orthogonally to each other on both sides of the substrate. Each of these electrodes is readout as a separate electrical output. When charge is created in the sensor, it diffuses to the front and back of

the device and is collected on the closest strip. The location of the ionizing radiation strike is determined by the intersection of the front and back strips outputs produced by the generated charge.

### Radiation Sensor Performance Modeling

The sensor substrate is intrinsic silicon. The sensor is composed of a front side doped with P+ material (boron) and a back side doped with N+ material (phosphorous). These dopants create the charge collection regions inside of the sensor. For this design, high doping concentration (on the order of  $10^{19} \text{ cm}^{-3}$ ) on the front and back surfaces of the wafers is desired. These high surface concentrations produce two results. The first result is that a high doping concentration on the surface allows for a better electrical connection between the doped regions and the aluminum electrodes. This ohmic connection greatly reduces the series resistance in the device and limits one potential area for loss. The second effect of a high surface doping concentration is that the depletion regions are pushed to a maximum depth into the bulk silicon wafer. By increasing the depth of the depletion regions, the active area of the sensor capable of collecting electrons and holes is expanded.

In order to determine the active sensing area for the sensor, the size of the depletion regions needs to be calculated. These active areas provide an idea as to how much charge is collected for a given radiation strike. The size of the depletion region directly depends on the doping concentrations achieved during fabrication. Measuring the sheet resistivity of the completed devices provides a means to calculate these doping

concentrations. Using (3.1), the resistivity of the doped sensor strips is determined from the measured sheet resistivities.

$$\rho_{P/N} = R \cdot X \quad (3.1)$$

In (3.1), R is the measured sheet resistivity and X is the final junction depth of the dopants after the completion of the fabrication process. Equation (3.2) is used to determine the final junction depth required in (3.1).

$$X = 2 \cdot \sqrt{-D_{tot} \cdot \ln(N_D \sqrt{\pi \cdot D_{tot}} / q)} \quad (3.2)$$

In (3.2),  $D_{tot}$  is the total dose (diffusion coefficient multiplied by diffusion time),  $N_D$  is the background concentration in the substrate, and  $q$  is the charge of an electron. Once the junction depth is known, the doped region's resistivity is determined. With these resistivities calculated, a table is used to find the actual doping concentration achieved during fabrication that would produce these resistivities. Once these concentrations are known, the built in voltage is calculated by (3.3).

$$V_{bi} = \frac{kT}{q} \ln\left(\frac{N_J N_D}{n_i}\right) \quad (3.3)$$

In (3.3) the variable  $k$  is Boltzmann's constant,  $T$  is the temperature in Kelvin,  $q$  is the charge of an electron,  $N_D$  is the background donor concentration of the wafer (provided by the manufacturer), and  $n_i$  is the intrinsic concentration in the wafer and is equal to  $n_i = 1.45 \cdot 10^{10} \text{ cm}^{-3}$ . The value used for  $N_J$  is either the P+ or N+ doping concentration that was determined using the previous results. The built in voltages calculated here, aide in the creation of the depletion regions inside of the silicon wafer.

These widths determine the active region of the sensor. To find the depletion width, (3.4) is used when no external bias voltage is applied to the radiation sensor.

$$W_{no\_BIAS} = \sqrt{\frac{2\epsilon_r \epsilon_o (N_J + N_D)}{qN_J N_D}} (V_{bi}) \quad (3.4)$$

The variables in (3.4) have the following values:  $\epsilon_r$  is the relative permittivity of the silicon sensor ( $\epsilon_r = 11.7$ ),  $\epsilon_o$  is the permittivity of free space ( $\epsilon_o = 8.85 * 10^{-12}$  F/m), and  $V_{bi}$  is the built in voltage that was just calculated.

Typical doping concentrations produce depletion regions that cover some percentage of the total sensor thickness. These partial depletion regions result in a collection area for the sensor that is less than the total thickness. If the charge is produced within a diffusion length of the depletion region, there is a high probability of it being collected. The remaining charge produced by the ionizing radiation strike is most likely not collected and is lost to recombination and diffusion (across the sensor instead of towards an output electrode). These losses can be compensated for by applying a reverse bias voltage to the PN junction, which causes the depletion regions to be expanded. This voltage is applied as a negative voltage to the top (P+) side of the sensor through the designed biasing circuitry that will be shown later. Using (3.5) shows how the depletion widths are changed when a bias is applied to the junction.

$$W_{BIAS} = \sqrt{\frac{2\epsilon_r \epsilon_o (N_J + N_D)}{qN_J N_D}} (V_{bi} - V_{BIAS}) \quad (3.5)$$

Applying a large reverse bias voltage causes the depletion regions to grow. By selecting the correct bias, the depletions regions are expanded and stretched across the entire

thickness of the wafer. This gives the maximum collection region of electron-hole-pairs and the best overall performance for the radiation sensor.

With this increased depletion region size, applied bias voltage, and built in voltage known, the internal electric field produced inside of the sensor is calculated using (3.6).

$$\vec{E} = -\nabla V \approx \frac{V_{bi} + V_{BIAS}}{W_{BIAS}} \quad (3.6)$$

This electric field is produced by the built in voltage acting across the thickness of the depletion region inside of the sensor. If an electron-hole-pair is produced inside of the depletion region, these charges are immediately separated by the electric field. This separation results from the force exhibited by the electric field on the charged particles. The velocity of these charge carriers due to the electric field can be determined by (3.7), where  $\mu$  is the mobility of the electrons or holes.

$$\vec{v}(x) = \mu \cdot \vec{E} \quad (3.7)$$

Once separated, these charges are collected at the electrodes on the front and back of the sensor. The time before the electrons and holes are collected depends on the location of their respective generation. This collection time is known as the transient time of the charge carriers. Using a known path length (distance from generation to collection), the carrier velocity, and (3.8) the charge carrier transient time is computed.

$$Transient\_Time = \frac{Collection\_Path\_Length}{\vec{v}(x)} \quad (3.8)$$

After determining the charge transient time, the current can be found if the amount of charge produced inside of the depletion regions is known. In order to determine the charge generated, the energy of the incoming particle must be known. For this analysis, we will assume that the incident particle is a heavy ion. For most available radiation sources, the linear energy transfer (LET) of the radiated particles is known. This value is used to quantify the effects of the ionizing radiation on materials. The LET for a given particle can vary greatly depending on the particles speed and charge. The final LET also depends on the target material since this value is closely related to the stopping power of the material. The LET for a particle is the energy transferred to the material per unit length where as the stopping power is the energy lost by the particle per unit length due to collisions with the target material. For heavy ions, the LET and stopping powers are nearly equivalent [17-18]. The Bethe-Bloch formula is used to quantify the stopping power of a material and can be used to roughly describe the LET of a heavy ion. This formula is seen in (3.9).

$$\frac{-dE}{dx} = \frac{1}{(4\pi\epsilon_0)^2} \frac{4\pi e^4 z^2}{m_e v^2} NZ \left[ \ln\left(\frac{2m_e v^2}{I}\right) - \ln(1 - \beta^2) - \beta^2 \right] \quad (3.9)$$

In (3.9),  $m_e$  is the mass of an electron,  $e$  is the charge of an electron,  $v$  is the velocity of the particle,  $z$  is the particle charge,  $N$  is the number of atoms per unit volume,  $Z$  is the number of electrons per atom,  $I$  is the average ionization potential of the medium, and  $\beta$  is equal to the velocity of the particle divided by the speed of light [18]. This equation can be used to estimate the LET for a variety of particles when this value is not readily available.

For this design, the LET is a measurement of the energy transferred to the silicon lattice from the high energy heavy ion. For a known LET, the charge per unit length (C/cm) produced inside the sensor is determined with (3.10).

$$Q(x) = \frac{LET \cdot \rho \cdot q}{3.3} \quad (3.10)$$

In (3.10), LET is the linear energy transform for a given particle in the desired target material in eV·cm<sup>2</sup>/mg,  $\rho$  is the density of the target material in mg/cm<sup>3</sup>,  $q$  is the charge on an electron, the factor 3.3 is the electron-hole-pair (EHPs) generation rate inside of the silicon lattice in EHPs/eV, and the variable  $x$  is used to represent a unit distance into the target. In general, a LET profile is available for a given heavy ion and the desired target material. This means that (3.10) allows for the calculation of the charge profile inside of the entire radiation sensor. The charge profile is a plot of the charge produced at each location throughout the sensor. Once the charge generated at certain locations and the transient time from these locations until collection is known, the current out of the radiation sensor is determined by (3.11).

$$I = \frac{Q}{\text{Transient\_Time}} \quad (3.11)$$

This equation yields the output current signals that can be expected for a given charge profile produced inside of the sensor.

The design of the radiation sensor is completed with these parameters in mind in order to maximize the electron-hole-pair generation and collection for the sensor when struck by a high energy particle. The fabrication sequence used on the sensors is an attempt at maximizing the outputs produced due to a radiation strike.

### Electronics Board

The previous section explains the design and theoretical performance of the radiation sensor. When a high energy particle strikes the sensor, an output current pulse will be produced on the electrodes of the sensor corresponding to the strike location. The front side electrodes will have an output current due to the holes and the back side electrodes will have an output current due to the electrons. This means that the front of the sensor will have a positive current, and the back of the sensor will have a negative current pulse. These output pulses will have a short pulse width (on the order of  $\mu\text{s}$ ) and small amplitude (on the order of  $\mu\text{A}$ ). The goal of the electronics board is to shape these output pulses into some form that is usable by the FPGA circuitry.

#### Amplifier Board Circuitry Design

In order to convert the fast, low amplitude analog output of the sensor into a digital signal usable by the FPGA, the designed circuitry needs to accomplish three tasks. First, the pulse width needed to be stretched so that very quick pulses are not output by the sensor and then remain unnoticed by the rest of the system. The second requirement for the electronics is to amplify the input current pulse to a level that can be detected by the FPGA. Finally, the third requirement for the electronics is to output a digital signal to the FPGA. This means that strikes would produce a logical high output (digital 1) and no strikes would produce a logical low output (digital 0). These steps combined would convert a sensor output to a usable FPGA signal.

The three required pulse shaping effects are implemented in a three stage circuit. Each stage consists of an op-amp circuit designed to accomplish the desired tasks. The first stage of the amplifier chain consists of a trans-impedance amplifier with a capacitor added in order to add a pulse stretching effect to this circuit [19]. This circuit converts the input current to an output voltage with a gain factor that is set by the trans-impedance resistor. This conversion is governed by Ohm's Law, with the output voltage being a scaled version of the input current. The pulse stretching is achieved by the charging and discharging of the capacitor connected between the input and output of the op-amp. The combination of this capacitor and the resistor connected in parallel produce a time constant that produces the desired pulse shaping. The time constant and gain for this first stage are shown in (3.12) and (3.13).

$$G = R_i \tag{3.12}$$

$$\tau_i = R_i C_i \tag{3.13}$$

Additional functionality added by this capacitor is that both a positive and negative pulse is output from this first stage op-amp circuit. This results from the charging and discharging of the capacitor. As the capacitor charges, an output of one polarity is seen and as the capacitor discharges, the opposite polarity output is seen. Both of these outputs experience the same pulse shaping and amplification. The reason that this is beneficial is because of the opposite polarity of the front and back side current inputs. This first stage produces outputs that are usable by the rest of the electronics chain regardless of the polarity of the input current which is essential for correct processing of both front and back side strikes.

The second stage of the amplifier chain is an inverting amplifier circuit. This op-amp circuit is intended to add additional gain to the input signal. After this stage, the output should be gained to a level that is very near to or at the positive voltage rail of the op-amps. The magnitude of this gain is shown in (3.14).

$$|A_v| = \frac{R_2}{R_1} \quad (3.14)$$

Also contained in this stage is an AC coupling capacitor that serves as the connection to the first stage of the amplifier chain. The purpose of this capacitor is to eliminate the DC offset voltage inherent in the first stage amplifier IC. Without removing this offset, the large gain on this second stage would rail the amplifier output making the observation of radiation strikes impossible.

The third and final stage of the amplifier chain is a comparator circuit. Implementation of this circuit involves connecting an op-amp in an open loop configuration. The non-inverting input of the op-amp is connected to the previous stage. The inverting input of the op-amp is connected to a reference voltage. A comparison is then made between the two inputs. If the non-inverting input is larger, then the circuit outputs a voltage equal to the positive power supply of the IC. If the non-inverting input is smaller, then the circuit outputs a voltage equal to the negative power supply of the IC. By selecting an IC that is powered off of +3 V and 0 V, the output of this last stage is a digital signal that can be used directly by the FPGA. With these three stages combined and values carefully selected to optimize the circuit's performance, the output of the final stage is 3 V when a radiation strike occurs and 0 V when no strike occurs.

The last part of the electronics that needs to be considered is the mechanism for coupling to the radiation sensor. A potentially large bias voltage may be applied to the sensor in order to full deplete this device. For this reason, another AC coupling capacitor is added in between the radiation sensor and the first stage of the electronics. This capacitor eliminates any offset produced by biasing the sensor. Also, large resistors ( $M\Omega$ ) are added between the bias voltage and the connection to the sensor. This ensures that the sensor outputs will be injected into the electronics and not simply pass into the power supply and be consumed. The designed amplifier chain is capable of taking a small analog signal and converting it into a digital signal useable by an FPGA system. Figure 3.3 shows a schematic of this circuitry. In addition to the shown components, power filtering capacitors are connected to all of the power pins for the ICs. This reduces the noise seen on these supplies.

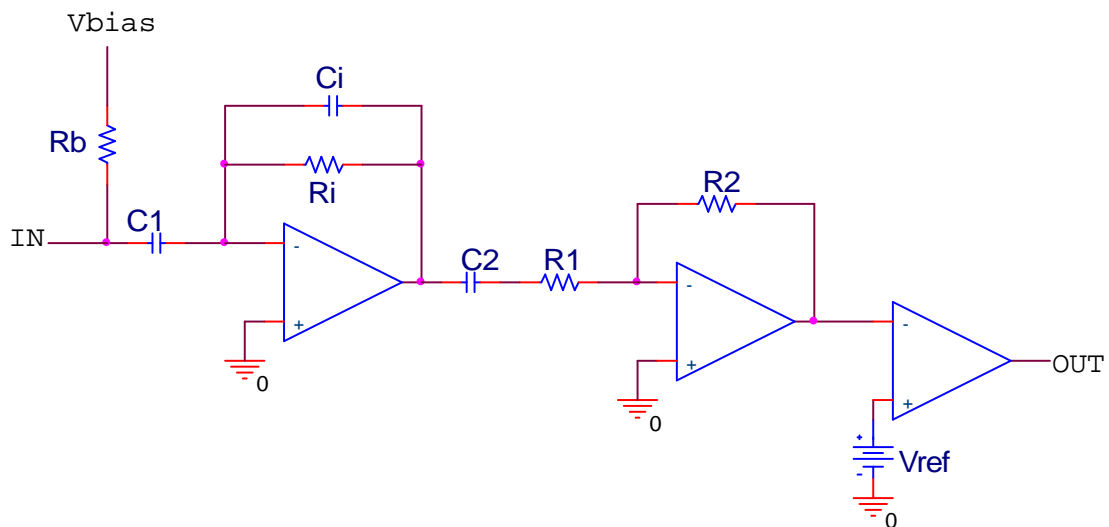


Figure 3.3 Schematic of the designed amplifier circuitry.

### High Speed Event Detector

The goal for the designed electronics is to take the input pulse and modify it into something easily useable by the FPGA. Despite the effort spent in this design, there is still the potential that a radiation strike will not be registered by the FPGA. This is because even with the pulse shaping and amplification, the pulses out of the last stage of the amplifier chain may still have a narrow pulse width. If this pulse width is narrow enough, the FPGA may not register it due the signal not being high during a rising edge of the FPGA clock. This would lead to unregistered radiation strikes and potential faults going uncorrected. The solution of this problem is to develop a high speed event detector. This circuitry would cause the FPGA to sample quickly and eliminate the potential of missed radiation strikes.

The high speed event detector design is based on the need to sample the incoming data at a fast enough rate that ensures no strikes go unregistered. This sampling mechanism is implemented using a chain of D flip-flops and a clock divider. For this design, a chain of 8 flip-flops is used. The devices are connected so that the output of the first flip-flop is connected to the input of the second and so on down the chain. These circuits run on the fast clock in the computer system. With this connection scheme, it takes an input into the first device 8 clock cycles to propagate through the entire system. This gives a greatly increased probability of registering even a very fast pulse.

In addition to being connected to the next flip-flop in the chain, the outputs of these devices are connected to an 8-bit register. For this register, the most significant bit is connected to the last flip-flop in the chain and the least significant bit is connected to

the first flip-flop. The outputs of the flip-flops are clocked into this 8-bit register at a clock rate that is 1/8 of the system clock rate (1/8 of the clock that the D flip-flop chain is running on). This implementation allows this register to hold 8 samples of the input channel at a time. These samples are taken at the fast system clock rate. This register holds these 8 samples until the next 8 samples of the input are clocked in at the slow clock rate. This entire system basically works as a serial to parallel conversion. Eight samples from a given sensor channel come into the event detector circuitry in a serial manner and are then clocked into a register, creating parallel data from the 8 samples.

The values in the 8-bit register are then passed to an 8 input OR gate. By doing this, the output of the gate is a '1' even if only one of the sampled inputs is a '1' or if all of the sampled inputs are a '1'. This gives the circuitry the ability to detect fast pulses but eliminates extra counts that are created by over sampling. With this approach, an input pulse would be counted only once if its pulse width was less than 8 times the period of the fast system clock. This value gives the minimum pulse width detectable for this particular event detector circuit. The output for a given input channel's OR gate shows the status of that channel. A '1' at this output shows that a radiation strike did occur during the last 8 samples, and a '0' shows that no strike occurred during the last 8 samples. A connection is made between this OR gate and a simple counter in order to log the total number of strikes observed.

The above system is replicated on all 32 sensor channels. This provides a way to count the strikes seen on all of the channels. Besides the individual channels, it is desired that the intersections between front (X) and back (Y) channels be monitored as well.

This is done by taking the output of a front side channel OR gate and a back side channel OR gate and connecting these two outputs to a two input AND gate. This is repeated for all combinations of the 16 front and 16 back side channels. The output of the AND gate is then connected to a counter in order to log the number of counts at that particular intersection. A count is only registered on the intersection counter if a strike is logged on a front and back side channel within 8 clock cycles of one another. The channel counters as well as the intersection counters all are operated by the divided by 8 clock. This produces the circuitry to detect a radiation strike at the intersection of a front and back side channel. Figure 3.4 shows a schematic of this event detector circuit. This schematic is shown for only a single X channel and a single Y channel even though this circuitry is replicated for every combination of X and Y channels. The channels selected are X1 and Y1 for this example. The D flip-flops are labeled with the letter 'D' and the locations in the 8 bit register are denoted with a letter 'S'.

Implementing this event detector and the previous electronics chain provides an effective line of communication between the radiation sensor and the FPGA based computer system. This is the entire purpose of this research. A radiation strike generates charge in the sensor. This charge exits the sensor as a current pulse. The electronics chain takes this current as the input and shapes this pulse into a digital signal. The digital signal is then sampled by the event detector and compared with other channels to check for an intersection. This produces the XY coordinates needed by the rest of the FPGA computer system in order to avoid the location of the radiation strike and repair the potentially faults circuit.

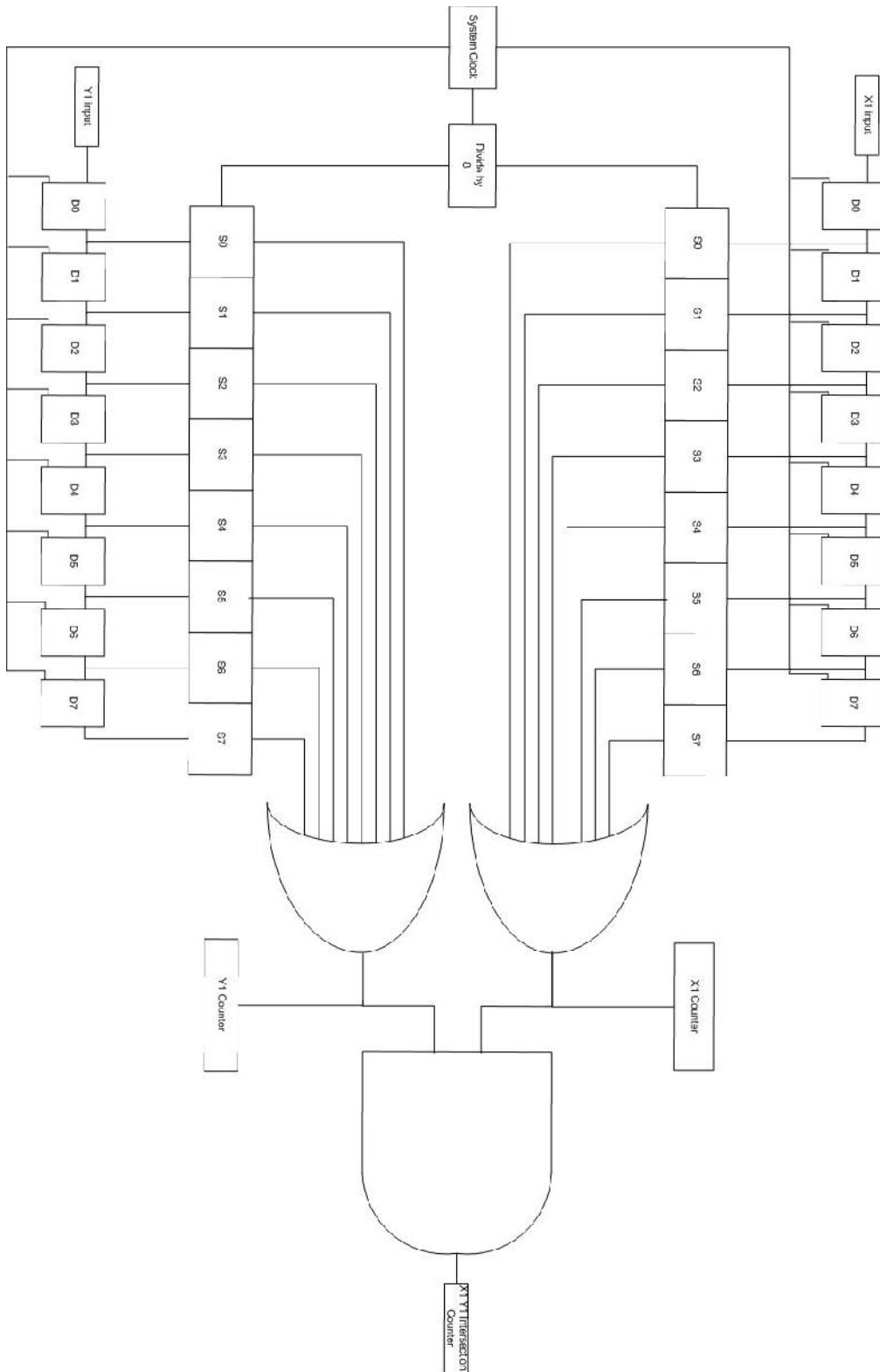


Figure 3.4 Schematic diagram showing the event detector circuit.

## CHAPTER FOUR – SPATIAL RADIATION

## SENSOR SYSTEM FABRICATION

Generation 5: Double Sided Strip Sensor  
with Front and Back Barrier Diffusions

The previously discussed design parameters are now implemented in the fabrication of the radiation sensor. The Montana Micro-fabrication Facility is used for the processing of the radiation sensor wafers. Upon completion, the whole wafers are taken to ADVR (a company in Bozeman) for dicing.

The dimensions of the die for the radiation sensors are 20 mm x 20 mm to accommodate all Xilinx FPGA chip sizes. These dimensions ensure that the sensor can completely cover the die used in the FPGA since these substrates are only a portion this area. This sensor design has 16 front side and 16 back side channels. The back side channels are rotated 90° with respect to the front side channels. The orthogonal grid of top and bottom channels produces 256 unique locations that can be stimulated by a radiation strike. The channel width on both the front and the back is 1 mm and the spacing between adjacent channels is 0.1 mm. The length of each channel is 18.7 mm. This produces an active sensing area for the sensor of about 350 mm<sup>2</sup>. Also included on the front side of the sensor are a set of bias rings. The purpose of these rings is to stabilize the long term performance of the sensors. Fully depleted sensors (large reverse bias voltage applied) can suffer from charge buildup on oxide surfaces. The buildup of this charge can affect the depletion region and eventually produce a reverse current which opposes the signal currents. Inclusion of the bias rings aims to limit this problem. The

bias rings act as a series of MOSFETs with the gates and sources connected. Daisy chaining these devices together gradually decreases the bias voltage towards the edges of the sensor which limits the potential for charge buildup and improves the long term performance of the radiation sensors [9].

### Sensor Fabrication Process

A 100 mm diameter, double side polished, 300  $\mu\text{m}$  thick, intrinsic silicon wafer with a <100> crystal plane orientation and a resistivity of 20,000 to 30,000  $\Omega\text{-cm}$  is selected as the substrate for the sensor (<www.el-cat.com> item number D046) [9]. With the design characterized and the materials selected, the fabrication process for the sensors begins. Following is a description of the fabrication process. A full, detailed description of the process is included in Appendix A. Figure 4.1 displays the cross sections of the sensor at various times during the fabrication process. This cross section view is taken perpendicularly to the bottom side strips.

The first step in the process involves growing a masking layer around the wafer. This oxidation process is a wet process, meaning that water vapor is used to aide in the growth of the oxide layer. This produces a  $\text{SiO}_2$  layer that is 0.5  $\mu\text{m}$  thick (Figure 4.1(a)). Next, photolithography is performed using a dark field mask. This mask is used to produce the front side P+ (boron) doping regions. The wafer is patterned and the regions for the front side strips are etched (Figure 4.1(b)).

The front side is now doped with boron (Figure 4.1(c)). The remaining oxide is removed using a BOE bath and a new layer of oxide is grown using the same method as previously described (Figure 4.1(d)). Photolithography is performed to produce the

regions for the back side N+ (phosphorous) doping. The wafer is patterned and etched to produce the back side strips (Figure 4.1(e)). The back side is doped with phosphorous (Figure 4.1(f)). Again, the remaining oxide is removed and a new layer is grown using the oxidation process (Figure 4.1(g)).

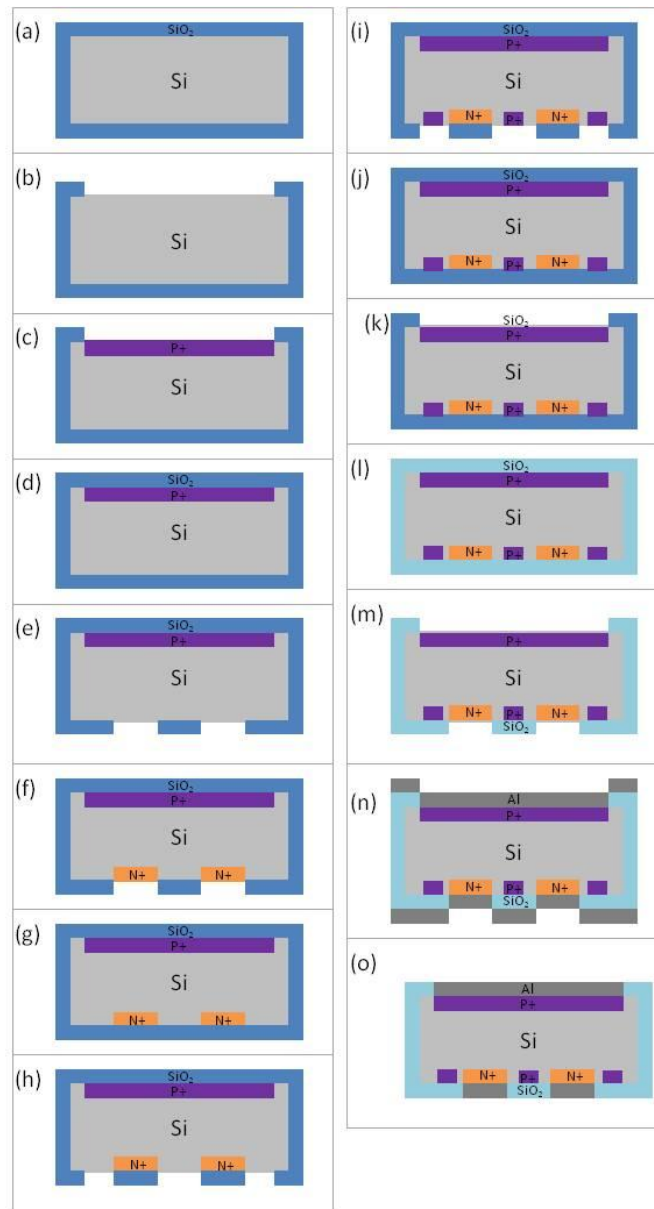


Figure 4.1 Fabrication process steps (a)-(o) used to create the sensors.

The next step is another photolithography process. This photolithography step is used to create the back side barrier diffusion areas. The back side of the wafer is patterned and etched as before (Figure 4.1(h)). The back side barrier regions are doped with P+ material (boron). These barrier diffusions are included to limit the charge coupling between adjacent strips on the back side of the sensor. These diffusions will eliminate the surface current that flows between adjacent strips by a diode in between the strips (Figure 4.1(i)). This leads to electrical isolation for the back side channels which is essential when trying to precisely determine the location of a radiation strike. The desire is that only a single front and single back side channel have an output for a strike and the barrier diffusions aide in this outcome. The remaining oxide is then removed using BOE.

Another oxide is grown on the surface of the wafer using a wet oxidation process (Figure 4.1(j)). The next step is a photolithography process that is used to create the front side barrier diffusions. The front side of the wafer is patterned and etched as in previous steps. The front side barrier regions are doped with phosphorous (N+ material) (Figure 4.1(k)). These barrier diffusions perform the same function for the front of the wafer that they do for the back. Inclusion of the barrier diffusions leads to better channel isolation and more accurate spatial radiation detection. The remaining oxide is then removed using BOE. These steps cannot be seen in Figure 4.1 due to the orientation of the cross section. An alternative view cross section is included later to display the location of these barrier diffusions.

The next step in the fabrication process involves growing a layer of dry oxide. In this oxidation, water vapor is not used to aide in the growth of the SiO<sub>2</sub> layer. Oxygen

gas serves as the catalyst for the growth of this oxide layer. The growth rate is much slower for a dry oxidation process, but the quality of the dry oxide is far superior to a wet oxidation process. This oxidation produces a layer of oxide that is 90 nm thick (Figure 4.1(l)). Photolithography is then performed on the front and the back of the wafer. This process is used to expose regions for the metal contacts to the front and back side channels. The front and back side contact areas are patterned and etched (Figure 4.1(m)).

Aluminum is then deposited on the front and back of the wafer using a physical vapor deposition (PVD) process. The aluminum sample that is evaporated for each side is  $36 \text{ cm}^2$  which results in a thickness of approximately  $0.4 \text{ }\mu\text{m}$  (Figure 4.1(n)).

Photolithography is then used to pattern the front and back side aluminum. This step leaves only the contact aluminum of the surfaces of the wafer. The wafer is patterned and etched for the last time in the process (Figure 4.1(o)). To complete the fabrication process, the wafers are annealed for 30 minutes at  $400 \text{ }^\circ\text{C}$ . This annealing improves the electrical connection between the deposited aluminum and the doped silicon regions. A low series resistance at these junctions is essential for this design. Nine different sensors are created on each wafer. The individual sensors are separated using a wafer saw.

Figure 4.2 shows the completed radiation sensors from two different cross section views.

Figure 4.3 displays a picture of the radiation sensors at the full wafer level before being separated.

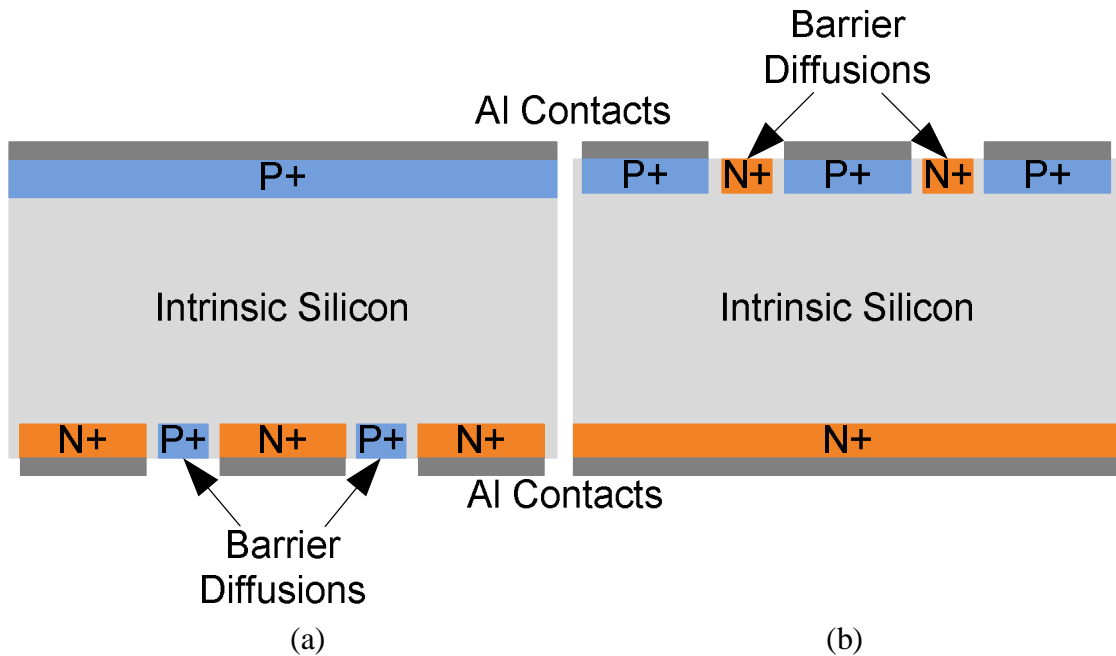


Figure 4.2 Cross section view of the radiation sensor when viewed from (a) perpendicular to the bottom electrodes (b) perpendicular to the top electrodes.

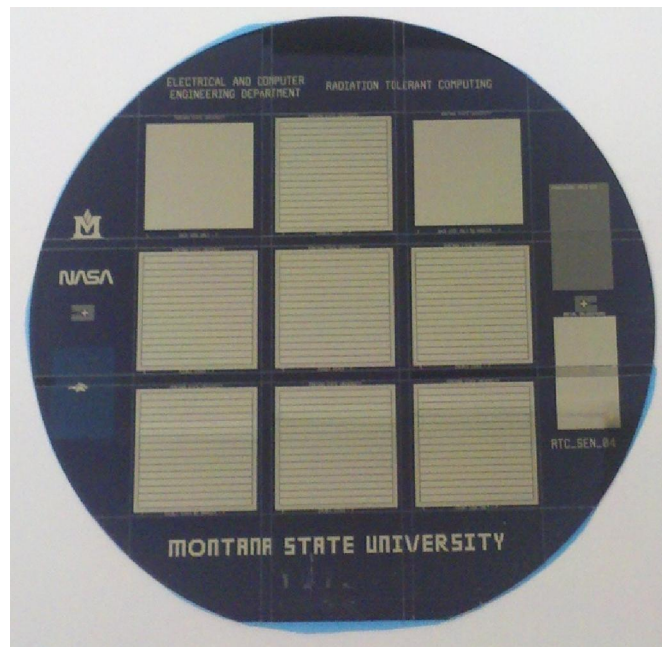


Figure 4.3 Picture of the radiation sensors at the full wafer level. This wafer has been diced, but the die have not been separated.

### Calculating Sensor Parameters

The sensors are fabricated using the previous process. The expected performance is then determined using a combination of measured and calculated sensor parameters. The wafers used for the sensor fabrication have a slight background concentration of donor atoms. The vendor specifies this background concentration to be  $N_D = 2.15 \times 10^{11}$  atoms/cm<sup>3</sup>. The maximum doping concentration achievable due to the solubility limit is  $N_{D+} = 1.2 \times 10^{20}$  atoms/cm<sup>3</sup> for the P+ doping and  $N_{A+} = 2.2 \times 10^{20}$  atoms/cm<sup>3</sup> for the N+ doping. The actual doping level achieved is less than these maximums and is calculated using the measured sheet resistivity of the devices. The sheet resistivity of one of the fabricated sensors is measured using a JANDEL four point probe. The measured sheet resistivities are  $R_{P+} = 46.07 \Omega/\square$  and  $R_{N+} = 11.46 \Omega/\square$ .

The fabrication process sets the final junction depth for the front and back side dopants since each thermal process causes the dopants to diffuse further into the silicon wafer. The doping times and temperatures are designed so that the final junction depth is less than 2  $\mu\text{m}$ . This meets the requirement of high surface doping concentrations. The junction depths calculated from the fabrication process are  $X_{P+} = 1.691 \times 10^{-4}$  cm and  $X_{N+} = 1.335 \times 10^{-4}$  cm. Using the measured sheet resistivities, the final junction depths, and (3.1) – (3.4), the radiation sensor parameters are calculated for this design. These values are shown in Table 4.1.

The depletion widths are the active charge collecting areas for the fabricated radiation sensor. Without applying an external reverse bias, approximately 125  $\mu\text{m}$  of the sensor thickness can be used to collect the charge produced by an ionizing radiation

strike. This limited active area is based on the fact that the diffusion length of the carriers is very short inside the sensor. Some charge will diffuse from outside of a depletion region and be collected, but the magnitude of this charge will be many times less than the charge generated and collected in the depletion regions. Figure 4.4 shows a cross section of the radiation sensor with these depletion regions clearly labeled. This view is taken perpendicular to the rear channel strips.

TABLE 4.1  
DEPLETION WIDTHS CALCULATIONS

Symbol	Quantity	Value
$R_{P+}$	P+ sheet resistivity	46.07 $\Omega/\square$
$R_{N+}$	N+ sheet resistivity	11.46 $\Omega/\square$
$X_{P+}$	P+ doping junction depth	$1.691 \cdot 10^{-4}$ cm
$X_{N+}$	N+ doping junction depth	$1.335 \cdot 10^{-4}$ cm
$\rho_{P+}$	P+ resistivity	$7.79 \cdot 10^{-3}$ $\Omega \cdot \text{cm}$
$\rho_{N+}$	N+ resistivity	$1.53 \cdot 10^{-3}$ $\Omega \cdot \text{cm}$
$N_{P+}$	P+ doping concentration	$1.15 \cdot 10^{19}$ $\text{cm}^{-3}$
$N_{N+}$	N+ doping concentration	$4.53 \cdot 10^{19}$ $\text{cm}^{-3}$
$V_{\text{bi-P+}}$	Front side built in voltage	0.619 V
$V_{\text{bi-N+}}$	Back side built in voltage	0.655 V
$w_{P+}$	Front side depletion width	61.57 $\mu\text{m}$
$w_{N+}$	Back side depletion width	63.31 $\mu\text{m}$

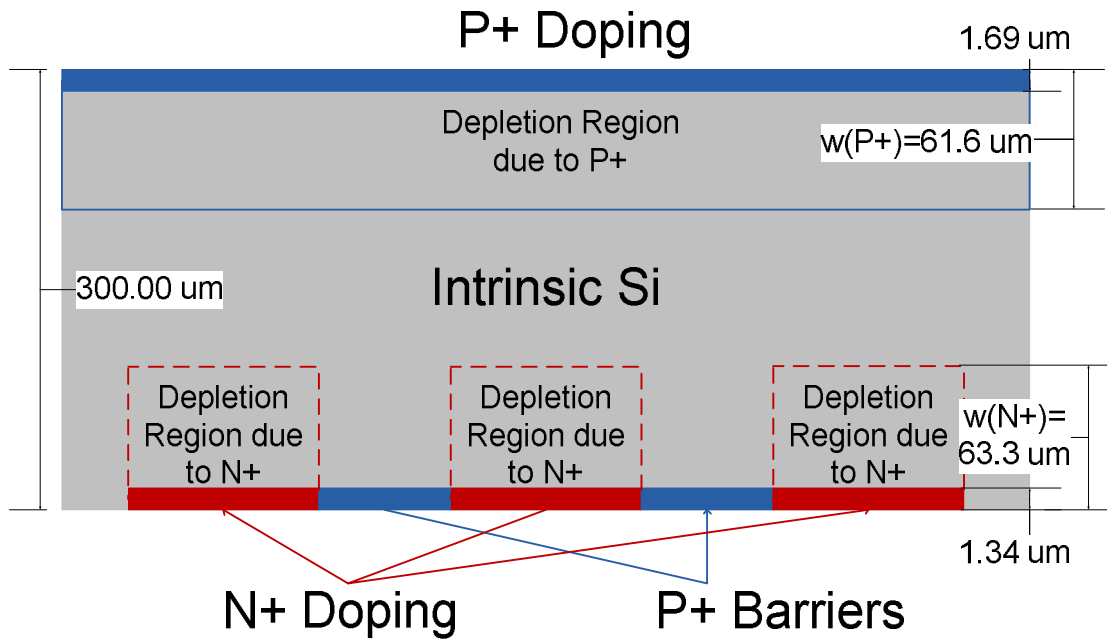


Figure 4.4 Cross section view of the radiation sensor with the depletion regions established.

### Simulated Heavy Ion Strike

The response of the radiation sensor is now characterized for a selected heavy ion. Texas A&M University has a research facility with the capabilities of producing a variety of high energy heavy ions. This facility contains a K500 superconducting cyclotron and an ECR ion source which allows for the production of a range of particles and energies [20]. For these high energy ions, many plots and data are provided to characterize the interaction of these ions with a silicon target. Figure 4.5 shows a plot of LET versus range into a silicon target. This plot is of particular importance to this project since an LET profile allows for the calculation of the charge generated inside of the sensor. In Appendix B there is a table that shows the various beams available and associated parameters.

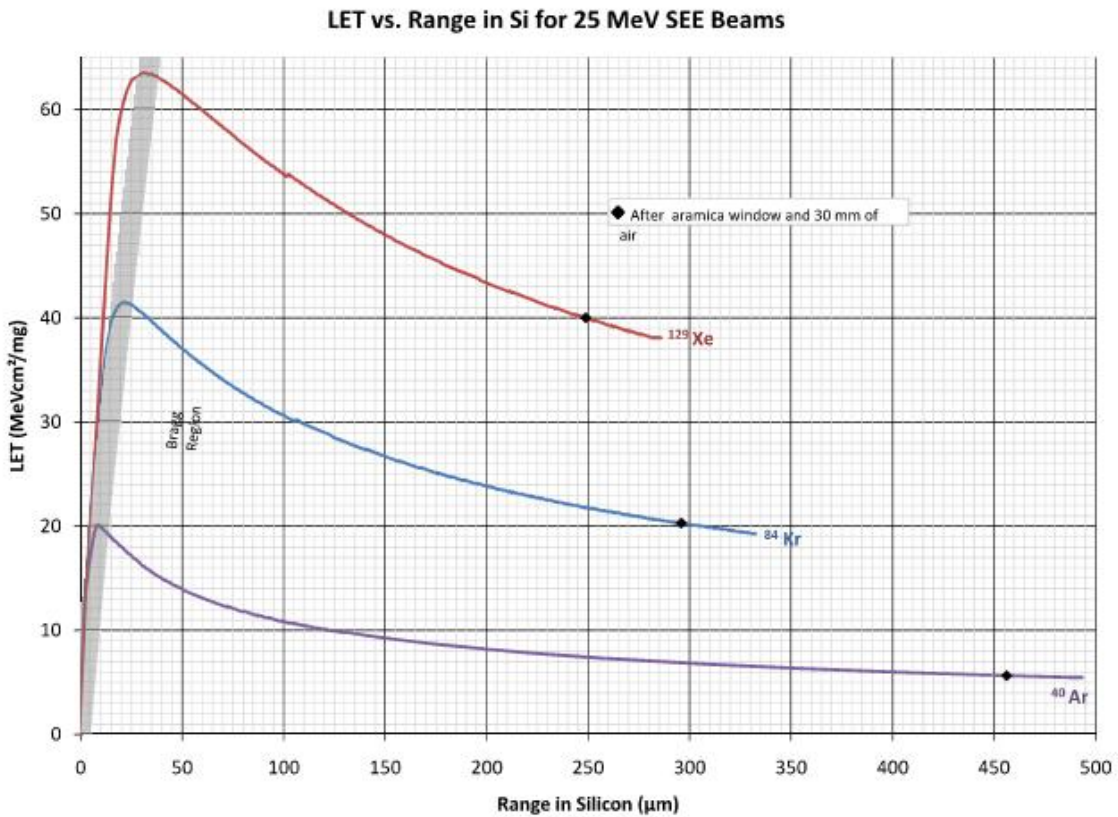


Figure 4.5 Plot of LET versus range in silicon for a few heavy ions available at the Texas A&M Cyclotron [20].

Due to its ability to penetrate the entire thickness of the sensor (300 µm), the krypton (KR) beam was selected from the above plot.

The parameters for the krypton heavy ion at 25 MeV/amu were used to calculate the output current of the sensor. This particle has a total ion energy of 2081 MeV (energy times mass in amu). This heavy ion has an energy that is a reasonable approximation of the radiation that this sensor could see in a low earth orbit. This same ion is also available at other cyclotron facilities for future chamber testing.

As a krypton ion enters the radiation sensor, the particle transfers energy to the sensor and creates electron-hole-pairs based on the LET for this ion. The LET profile

seen earlier is provided by the Texas A&M Radiation Effects Facility. In order to better understand this model, a free software program downloaded from the web is used. This program is called *SRIM: The Stopping and Range of Ions in Matter*. As the name indicates, this program allows for the calculation of the LET for a selected ion in a chosen target material. The ion and target are input, and the program outputs a text file with a variety of data, including the LET at certain incremental distances into the target material. This file allows for the precise reproduction of an LET profile such as the one seen in Figure 4.5 previously. Appendix C shows an example of the output of this program. This program is used to generate the LET in the silicon sensor for the 25 MeV krypton ion. With the LET profile known, the charge profile for the ion path through the sensor is now calculated. The charge profile is calculated for this ion as it penetrates the sensor using (3.10) and can be seen in Figure 4.6. The majority of the collected charge is produced in the front and back side depletion regions which are found using (3.4). These regions are shown in Figure 4.6 as the colored regions (red = front depletion region, blue = back depletion region).

Using (3.6) – (3.11), the currents produced inside of the sensor due to the krypton atom strike are calculated. Table 4.2 shows the additional sensor parameters calculated in order to determine these currents.

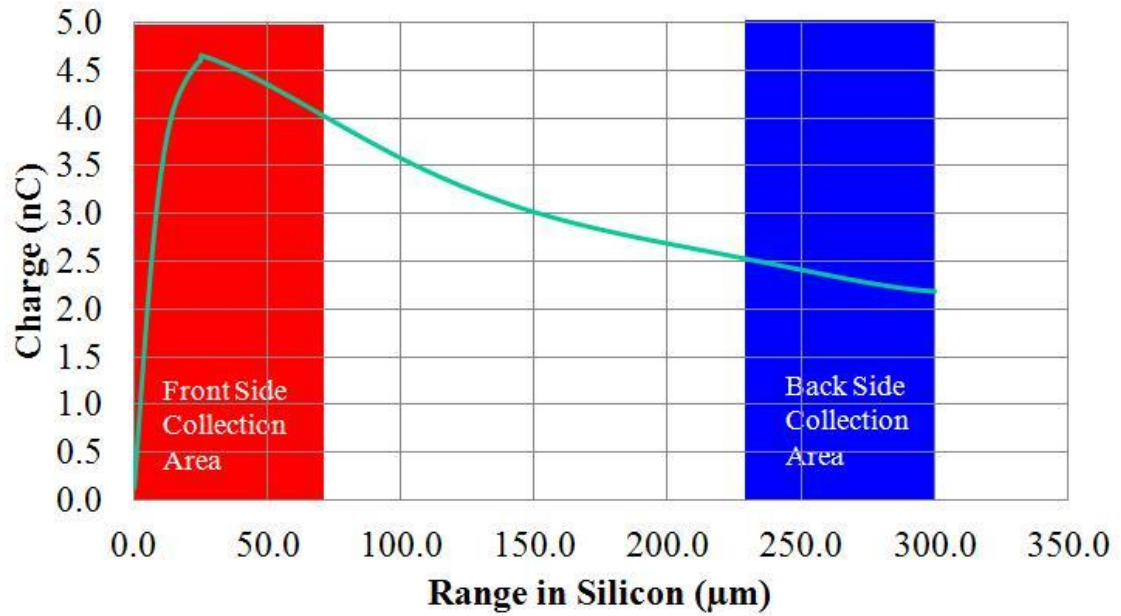


Figure 4.6 Charge profile produced in the sensor by a 25 MeV Kr atom.

TABLE 4.2  
SENSOR CURRENT CALCULATIONS

Symbol	Quantity	Value
$\mu_h$	Hole mobility	470.46 cm <sup>2</sup> /V-s
$\mu_e$	Electron mobility	1413.87 cm <sup>2</sup> /V-s
$E_{p+}$	Front side electric field	100.54 V/cm
$E_{N+}$	Back side electric field	103.46 V/cm
$v_h$	Hole velocity	47300 cm/s
$v_e$	Electron Velocity	146279 cm/s

The velocities in Table 4.2 are used in (3.8) to determine the transient times for both of these charge carriers as a function of position in the sensor. Finally, using the charge at a given sensor position, and the transient time for that location, the current is found for both the electrons and holes using (3.11). This analysis produces a data set of

currents for incremental steps through the entire thickness of the radiation sensor. In order to plot these currents, this data was imported into DxDesigner. To import this data, first a .csv file is made. This file is then formatted (commas removed, etc.) into one column of input data with time (s) and current ( $\mu\text{A}$ ). The file is then saved as a .pwl file since this is the format required by DxDesigner. A custom source is then produced in DxDesigner and the .pwl file is loaded into this source. Figures 4.7 and 4.8 show the hole and electron currents produced by this data file derived from the modeled response of the sensor to a high energy krypton atom strike.

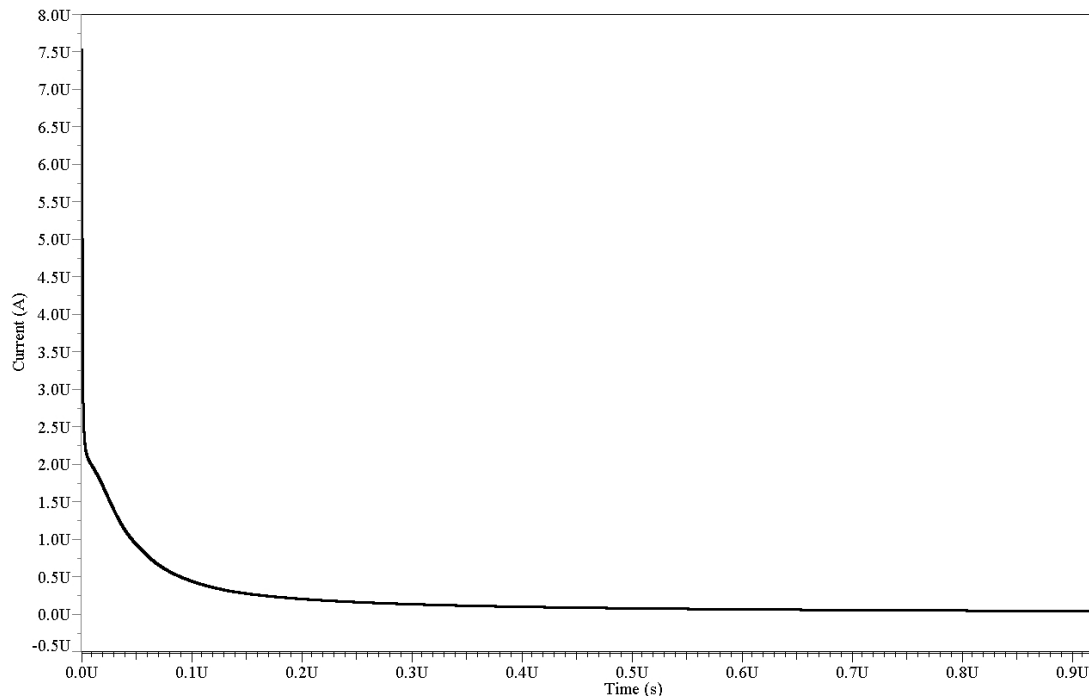


Figure 4.7 Hole current (front side) produced by the 25 MeV Kr ion strike.

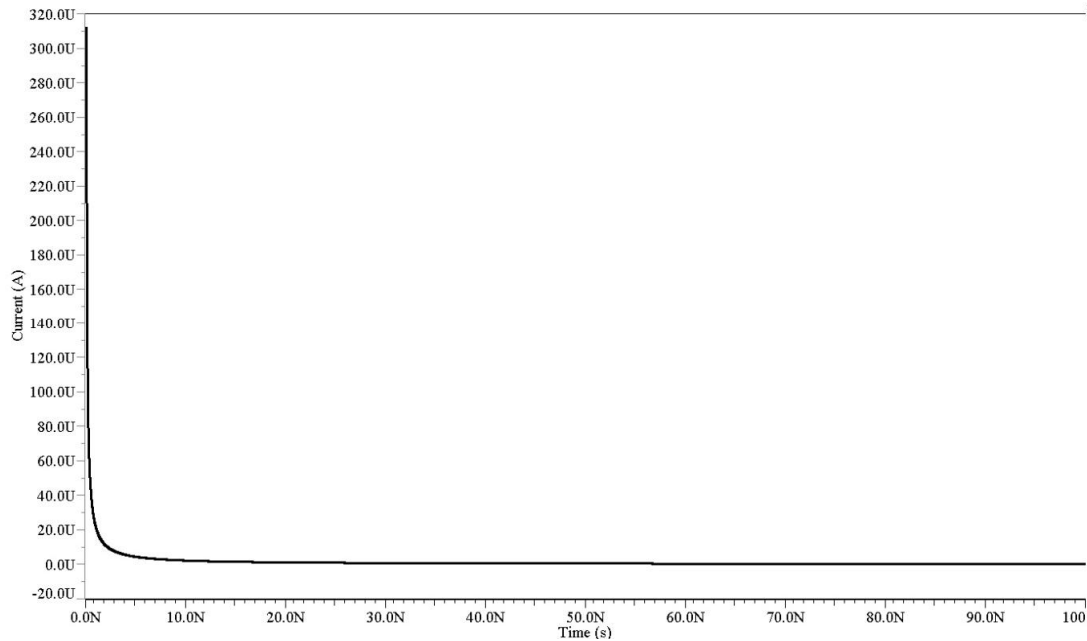


Figure 4.8 Electron current (back side) produced by the 25 MeV Kr ion strike.

### Radiation Sensor Package Board Fabrication

Now that the fabrication of the sensors is complete, it is necessary to develop a means to package the sensor so that the outputs can easily be connected to the designed electronics. The method decided upon is to create a printed circuit board (PCB) that holds the radiation sensor. The sensor outputs are routed onto the PCB using a small wire. This wire is soldered to the package board and connected to the sensor using a conductive silver epoxy. The signals on the PCB are then routed to an output connector. The printed circuit board is designed using two different tools. DxDesigner is used to produce the part symbols and the schematic that shows all of the connections. PADS Layout is then used to design the board outline, place the part footprints, and route the necessary traces. The combination of these two tools produces the final PCB design.

For this package board, a two layer board is used. Traces are routed on both the top and bottom sides of the board. The back side of the board also contains a copper pour that serves as a ground plane. The PCB is fabricated using Sunstone Circuits fabrication procedures. Figure 4.9 shows the completed PCB. Figure 4.10 shows the PCB with a radiation sensor mounted in it.

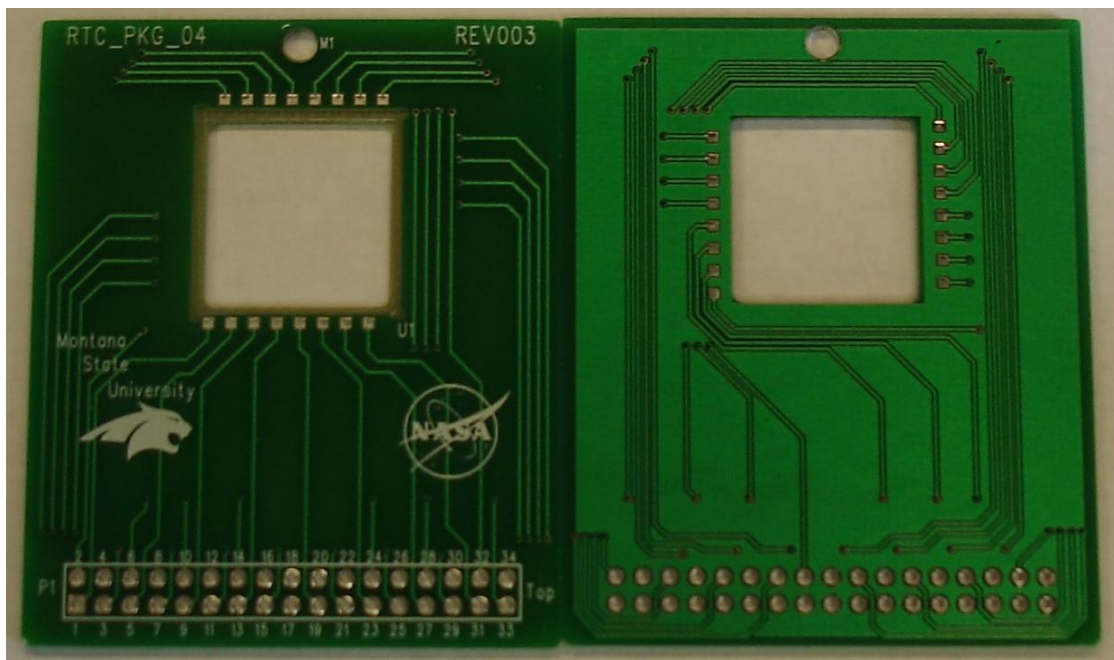


Figure 4.9 Picture of the radiation sensor package PCB.

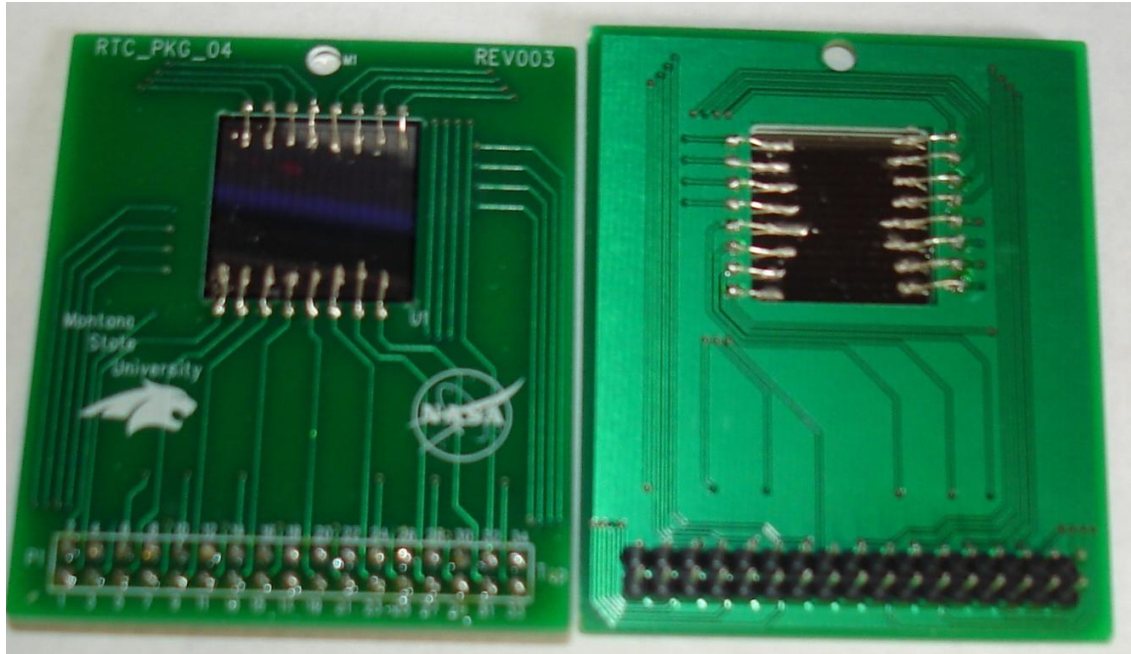


Figure 4.10 Picture of the radiation sensor mounted in to the fabricated PCB.

### Amplifier Board Implementation

The results of the simulated heavy ion strike are now used to select component values for the previously designed amplifier chain. The component values are chosen so that the input current is amplified to a usable signal by the end of the electronics.

### Component Selection

All of the resistors, capacitors, and op-amps need to be selected for this board. The ICs are selected based on a few different parameters. The same chip is used for both the first and second stage of the amplifier chain, so this first IC needs to be a quad package (four circuits per IC). This will help conserve space in the layout. The second parameter for this first stage is low noise. Since the gain of this circuit is large, the voltage and current noise of this first stage must be low in order to avoid saturation in the

later stages. The third condition is that the op-amp must be able to operate rail-to-rail. With these parameters in mind, a low noise amplifier is selected from ST Microelectronics with a part number of TS974.

The selection of the second IC involves a different set of parameters. This chip is used for the comparator circuit in the last stage of the amplifier chain. The first condition for this chip is that it must be powered off of a positive voltage and ground. This ensures that the output of this last stage is not a negative voltage. The second parameter is that this component must be a high speed device. This ensures that the output can change states very quickly. The component selected for this stage is from National Semiconductor and the part number is LMH6601.

The values for the capacitors and resistors are selected based on the previous simulations of the sensor output currents for a know radiation strike. As more testing is performed, these values will be optimized. Figure 4.11 shows a schematic with these values added. Once again, the capacitors connected to the power supplies for the ICs are not shown on this schematic. The first two stages are powered off of +3 V and -3 V, while the final stage operates off of +3 V and ground. For all of these voltages, a 1 $\mu$ F capacitor is used for the power distribution. For the bias and reference voltage, a 10  $\mu$ F capacitor is used.

The values shown in Figure 4.11 are for the front side channels and are therefore selected to amplify and shape the hole current. The only difference for the back side channels is that the resistor R2 is changed to 100 k $\Omega$  instead of the value shown in Figure 4.11.

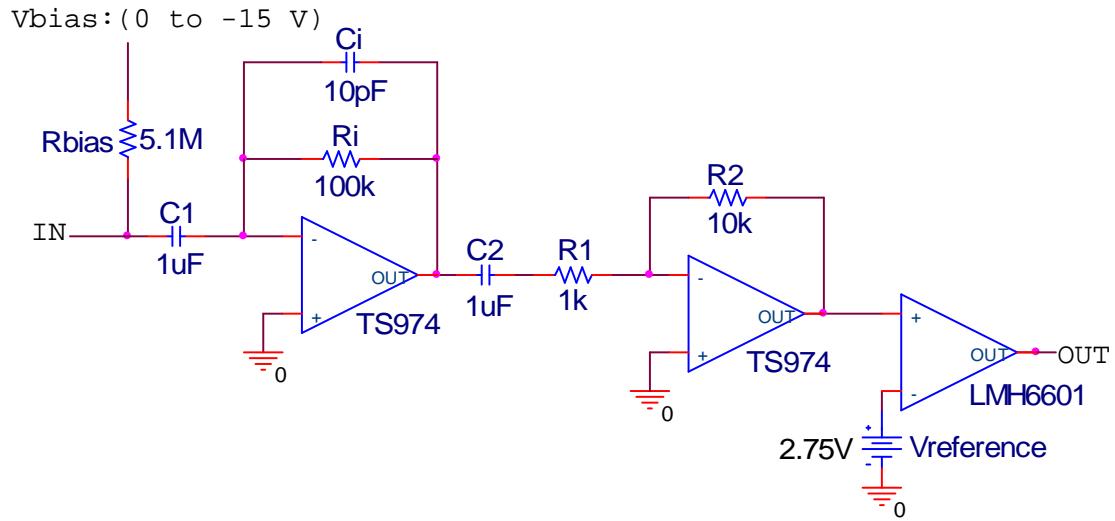


Figure 4.11 Schematic of the amplifier chain with the component values included for the front side channels. The value of R2 changes to 100k for the back side channels.

### Amplifier Board Fabrication

As is the case for the sensor package board, a PCB is used to layout the designed electronics. The same two tools are used for this layout. The board used for this design is a six layer board. The two outer layers are used for routing and component loading. The four inner layers are used for copper planes with two of them being for ground planes and the inner most two being used for the positive (+3 V) and negative (-3 V) supplies. Figure 4.12 shows the front and back of this fabricated PCB. Sunstone Circuits fabrication procedure is used to create this board. This board is a 4 inch square, which sets the footprint for future additions to this design.

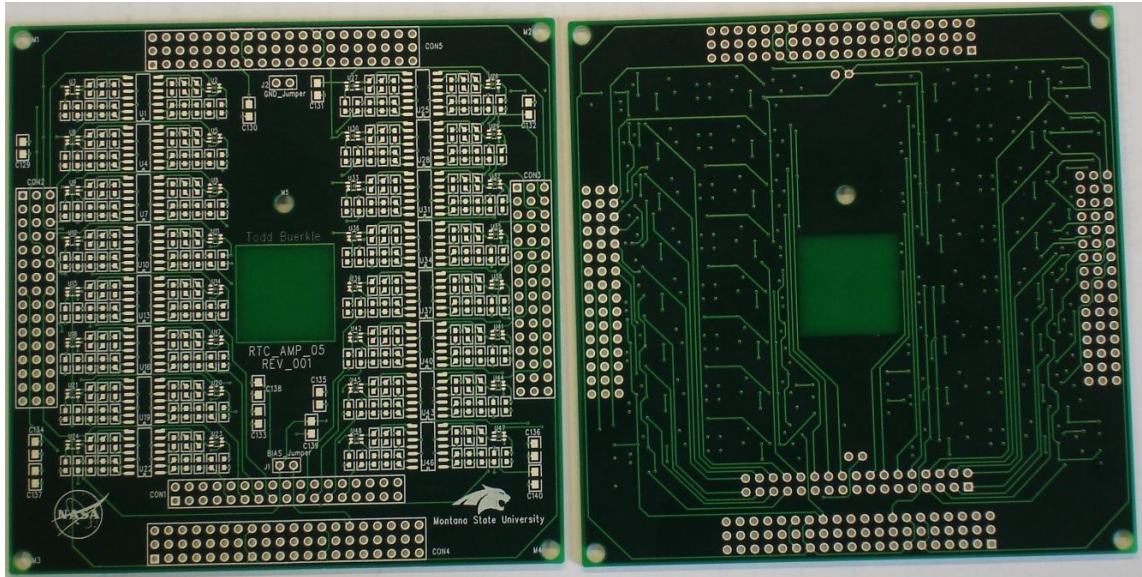


Figure 4.12 Picture showing the front and back side of the fabrication amplifier board. These boards are 4 inches by 4 inches.

Figure 4.13 shows an amplifier board with all of the components loaded.

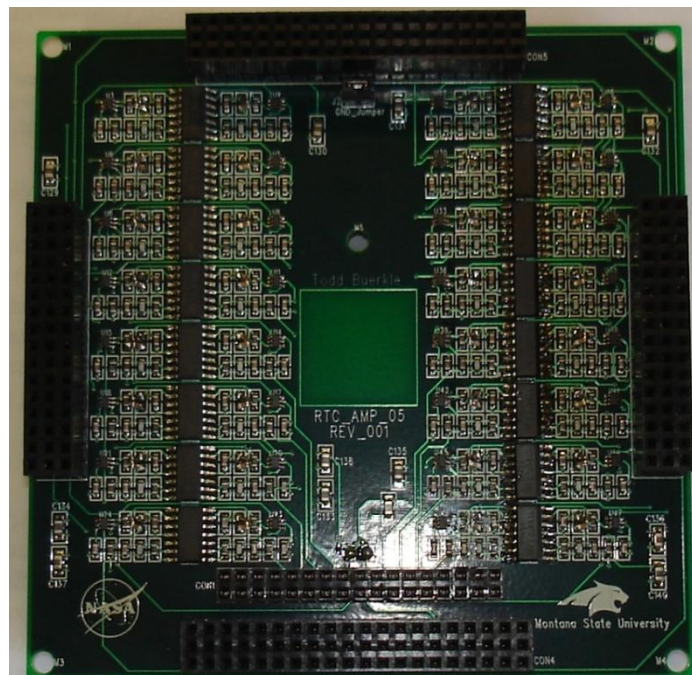


Figure 4.13 Amplifier board picture showing all of the loaded components.

### Additional PCB Designs

A few additional PCBs have also been fabricated in order to aide in the implementation of the radiation sensor and electronics system. The first of these additions is a power board. This board was designed by another graduate student and provides an easy method to connect the required voltages to the amplifier board. The board is the same size as the amplifier board and has the same power connector. Connectors are mounted on the power board that allow banana jacks to be plugged in and then distributed as needed. Figure 4.14 shows a picture of the fabricated power board with all of the components loaded.

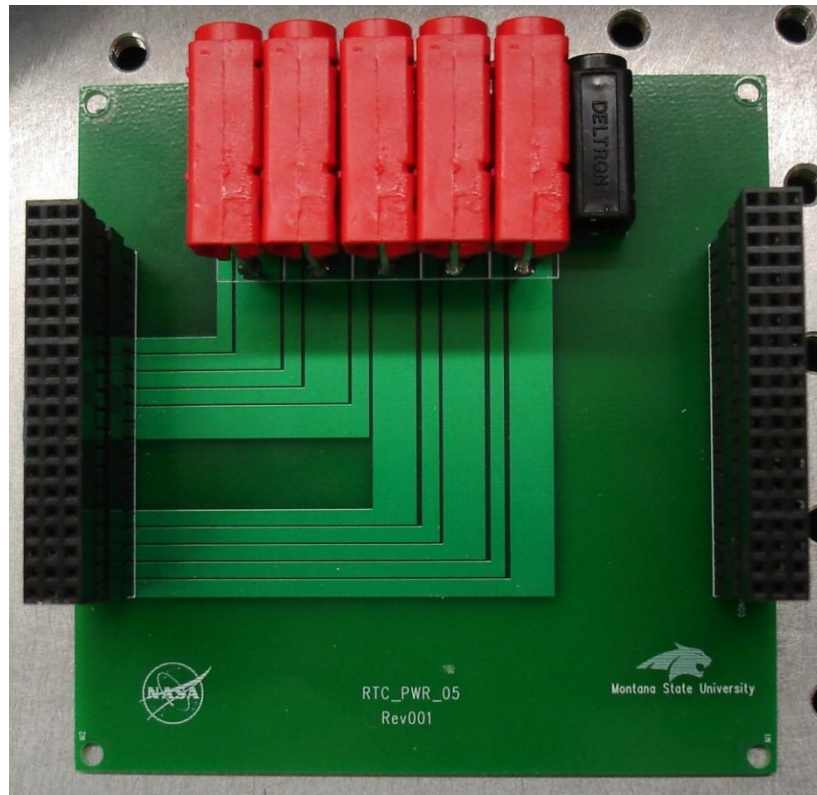


Figure 4.14 Picture of the fabricated power board. This board has the same 4 inch by 4 inch dimensions as the amplifier board.

The second additional board fabricated is a voltage translation board. The output of the electronics is +3 V or 0 V. The FPGA requires +2.5 V as the input. This board consists of a voltage divider for all 32 sensor channels. The divider is designed to reduce the output of the amplifier board to the level required by the FPGA. The outputs of this board are then connected into the FPGA system by a ribbon cable. Figure 4.15 shows this translation board. Figure 4.16 shows the final stacked assembly for this design.

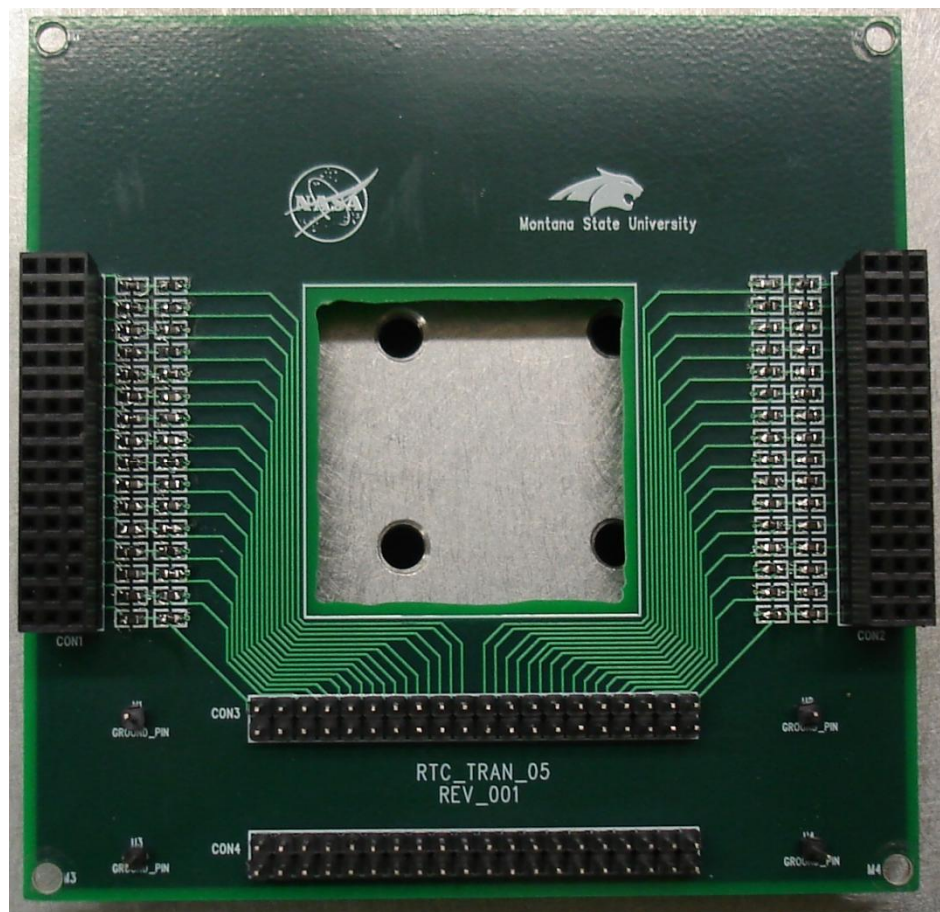


Figure 4.15 Picture of the loaded voltage translator board created on a 4 inch by 4 inch PCB.

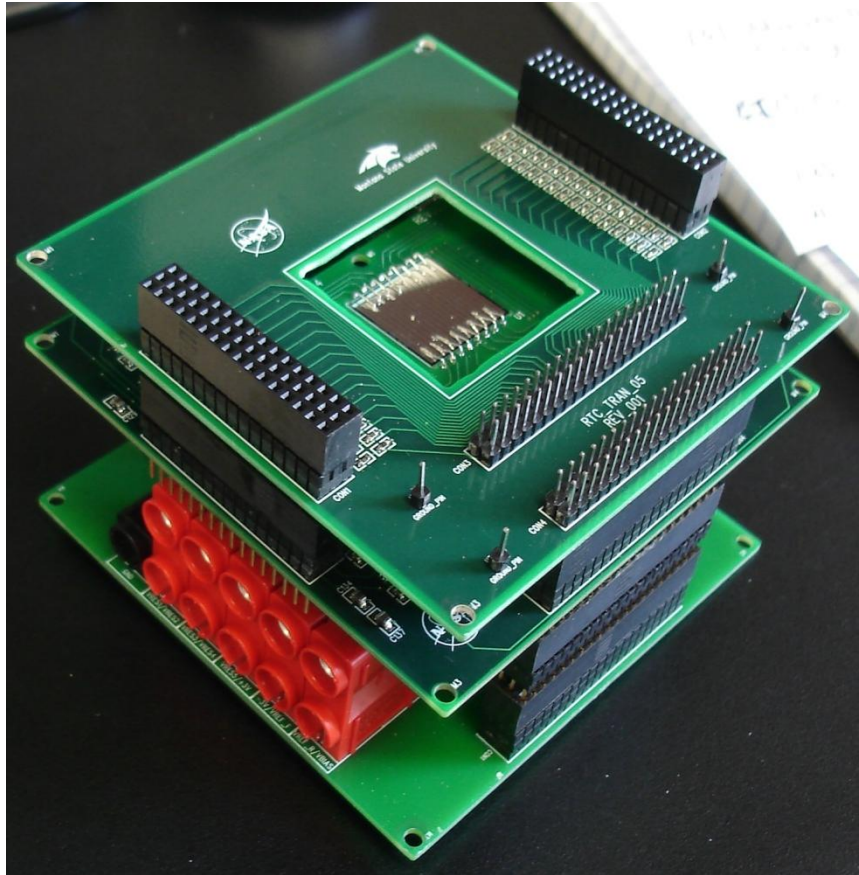


Figure 4.16 Picture of the stacked radiation sensor system assembly. Each board is a 4 inch square, with the entire stack standing about 2.25 inches high.

### High Speed Event Detector Implementation

The FPGA computer system for this design is implemented on a Virtex 6 FPGA. This component is loaded onto a ML605 board. The high speed event detector design that was previously discussed is also implemented on this FPGA. The parameters of this FPGA set some of the performance characteristics for the event detector. These performance metrics are summarized in Table 4.3.

The FPGA in this design sets the sample rate of the event detector to 121.2 ns due to the system clock for this device. As long as the designed electronics output a pulse

that is at least 121.2 ns wide, the event detector will log this strike and relay the information to the rest of the FPGA system.

TABLE 4.3  
EVENT DETECTOR PERFORMANCE METRICS

Symbol	Quantity	Value
$f_{\text{sys}}$	System Clock	66 MHz
$f_{\text{div}}$	Divided System Clock	8.25 MHz
$T_{\text{sys}}$	System Period	15.15 ns
$T_{\text{sample}}$	System Sample Rate	121.2 ns
$T_{\text{C}}$	Counter Update Rate	121.2 ns

Figure 4.17 shows a picture of the FPGA board used to implement both the event detector and the rest of the FPGA based computer system.

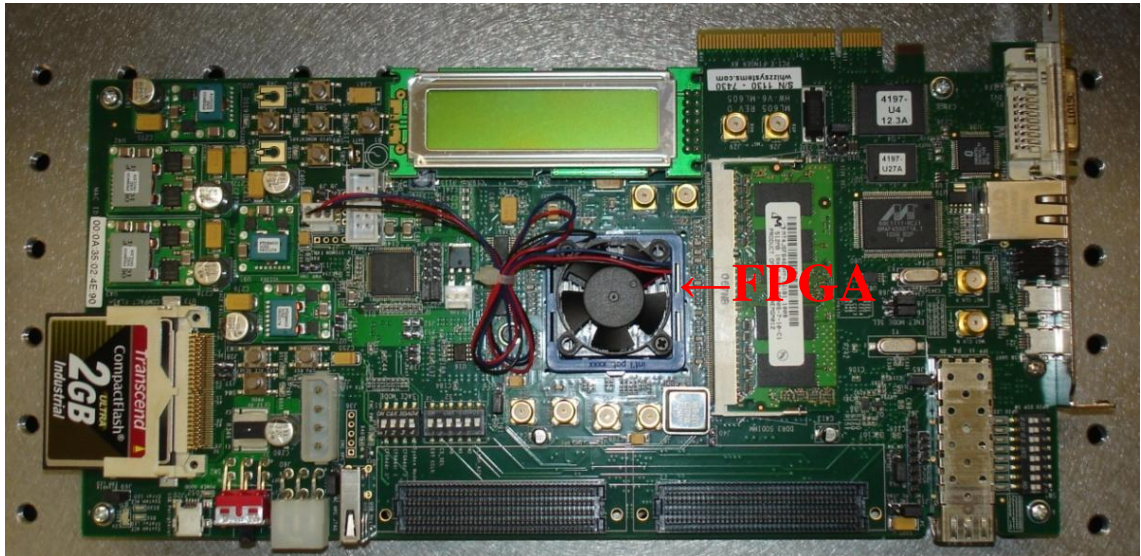


Figure 4.17 FPGA board used to implement the event detector and the rest of the fault tolerant computing system.

## CHAPTER FIVE – RADIATION TESTING

Cyclotron Testing at Texas A&M University

The previously discussed design was assembled and taken to the facility at Texas A&M University for testing. The 25 MeV krypton ion is selected as the radiation source for these tests. Due to the current tuning of the beam, the actual energy of this ion is 21.8 MeV instead of the nominal value. This means that the ion will only penetrate through about 275  $\mu\text{m}$  of the sensor. Without the ionization of the entire thickness of the sensor, observing strikes on the back side channels is going to be more difficult. This lower energy will be analyzed later in the developed model in order to update the predictions to reflect the actual beam achieved during testing.

The system is now setup for the radiation testing. Six different shields are used in this testing process. Three of the shields have a 0.125” diameter hole and the other three have a 0.04” diameter hole. The locations of these holes allows for the stimulation of nine different sensor locations. Two of the shields (one large and one small hole shield) have the hole that exposes the center of the sensor. Another two shields (one large and one small hole shield) have a hole that exposes an edge of the sensor. This allows for the top, right, bottom, or left side of the sensor to be stimulated by rotating the shield 90°. The final two shields (one large and one small hole shield) have a hole that exposes a corner of the sensor. These shields allow for the stimulation of the top right, bottom right, bottom left, and top left corners of the sensor again by rotating the shield 90°.

Between these six shields, 18 different experiments (9 different locations for 2 different size holes) can be performed on the radiation sensor system.

The previously determined amplifier gains are a rough estimate of the actual values needed to effectively monitor radiation strikes. For this reason, the electronics boards used during this testing have a range of gains. Three different gains are used for both the front and back side electronics. This allows the sensor outputs to experience different amplification and pulse shaping depending on where the Kr beam is aimed.

Table 5.1 shows the gains used for each of the channels on the amplifier board.

TABLE 5.1  
AMPLIFIER BOARD GAINS

Sensor Channels	Integrator Gain	Amplifier Gain	Total Gain	Gain Classification
Front				
F1 – F5	100,000	10	1,000,000	Low
F6 – F11	100,000	100	10,000,000	Medium
F12 – F16	100,000	1,000	100,000,000	High
Back				
B1 – B5	100,000	1	100,000	Low
B6 – B11	100,000	10	1,000,000	Medium
B12 – B16	100,000	100	10,000,000	High

With these variable gains, it is hypothesized that at least one location will be able to record both front and back side strikes. After testing, the gains that performed the best will be used for future amplifier boards.

In addition to the variable gains, the radiation sensor electronics only respond to transient effects. For this reason, the Kr beam needs to be pulsed. This pulsing response

was provided by the control room by phasing and de-phasing the ion beam. The pulse width achieved by this pulsing scheme is 100 ms at a 1 Hz rate. With this pulse rate, the fluence of the ion beam provides an average number of ions/cm<sup>2</sup> during the 100 ms pulse width and 0 Kr ions during the 900 ms off time. This ion count is an average count recorded by four detectors located in the beam line. Each of these detectors has a sensing area of 0.1 cm<sup>2</sup>. Multiplying this area by the ion fluence gives the total ions counted by the detectors in the beam line. This value will vary depending upon the test, since each run of the beam is slightly different. The total number of Kr ions is spread across the entire spot size for the radiation beam. Due to the shields used for this testing, only a fraction of these Kr ions are going to reach the radiation sensor. The number of ions that actually hit the sensor is determined later using the developed correlation model.

The data for these tests is logged on a computer GUI that registers the counts seen on every individual channels as well as the counts on all 256 intersections. This GUI is updated five times a second during the testing and the total counts on every channel is logged every 5 – 10s. After logging the data, counts displayed on the GUI are reset. The assembly is mounted in the beam line and the testing is started. For all of these tests, no bias voltage is applied to the sensor and the bias connections are simply grounded. The length of the test runs ranges from 5 minutes to 10 minutes depending on the test. In all, 19 different experiments are performed on the system. Figures 5.1 and 5.2 show the location of these different runs. Test run #6 is not included because this test did not include any data due to the beam cap still being on during testing.

Test run data is produced by the control software after each experiment. This data includes information about the average flux, effect fluence, uniformity, and many other parameters. The run file for each of these tests is included in Appendix D.

#7	#2	#8	Large Aperture (0.125")
#5	#1	#3	
#10	#4	#9	

Figure 5.1 Location of the radiation test runs for the large aperture shields.

#18	#12/ 16	#19	Small Aperture (0.04")
#17	#11	#13	
	#14/ 15		

Figure 5.2 Location of the radiation test runs for the small aperture shields.

The total counts are logged on all of the channels during the run. After the tests are completed, plots are made for all of the runs that show the counts per second on every

X and Y channel as well as the counts on the 256 intersection counters. The following plots show the result of these tests. Figure 5.3 shows the results from test run #7.

Test #7 (Large Hole, Low Gain Front, High Gain Back)

Strike Location:

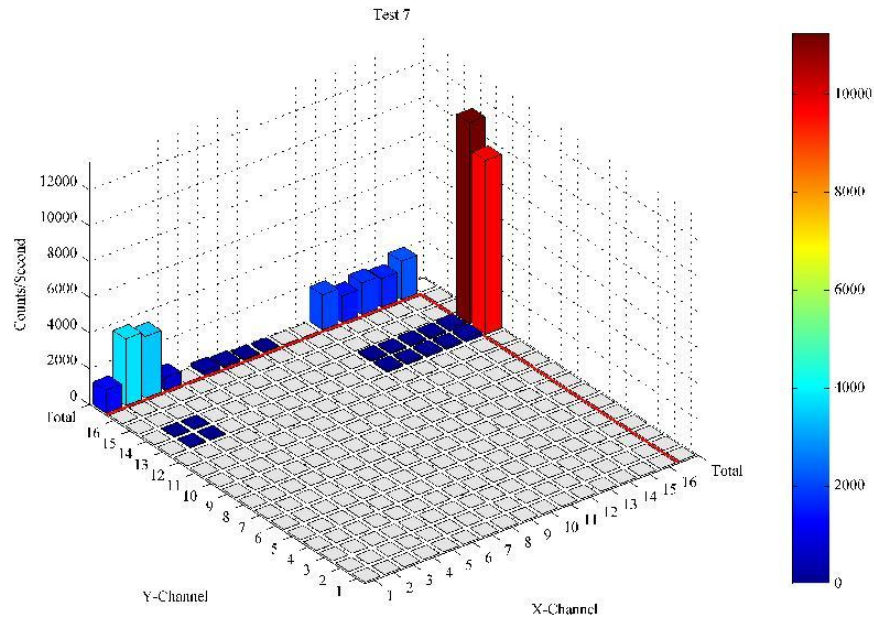


Figure 5.3 Radiation test data for test run #7.

For this test, the beam is aimed at the upper left corner of the radiation sensor with the large aperture shield in place. This means that the front side electronics for these channels have a low gain and the back side electronics have a high gain. This high gain allows for the back side channels to observe counts. A few intersections are even observed when the beam is pulsed in this location. Table 5.2 shows the average counts per second observed on each channel with the beam in this location. Only the individual channels that the beam is directly aimed at are included and intersections are omitted.

Since this test included the low gain front side channels and high gain back side channels, these are the channels shown in Table 5.2.

TABLE 5.2  
AVERAGE COUNTS PER SECOND FOR TEST #7

Sensor Channels	Average Counts per Second
Front Channels	
F1	1283
F2	3730
F3	3438
F4	704
F5	0
Total for Front	9155
Back Channels	
B16	9
B15	5
B14	11248
B13	9736
B12	11
Total for Back	21009

The intersection is not located at a single point due to the spot size produced by the large aperture shield which causes multiple intersections to be hit at one time. The effect of this is a larger intersection point. Regardless of the increased spot size, this proves that the sensor system is able to produce an intersection point for a radiation strike. The number of counts observed on these intersection channels is only about 25 per second. Different gains need to be used in order to observe a more accurate number of intersection counts.

The higher gain channels (12 – 16) on the front side observe a large number of counts and the medium gain channels (5 – 11) observe a few counts even though the radiation beam is not aimed at these channels. This effect is the result of the gain on these channels.

Charge that is produced outside of the depletion regions is not collected right away. Some charge produced outside of the depletion region will diffuse into these regions and be collected. The charge that does not end up in a depletion region can either recombine or diffuse laterally (across the sensor instead of up or down). Some of the charge will recombine, while some amount of charge will laterally diffuse throughout the sensor. The high gain channels are able to convert this diffused charge into a large number of counts, while the medium gain channels produce only a small number of counts from the diffused charge. These artificial counts could be eliminated by reducing the gain on the front side channels. Another hypothesis is that biasing the sensor would either completely eliminate or drastically reduce this lateral diffusion effect. This theory will be tested during future testing due to time constraints. The artificial nature of these counts is the reason that they are not included in Table 5.2.

Figure 5.4 shows the results of test run #2. This means that the beam was aimed at the upper, middle section of the radiation sensor with the large aperture shield in place. The front side electronics for the channels in this location have a medium gain, while the back side electronics for these channels have a high gain. Again, this high gain is necessary to observe back side strikes due to the fact that the ion beam does not pass completely through the sensor. Once again, an intersection spot is produced instead of a

single location. This is still an effect of the spot size produced by the large aperture shield. The high gain front side channels are now able to produce even more artificial counts due to the decreased diffusion distance when compared to Test #7. The low gain front side channels did not produce any false counts due to lateral diffusion. This gives a rough idea of the front side gain threshold necessary to eliminate the counts produced by lateral diffusion.

Test #2 (Large Hole, Mid Gain Front, High Gain Back)  
Strike Location:

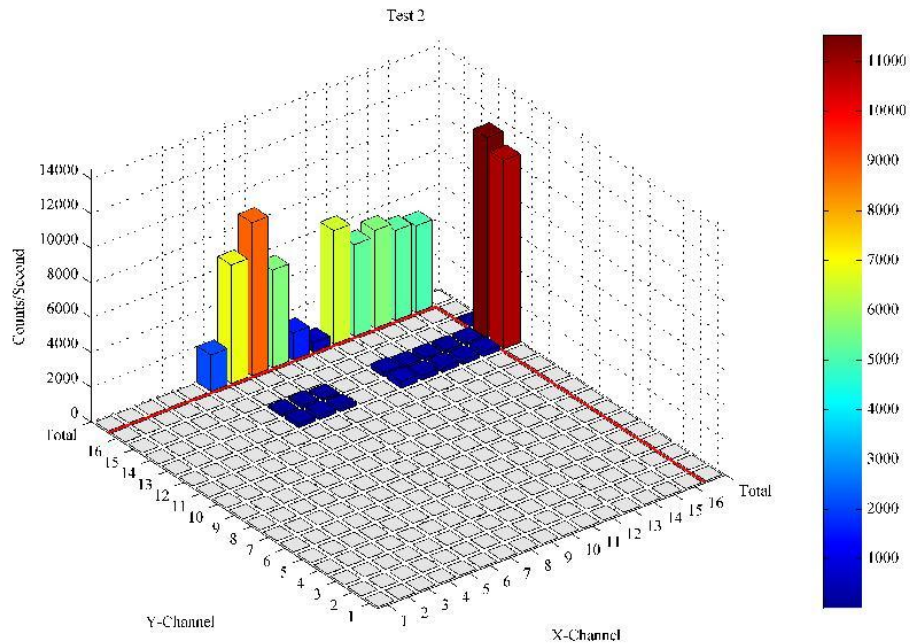


Figure 5.4 Radiation test data for test #2.

Table 5.3 shows the average number of counts per second for the channels in this test.

Due to the location of the beam, the channels included in Table 5.3 are the medium gain

front channels and the high gain back channels. Only the channels that are directly hit by the radiation beam are included in this table (artificial counts are ignored).

TABLE 5.3  
AVERAGE COUNTS PER SECOND FOR TEST #2

Sensor Channels	Average Counts per Second
Front Channels	
F6	2100
F7	6828
F8	8816
F9	5622
F10	1559
F11	547
Total for Front	25472
Back Channels	
B16	0
B15	20
B14	11529
B13	10873
B12	9
Total for Back	22431

The intersection spot for this particular test shows a few counts. These six intersection points have between 100 – 230 counts per second. The increased front side gain caused the front side output pulse width to increase, which enabled more intersections to occur for this test.

Figure 5.5 shows the results of test run #8. For this test, the beam is aimed at the top right corner of the radiation sensor with the large aperture shield in place. The electronics for the sensor channels in this corner have high gains for both the front and

back side. High gains on both front and back electronics maximize the number of potential intersections. This combines with the spot size due to the large aperture shield to produce intersection spot size that is shown in Figure 5.5.

Test #8 (Large Hole, High Gain Front, High Gain Back)

Strike Location:

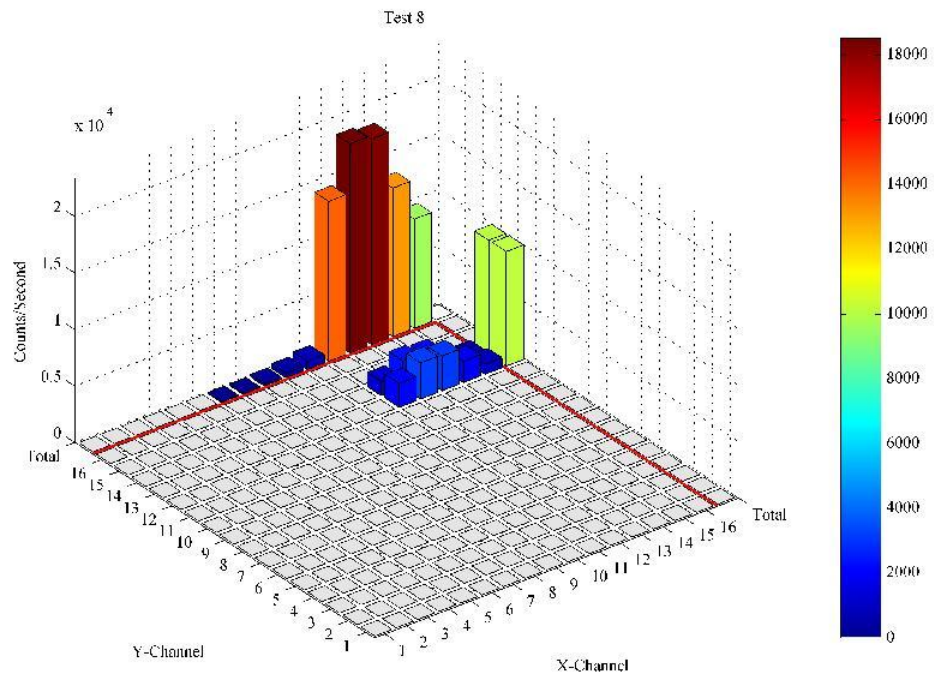


Figure 5.5 Radiation test data for test run #8.

The medium gain front side channels still produce a few artificial counts for this test run. Table 5.4 shows the average counts per second for the channels aimed at during this test, which are the high gain front and back side channels. The artificial counts as well as the intersection counts are not included in this table. The intersection locations for this particular test show between 500 – 3000 counts per second. The more directly hit

locations display the high end of this count range. This makes it clear that high front and back gain lead to a maximum number of intersection counts, but the high gain front side channels will produce artificial counts. For this reason, the ideal gains for this ion beam are low front side gain and high back side gain.

TABLE 5.4  
AVERAGE COUNTS PER SECOND FOR TEST #8

Sensor Channels	Average Counts per Second
Front Channels	
F12	14152
F13	18510
F14	18213
F15	13141
F16	9657
Total for Front	73673
Back Channels	
B16	3
B15	21
B14	10120
B13	10137
B12	1
Total for Back	20282

The total back side counts observed for these three different tests remained relatively constant. This is reassuring since these three tests all involved aiming the beam at the high gain back side channels. The small differences observed between these numbers are due to variations in the beam fluence during these tests. Table 5.5 shows the effective fluence and the ion count for each of the previously discussed test runs. The ion count is calculated by multiplying the effective fluence by the  $0.1 \text{ cm}^2$  area of the particle

detectors in the beam line. The average fluence for the rest of the experiments can be found in the run data located in Appendix D.

TABLE 5.5  
EFFECTIVE PARTICLE FLUENCE FOR TESTS 2, 7, AND 8

Test Number	Effective Particle Fluence (ions/cm <sup>2</sup> )	Ion Count
#2	1,258,000	125,800
#7	1,409,000	140,900
#8	1,210,000	121,000

The highest effective fluence, during test #7, produced the highest number of back side counts, where as the lowest effective fluence, during test #8, produced the lowest number of back side counts.

The lateral diffusion counts in all of the previous analysis can be ignored since these are the product of charge produced outside of the radiation sensor's depletion regions. Almost all of the front and back side signals are caused by the charge produced inside of the depletion regions or within a short diffusion length. This means that the counts produced by lateral diffusion do not cause a reduction in the total counts seen on the directly hit channels.

These three tests are displayed because intersections are observed during the data set. The plots for the rest of the test runs can be seen in Appendix E. Included in these additional tests are the remaining large aperture locations as well as all of the locations for the small aperture. A majority of these additional tests only display counts on the

front side channels due to the beam being aimed away from the high gain back side channels.

### Correlating Measured Data and the Developed Radiation Sensor Model

A large amount of data about the performance of the radiation sensor was collected during the Cyclotron testing. Now it's time to further develop the model to allow for a better correlation. The goal of this new model is to allow for the prediction of the counts per second based on the ion selected. For this analysis, the Kr ion is still used. The energy of this ion is set to 21.8 MeV since this was the energy actually observed during the radiation testing. The same model as before will be used initially, except this new ion energy is input into the SRIM software. The charge profile for a single ion strike is produced using the same procedure as before and can be seen in Figure 5.6.

Figure 5.6 clearly shows that the ion does not make it the entire way through the sensor, a result of the decreased ion energy. As already expected, this reduces the back side signals since charge is only produced in a portion of the depletion region. Using the new charge profile, the front and backside currents for a single ion strike are calculated using the same approach as before. Once again, the data produced is imported into DxDDesigner and plotted. The hole and electron current can be seen in Figure 5.7 and Figure 5.8 respectively. These two current plots show the same shape as those derived previously except that the magnitude of these signals is decreased as a result of the lower ion energy.

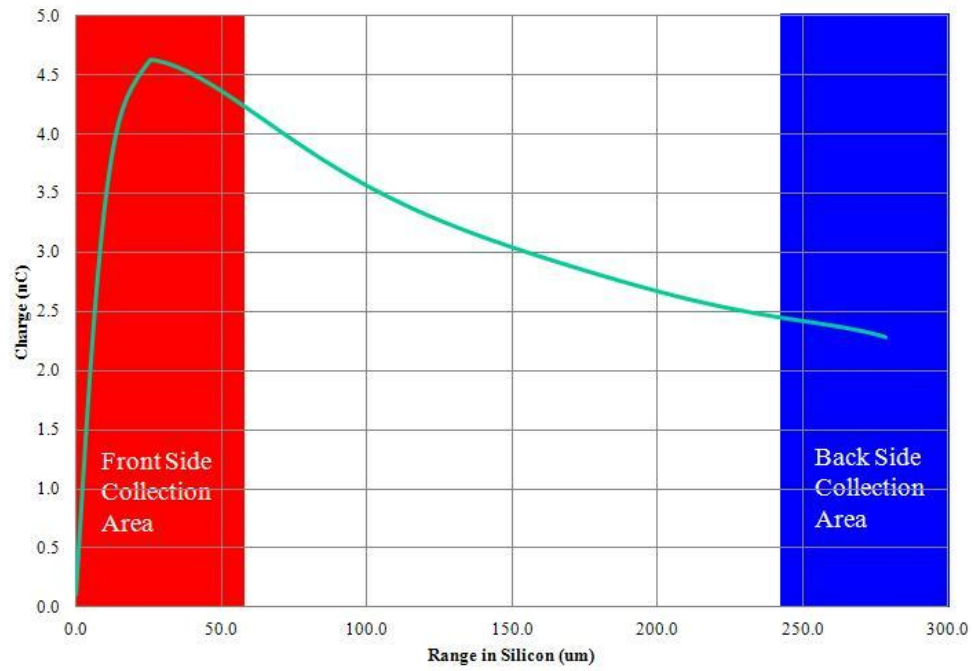


Figure 5.6 Charge profile for the 21.8 MeV Kr ion in the radiation sensor.

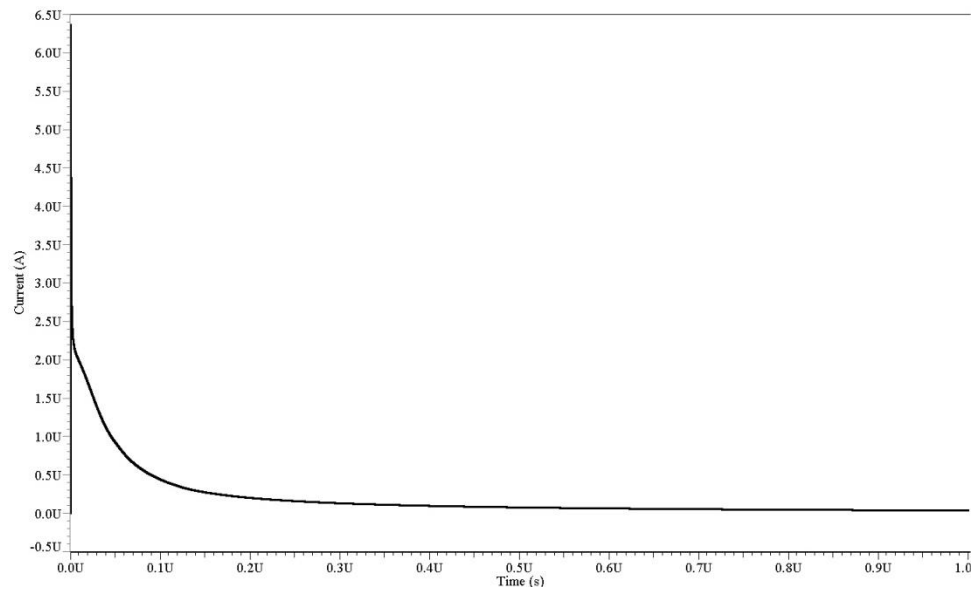


Figure 5.7 Hole (front) current produced out of the sensor for a 21.8 MeV Kr ion strike.

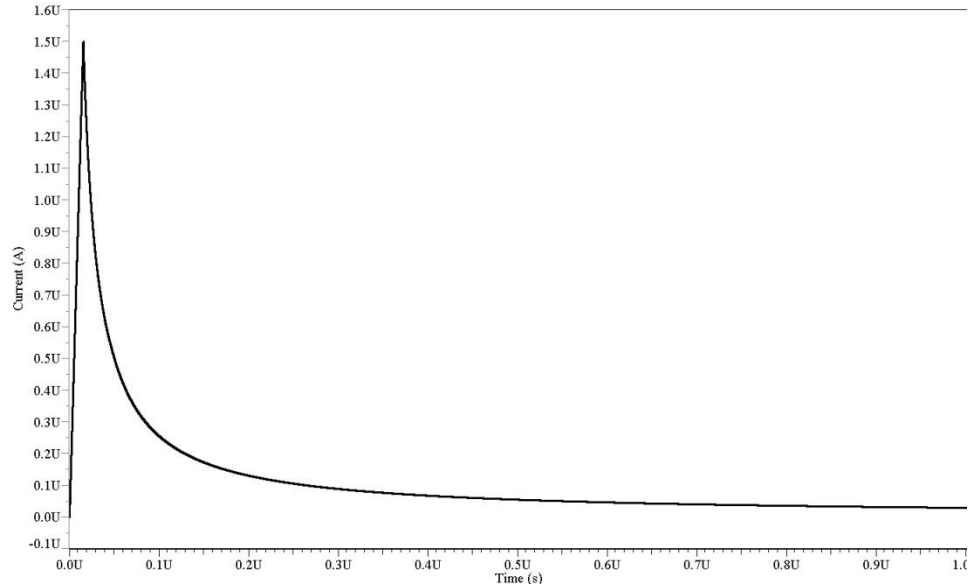


Figure 5.8 Back side (Electron) current produced out of the sensor for a 21.8 MeV Kr strike.

The output currents are now known for the sensor when hit by a 21.8 MeV Kr ion. This output current is now input into the electronics chain. This simulation is setup in DxDesigner by importing the above current waveforms and using them as the input to the sensor electronics. Only the first two stages of the amplifier chain are used since this is all that is completely necessary to determine the output. Also, an op-amp model for the comparator is not readily available in DxDesigner so this stage is omitted. The last stage can be treated like a Boolean operation. If the output of the inverting amplifier is greater than 2.75 V, then the output of the comparator will be 3.0 V. This gives a threshold that can be applied to the output of the inverting amplifier. These simulations are performed for each of the three gains used in the front and back side channels electronics. Figure 5.9 shows the circuit used to simulate these two current inputs.

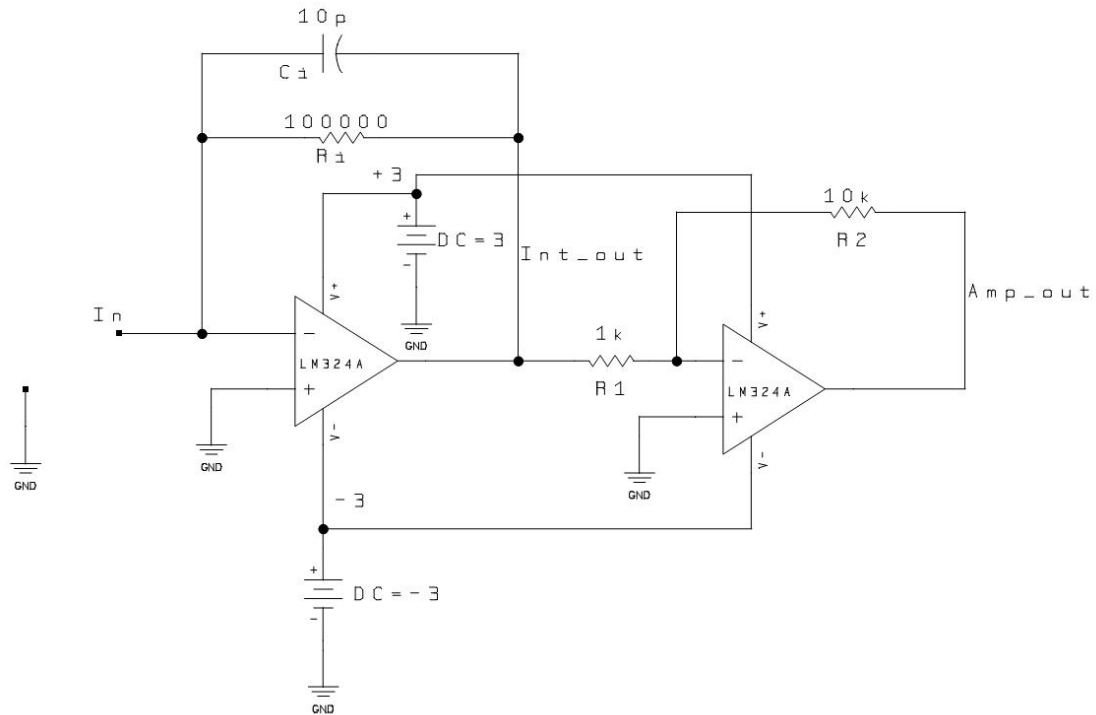


Figure 5.9 DxDesigner schematic that is used to simulate the currents produced by a 21.8 MeV Kr strike.

The resistor R2 is simply changed for each of the different simulations. By keeping R1 constant, the value of R2 is used to set the inverting amplifier gain to the desired level for each of the three different sets of gains on the front and back side electronics.

The front side hole current, shown in Figure 5.7, is simulated for the three different inverting amplifier gains of 10x ( $R2 = 10 \text{ k}\Omega$ ), 100x ( $R2 = 100 \text{ k}\Omega$ ), and 1000x ( $R2 = 1000 \text{ k}\Omega$ ). The following plots show the output of the inverting amplifier for the input current shown in Figure 5.7. Figure 5.10 shows the output of the inverting amplifier with a gain of 10x, Figure 5.11 shows the output of the inverting amplifier with

a gain of 100x, and Figure 5.12 shows the output of the inverting amplifier with a gain of 1000x for the front side current (holes).

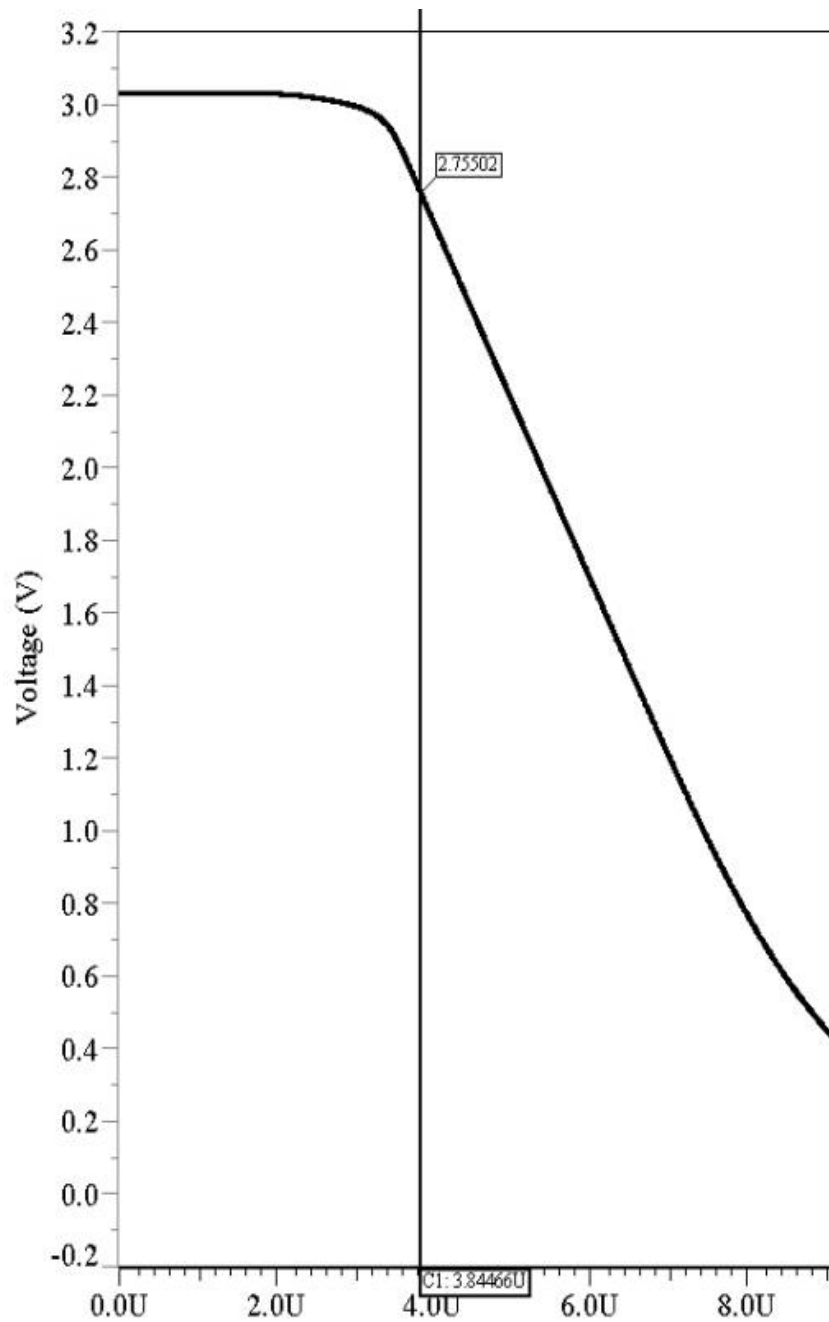


Figure 5.10 Output of the 10x gain inverting amplifier for the front side current produced by a single 21.8 MeV Kr ion.

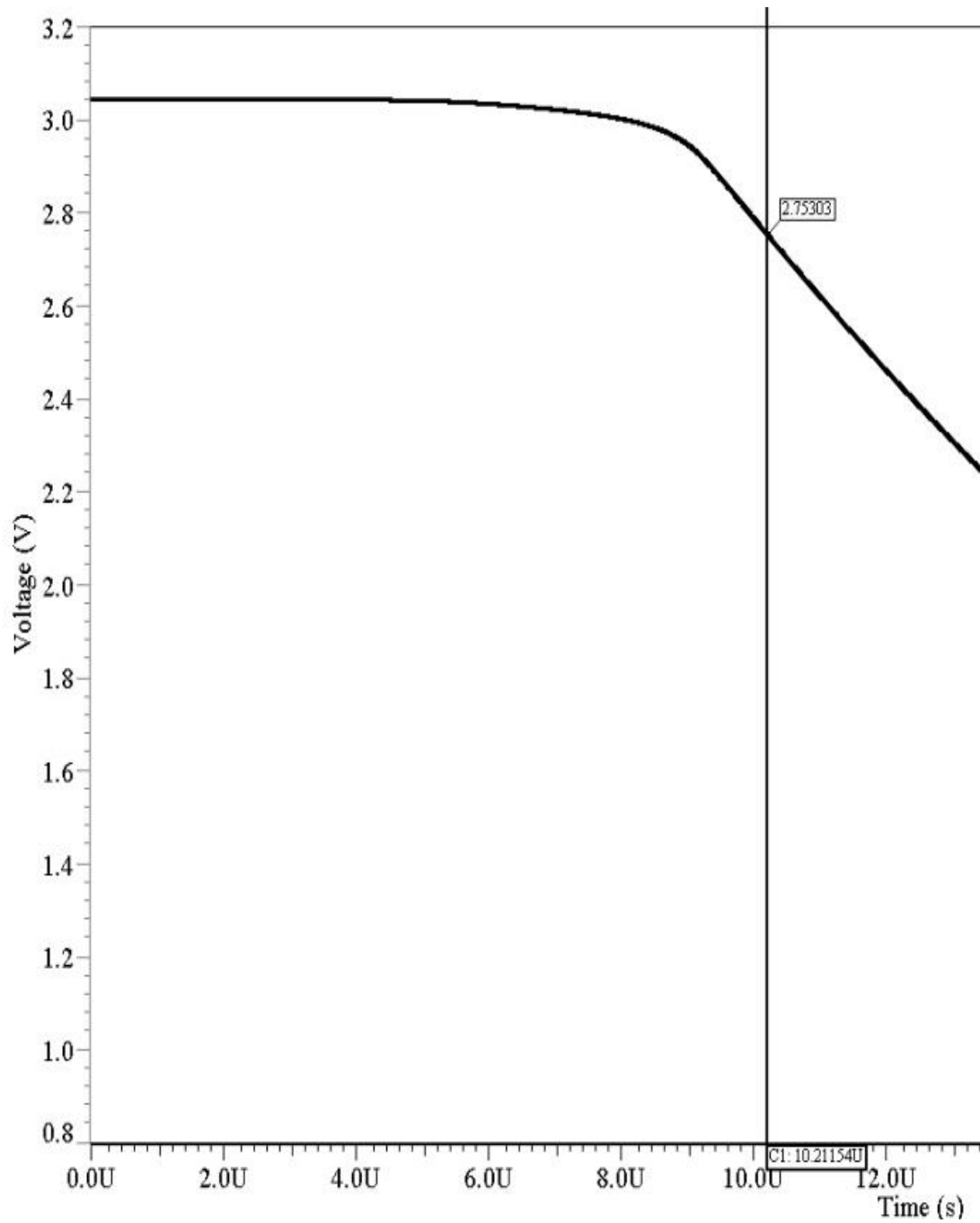


Figure 5.11 Output of the 100x gain inverting amplifier for the front side current produced by a single 21.8 MeV Kr ion.

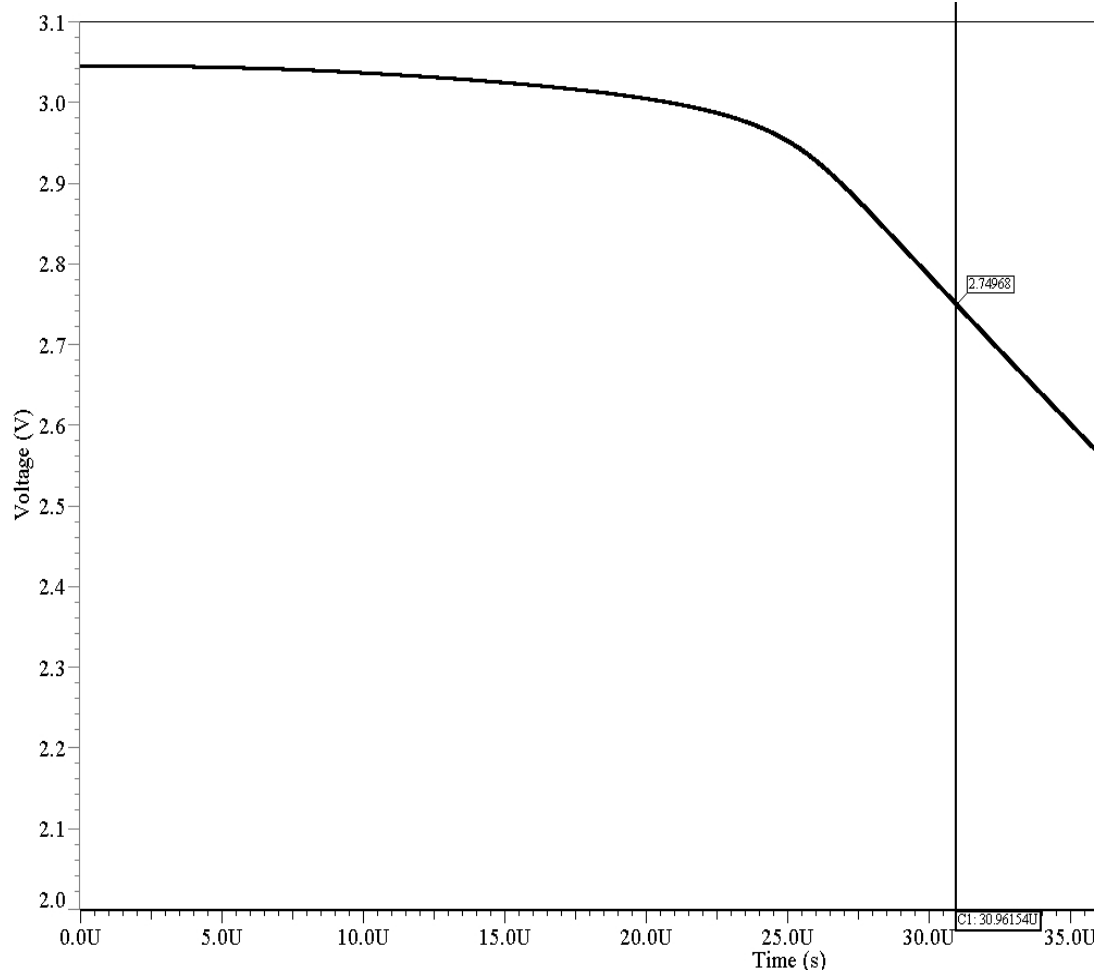


Figure 5.12 Output of the 1000x gain inverting amplifier for the front side current produced by a single 21.8 MeV Kr ion.

These results show the output pulse widths that are achieved for the front side electronics when the radiation sensor is struck by a single 21.8 MeV krypton ion. Given the small pulse width of the input current (on the order of hundreds of nanoseconds), these output pulse widths seem reasonable for the given electronics. One of the goals of this electronics chain is to stretch the input pulse into a more usable output pulse. These plots prove that this is accomplished by this set of electronics. Additional pulse stretching is most likely added into this system by the slew rates for the particular op-

amps chosen. The slow slew rate of the LMV324 op-amps adds to the pulse stretching effect of the entire circuitry.

The back side electron current, shown in Figure 5.8, is simulated for the three different inverting amplifier gains of 1x ( $R_2 = 1 \text{ k}\Omega$ ), 10x ( $R_2 = 10 \text{ k}\Omega$ ), and 100x ( $R_2 = 100 \text{ k}\Omega$ ). The following plots show the output of the inverting amplifier for this input current. Figure 5.13 shows the output of the inverting amplifier with a gain of 1x, Figure 5.14 shows the output of the inverting amplifier with a gain of 10x, and Figure 5.15 shows the output of the inverting amplifier with a gain of 100x for the back side current (electrons).

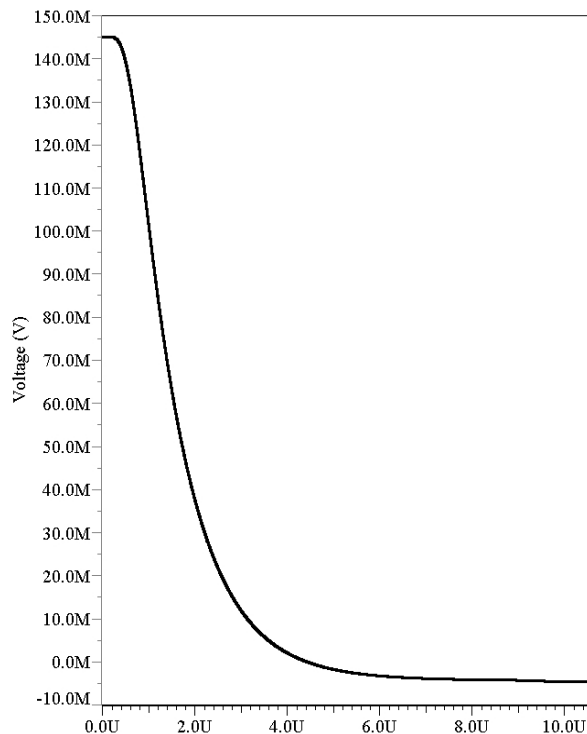


Figure 5.13 Output of the 1x gain inverting amplifier for the back side current produced by a single 21.8 MeV Kr ion.

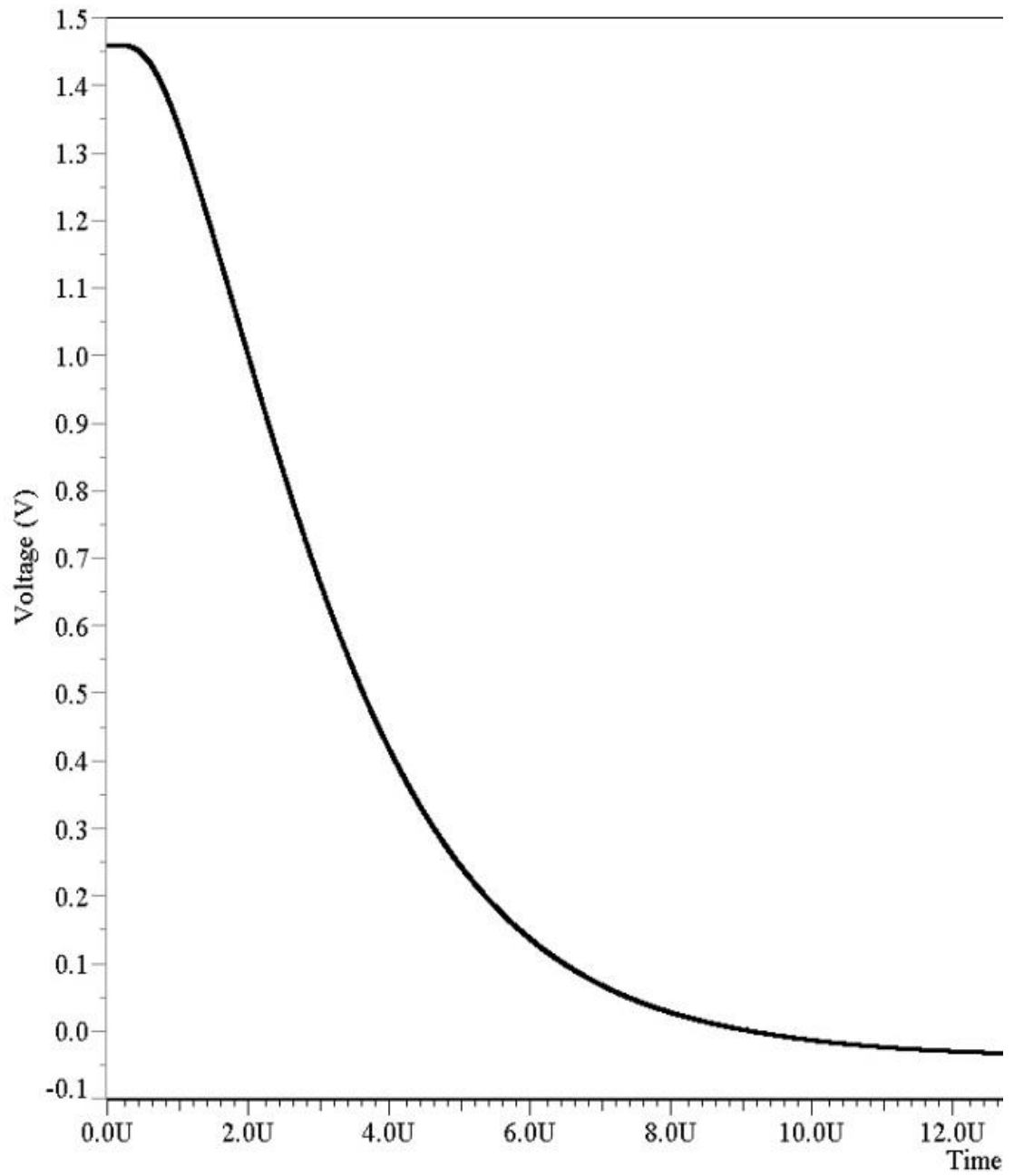


Figure 5.14 Output of the 10x gain inverting amplifier for the back side current produced by a single 21.8 MeV Kr ion.

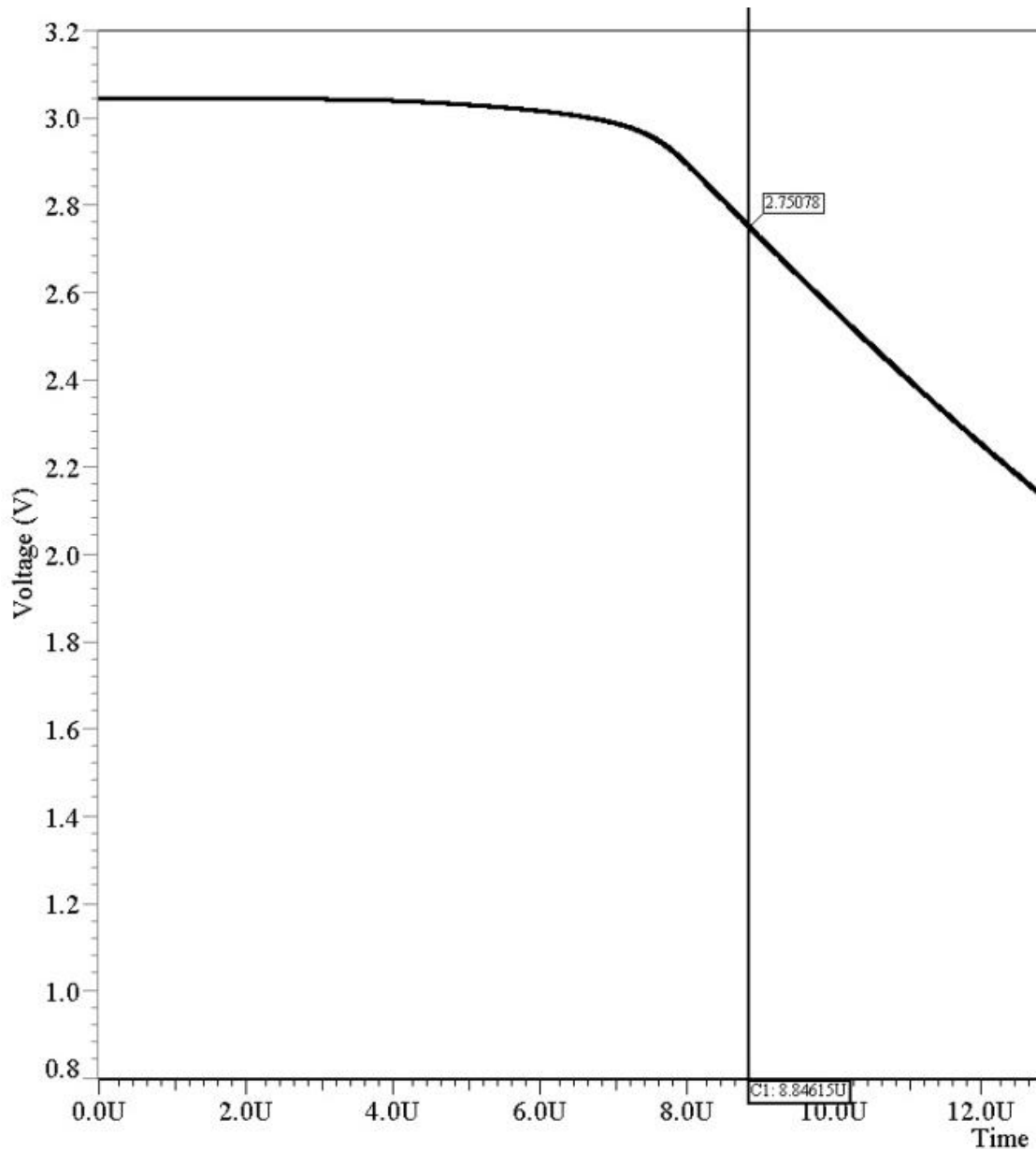


Figure 5.15 Output of the 100x gain inverting amplifier for the back side current produced by a single 21.8 MeV Kr ion.

The previous results show the output pulse widths that are achieved for the back side electronics when the radiation sensor is struck by a single 21.8 MeV krypton ion.

Four of these plots (Figure 5.10, 5.11, 5.12, and 5.15) clearly show a saturated output

that is produced by the high gain for these particular channels. Table 5.6 summarizes the output pulse widths that are achieved for these six different simulations.

TABLE 5.6  
OUTPUT PULSE WIDTHS FOR FRONT AND BACK SIDE ELECTRONICS FOR A SINGLE  
KRYPTON ION STRIKE

Electronics Gain	Output Pulse Width ( $\mu\text{s}$ )
Front Side Channels	
Low Gain	3.84
Medium Gain	10.21
High Gain	30.96
Back Side Channels	
Low Gain	0
Medium Gain	0
High Gain	8.85

No output pulse width is achieved on the low and medium gain back side channels because the electronics for these channels are unable to amplify the input current to a level higher than the 2.75 V threshold. Assuming that these are the output pulse widths seen by the event detector then the number of counts recorded can be predicted. In order to predict the number of counts, the total number of ions that hit the radiation sensor needs to be determined. The final ion count is a product of the ion beam fluence, aperture size, and aperture location with respect to the radiation sensor channels. By calculating an ion density that hits the sensor, the final ion count is determined. The follow calculations show how to produce this ion density and how to use this value to find the number of ions that hit a particular sensor location.

For each output pulse of the ion beam, a particle density is produced, due to the volume of the beam line, the pulsing of the beam, and the number of ions contained in each beam pulse. This produces a cylindrical volume containing a certain number of ions. Figure 5.16 shows a representation of one potential particle density with a random number of krypton ions contained in a cylindrical volume.

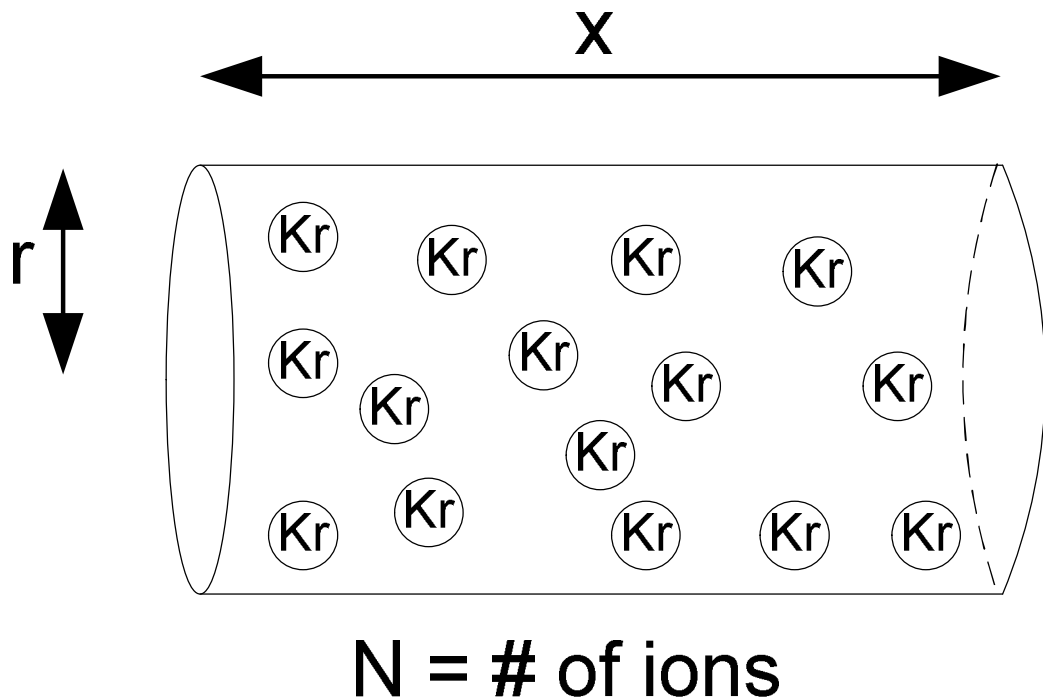


Figure 5.16 Drawing that shows the particle density that is produced by the radiation shields and the pulsing of the beam.

The energy of each ion is known from the radiation sensor testing experimental data. This energy is provided in MeV/amu for the ion selected. Using (5.1) gives the particle energy for the selected ion.

$$E(eV) = \left( \frac{MeV}{amu} \right) \cdot ion\_atomic\_mass(amu) \quad (5.1)$$

By multiplying the energy in MeV/amu by the atomic mass of the ion in amu, the total ion energy is found. The ion energy, which is the kinetic energy of the ion, is converted from eV to Joules. This is accomplished using (5.2). This energy conversion requires that the particle energy is represented in units of eV.

$$KE(Joules) = E(eV) \times (1.602 \times 10^{-19}) \quad (5.2)$$

The kinetic energy is then used to determine the velocity of the ion. The velocity is found using (5.3).

$$v = \sqrt{\frac{2KE}{m}} \quad (5.3)$$

In (5.2), KE is the previously determined kinetic energy in Joules and m is the mass of the ion in kilograms. Once the velocity is known, the length of the 100 ms ion beam pulse width is determined using (5.4).

$$x = v \times t \quad (5.4)$$

The variable t in (5.4) represents the 100 ms pulse width of the ion beam. The distance x represents the total length of the ion distribution as shown in Figure 5.16. The volume for the ion beam pulse is now found using (5.5) or (5.6) depending on if the beam has a circular or square cross section.

$$Vol = \pi \times r^2 \times x \quad (5.5)$$

$$Vol = y \times z \times x \quad (5.6)$$

In (5.5),  $r$  is the radius of the beam for a circular cross section. In (5.6)  $y$  and  $z$  are the outer dimensions for a square beam cross section. The total number of ions,  $N$ , contained in the calculated volume is found from the ion effective fluence. This fluence is used in (5.7) to find the ion count.

$$N = \text{Effective\_Fluence} \times 0.1 \quad (5.7)$$

In (5.7), the effective fluence of the ion is in units of ions/cm<sup>2</sup> and can be found in the beam run data sets (Appendix D). The factor of 0.1 is used since this is the sensing area of the beam line detectors that were discussed earlier. This calculation provides the total number of ions in one beam pulse. With the number of ions known, the ion density can be found using (5.8).

$$n = \frac{N}{Vol} \quad (5.8)$$

The value,  $n$ , is the ion density for an output pulse of the radiation beam.

Using the previous calculations, the ion density is now calculated for the three different test runs. In order to find the ion beam cross section in the beam line, Figure 5.17 is used [20]. The dimensions in this figure are in inches. Converting these dimensions to meters and using (5.6) gives the volume of the beam line in m<sup>3</sup>. With these parameters known, the ion density for test #2 is calculated using the previous equations. The results of this analysis are summarized in Table 5.7.

The same calculations were also performed for test #7 and #8. The only change to the process is substituting in the correct effective fluence for each test run. Table 5.8

shows the ion densities achieved during the three different tests for the three different ion fluences.

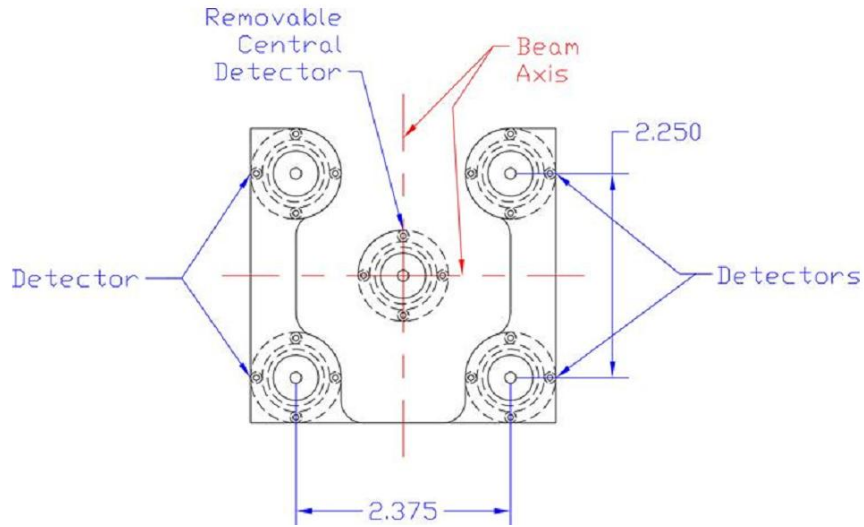


Figure 5.17 Orientation of detectors in the beam line [20].

TABLE 5.7  
CALCULATION OF THE ION DENSITY FOR TEST #2

Parameter	Value	Units
Energy(E)	21.8	MeV/amu
Mass(m)	83.912	amu
Energy (E)	$1.829 \times 10^9$	eV
Energy (E)	$2.93 \times 10^{-10}$	J
Mass (m)	$1.559 \times 10^{-25}$	kg
Velocity (v)	$6.131 \times 10^7$	m/s
Length (x)	$6.131 \times 10^6$	m
Beam dimension(y)	0.05715	m
Beam dimension(z)	0.06033	m
Volume (Vol)	21,137	m <sup>3</sup>
Effective fluence	1,258,000	ions/cm <sup>2</sup>
Ions (N)	125,800	ion
Ions Density (n)	5.95	ions/m <sup>3</sup>

TABLE 5.8  
ION DENSITIES

Test Number	Effective Fluence (ions/cm <sup>2</sup> )	Ion Density (ions/m <sup>3</sup> )
Test #2	1,258,000	5.95
Test #7	1,409,000	6.67
Test #8	1,210,000	5.74

Using the ion densities shown in Table 5.8, the total ions that hit the radiation sensor during each test can be determined if the absorption area is known. The absorption area is calculated using the overlap area between the beam spot size (after the shield) and the radiation sensor strips. The ions that hit the absorption area for a particular channel will produce charge that is collected by the electrode for that channel. This absorption area is greatly influenced by the location of the beam spot on the radiation sensor channels. There are two end point cases for the location of the beam spot. The first case is if the beam is centered on the aluminum strip for one channel. This gives the maximum absorption area for this channel and small absorption area for the two adjacent channels. The second case is if the beam is centered on the gap between two aluminum strips. This gives a high absorption area for two adjacent channels and small absorption areas for the next two strips. Figure 5.18 and 5.19 show diagrams of these two cases for the large aperture shield. This shield produces a circular beam spot size with a diameter of 0.3175 cm. These figures are produced using a MATLAB script generated by another graduate student.

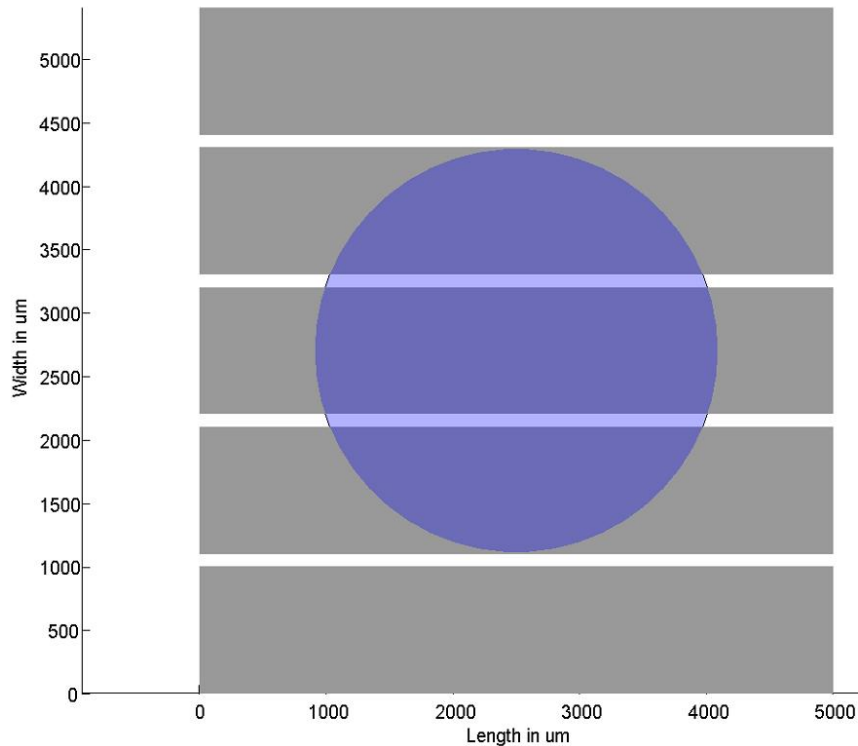


Figure 5.18 Diagram showing the large aperture beam spot centered on a front side aluminum strip. This situation will now be referred to as beam location #1.

This same MATLAB script is used to calculate the overlap area for these two cases. This range of area can then be used to calculate the number of ions that hit a given radiation sensor strip. The absorption area for a given strip is the overlap area between radiation beam spot and the aluminum strips plus half of the gap above and below the strip. This is based on the assumption that if charge is generated in between two strips, it will diffuse to whichever strip is closer and be collected. This divides the gaps in between two strips in half and adds this additional collection area to the corresponding strips.

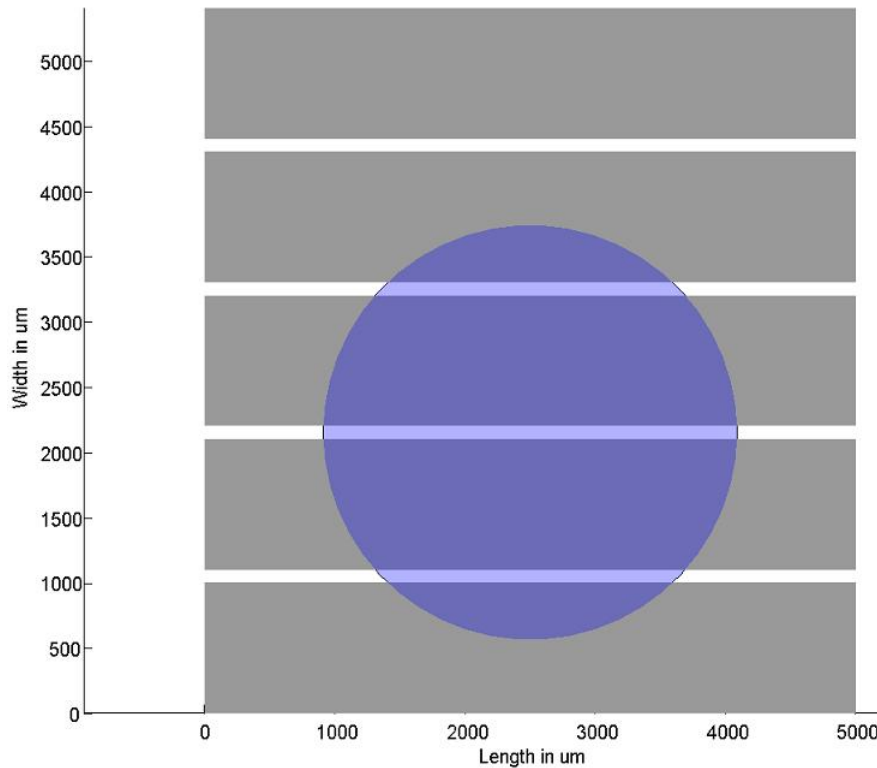


Figure 5.19 Diagram showing the large aperture beam spot centered on a gap between two front side aluminum strips. This situation will now be referred to as beam location #2.

The overlap area for the five strips shown in Figure 5.18 and 5.19 are computed. The results of these calculations are seen in Table 5.9. For this analysis, the strips in the two figures are number 1 – 5, with 1 being the very bottom strip and 5 being the strip located at the top. With this numbering scheme, the beam spot is centered on strip 3 in Figure 5.18 and in between strips 2 and 3 in Figure 5.19. Also included in this table, is the total overlap area for the entire beam spot size (the area of the spot size). These overlap absorption areas are the same for both the front and back side of the radiation sensor, since the same to scenarios for spot location exist for both the front and back of the sensor.

TABLE 5.9  
OVERLAP AREAS

Radiation Channel Number	Location #1 Overlap Areas (m <sup>2</sup> ) (Figure 5.18)	Location #2 Overlap Areas (m <sup>2</sup> ) (Figure 5.19)
1	0	0.7582 x 10 <sup>-6</sup>
2	2.2321 x 10 <sup>-6</sup>	3.1603 x 10 <sup>-6</sup>
3	3.3909 x 10 <sup>-6</sup>	3.1603 x 10 <sup>-6</sup>
4	2.2321 x 10 <sup>-6</sup>	0.7582 x 10 <sup>-6</sup>
5	0	0
Total Overlap	7.9145 x 10 <sup>-6</sup>	7.9145 x 10 <sup>-6</sup>

The absorption areas for the two different cases are now known for a section of five different strips shown in the figures. These overlaps can be extended to any of the tests completed using the large aperture shield, meaning that the data can be extrapolated so that the beam is centered on any strip or in between any two adjacent strips. The true overlap area for a particular test will be somewhere in between the two values shown in Table 5.9. The total ions that hit these areas are now determined. The data in Table 5.9 is used with the value found using (5.4) to find the volume of the beam. This volume is then used with the values found in Table 5.8 (ion densities) to determine the number of ions that hits each radiation sensor strip for the two beam positions. This ion count is first calculated for the front side strips in test #2 and can be seen in Table 5.10. The ion density for this test run is found in Table 5.8 and is 5.95 ions/m<sup>3</sup>. Multiplying the ion density by the newly found volume gives the total number of ions seen in the right two columns in Table 5.10. The channel numbers in the following tables correspond to the

channels on the front side of the radiation sensor. For this set of calculations, location #1 represents the beam centered on channel 8 and location #2 represents the beam centered on the gap between channels 7 and 8.

TABLE 5.10  
ION COUNTS FOR TEST #2

Channel Number	Location #1 Volume (m <sup>3</sup> )	Location #2 Volume (m <sup>3</sup> )	Location #1 Ions	Location #2 Ions
6	0	4.649	0	27.66
7	13.686	19.378	81.43	115.3
8	20.79	19.378	123.7	115.3
9	13.686	4.649	81.43	27.66
10	0	0	0	0
11	0	0	0	0
Total Overlap	48.55	48.55	288.87	288.87

The same calculations are performed to find the ion counts for test #7 and #8. These results are seen in Table 5.11 and Table 5.12. For the calculations in Table 5.11, location #1 represents the beam centered on channel 2 on the front side and location #2 is the beam centered on the gap in between channels 2 and 3 on the front side. For the calculations in Table 5.12, location #1 is when the beam is centered on channel 13 on the front side of the sensor and location #2 is when the beam is centered in between channels 13 and 14 on the front of the radiation sensor.

The ion density for test #7 is 6.67 ions/m<sup>3</sup>. The ion density for test #8 is 5.74 ions/m<sup>3</sup>. The data shown in Table 5.10, 5.11, and 5.12 holds true for both front side and back side pulses. The same fluences and overlap areas are used to model both the front

and back side of the sensor. This produces the same number of ions observed by the sensor for the front and back during a given test.

TABLE 5.11  
ION COUNTS FOR TEST #7

Strip Number	Location #1 Volume (m <sup>3</sup> )	Location #2 Volume (m <sup>3</sup> )	Location #1 Ions	Location #2 Ions
1	13.686	4.649	91.28	31
2	20.79	19.378	138.67	129.25
3	13.686	19.378	91.28	129.25
4	0	4.649	0	31
5	0	0	0	0
Total Overlap	48.55	48.55	323.83	323.83

TABLE 5.12  
ION COUNTS FOR TEST #8 (UPPER RIGHT CORNER OF SENSOR)

Strip Number	Location #1 Volume (m <sup>3</sup> )	Location #2 Volume (m <sup>3</sup> )	Location #1 Ions	Location #2 Ions
12	13.686	4.649	78.56	26.68
13	20.79	19.378	119.34	111.23
14	13.686	19.378	78.56	111.23
15	0	4.649	0	26.68
16	0	0	0	0
Total Overlap	48.55	48.55	278.68	278.68

Given the large distance over which the ions are spread (result of using (5.4)), it is assumed that each ion hits the radiation sensor individually. This will produce a long chain of strikes distributed over the given absorption areas. Using the previously

calculated output pulse widths (Table 5.6), the ion counts (Table 5.10), and the FPGA sampling rate, the number of counts is predicted. The output pulse widths found are for a single ion. By assuming that the ions all hit the sensor individually, the total output is this single pulse width multiplied by the number of ions that hit that location. This final output is then divided by the sampling rate to determine the total number of counts.

Equation (5.9) shows this calculation.

$$Counts = \frac{(\#ions) \times (pulse\_width)}{sampling\_rate} \quad (5.9)$$

Tables 5.13, 5.14, and 5.15 show the predicted counts for tests #7, #2, #8 that are determined using the previously found data and (5.9). These tables show the predictions for both the front and back sides of the sensor. For the data in Table 5.13, an output pulse width of 3.84  $\mu$ s is used for the front side (low gain channels) and an output pulse width of 8.85  $\mu$ s is used for the back side (high gain channels). For the data in Table 5.14, an output pulse width of 10.21  $\mu$ s is used for the front side (medium gain channels) and an output pulse width of 8.85  $\mu$ s is used for the back side (high gain channels). For the data in Table 5.15, an output pulse width of 30.96  $\mu$ s is used for the front side (high gain channels) and an output pulse width of 8.85  $\mu$ s is used for the back side (high gain channels).

TABLE 5.13  
COUNTS FOR TEST #7

Radiation Sensor Channel	Location #1 Ions	Location #2 Ion	Location #1 Predicted Counts	Location #2 Predicted Counts
F1	91.28	31	2900	985
F2	138.67	129.25	4406	4106
F3	91.28	129.25	2900	4106
F4	0	31	0	985
F5	0	0	0	0
Front Total	323.83	323.83	10289	10289
B16	0	31	0	2268
B15	91.28	129.25	6676	9453
B14	138.67	129.25	10142	9453
B13	91.28	31	6676	2267
B12	0	0	0	0
Back Total	323.83	323.83	23685	23685

TABLE 5.14  
COUNTS FOR TEST #2

Radiation Sensor Channel	Location #1 Ions	Location #2 Ion	Location #1 Predicted Counts	Location #2 Predicted Counts
F6	0	27.66	0	2334
F7	81.43	115.3	6872	9731
F8	123.7	115.3	10439	9731
F9	81.43	27.66	6872	2334
F10	0	0	0	0
F11	0	0	0	0
Front Total	288.87	288.87	24379	24379
B16	0	0	0	0
B15	0	27.66	0	2023
B14	81.43	115.3	5956	8433
B13	123.7	115.3	9047	8433
B12	81.43	27.66	5956	2023
Back Total	288.87	288.87	21128	21128

TABLE 5.15  
COUNTS FOR TEST #8

Radiation Sensor Channel	Location #1 Ions	Location #2 Ions	Location #1 Predicted Counts	Location #2 Predicted Counts
F12	78.56	26.68	20102	6827
F13	119.34	111.23	30537	28462
F14	78.56	111.23	20102	28462
F15	0	26.68	0	6827
F16	0	0	0	0
Front Total	278.68	278.68	71309	71309
B16	0	0	0	0
B15	0	26.68	0	1951
B14	78.56	111.23	5746	8135
B13	119.34	111.23	8729	8135
B12	78.56	26.68	5746	1951
Back Total	278.68	278.68	20383	20383

The counts for the three different tests have now been predicted. These predictions produce a range based on the location of the radiation beam with respect to the radiation sensor front and back electrodes. These predicted counts are now compared to the counts recorded during the radiation testing. Table 5.16 compares the predicted counts to the measured counts for each of the three different tests for the front side channels for the sensor. Table 5.17 compares the predicted counts to the measured counts for the back side channels of the radiation sensor. Following these tables are plots that show the predicted range and measured counts graphically. In these plots, the gray areas represent the predicted range and the black lines represent the measured value for the number of counts per second. Figure 5.20 shows the front side of the sensor during test #7. Figure 5.21 shows the front side of the sensor during test #2. Figure 5.22 shows

the front side of the sensor during test #8. Figure 5.23 shows the back side of the sensor during test #7. Figure 5.24 shows the back side of the sensor during test #2. Figure 5.25 shows the back side of the sensor during test #8.

TABLE 5.16  
FRONT SIDE PREDICTED VERSUS MEASURED COUNTS

Radiation Sensor Channel	Predicted Count Range	Measured Counts
Test #7		
F1	985 – 2900	1283
F2	4106 – 4406	3730
F3	2900 – 4106	3438
F4	0 – 985	704
F5	0	0
Total	10289	9155
Test #2		
F6	0 – 2334	2100
F7	6872 – 9731	6828
F8	9731 – 10439	8816
F9	2334 – 6872	5622
F10	0	1559
F11	0	547
Total	24379	25472
Test #8		
F12	6827 – 20102	14152
F13	28402 – 30537	18510
F14	20102 – 28762	18213
F15	0 – 6827	13141
F16	0	9657
Total	71309	73673

TABLE 5.17  
BACK SIDE PREDICTED VERSUS MEASURED COUNTS

Radiation Sensor Channel	Predicted Count Range	Measured Counts
Test #7		
B16	0	9
B15	0 – 2268	5
B14	6676 – 9453	11248
B13	9453 – 10142	9736
B12	2268 – 6676	11
Total	23685	21009
Test #2		
B16	0	0
B15	0 – 2023	20
B14	5956 – 8433	11529
B13	8433 – 9047	10873
B12	2023 – 5956	9
Total	21128	22431
Test #8		
B16	0	3
B15	0 – 1951	21
B14	5746 – 8135	10120
B13	8135 – 8729	10137
B12	1951 – 5746	1
Total	20383	20282

These plots show that the developed model is reasonably accurate at predicting the number of counts observed. A few of the predictions are very close to the measured values. Even the predictions that are not exact are a fairly close estimate of the measured number of counts. This model is unable to predict the intersections due to there not being a way to determine when (in time) the counts on the front and back the sensor occurred. Without knowing if the front and back output pulses overlapped (strikes occurred at the

same time) or were spaced by some time segment, it is impossible to produce an intersection count for the radiation sensor. The prediction of the counts on the individual front and back side channels is sufficient when modeling the performance of the radiation sensor for a particular radiation ion strike.

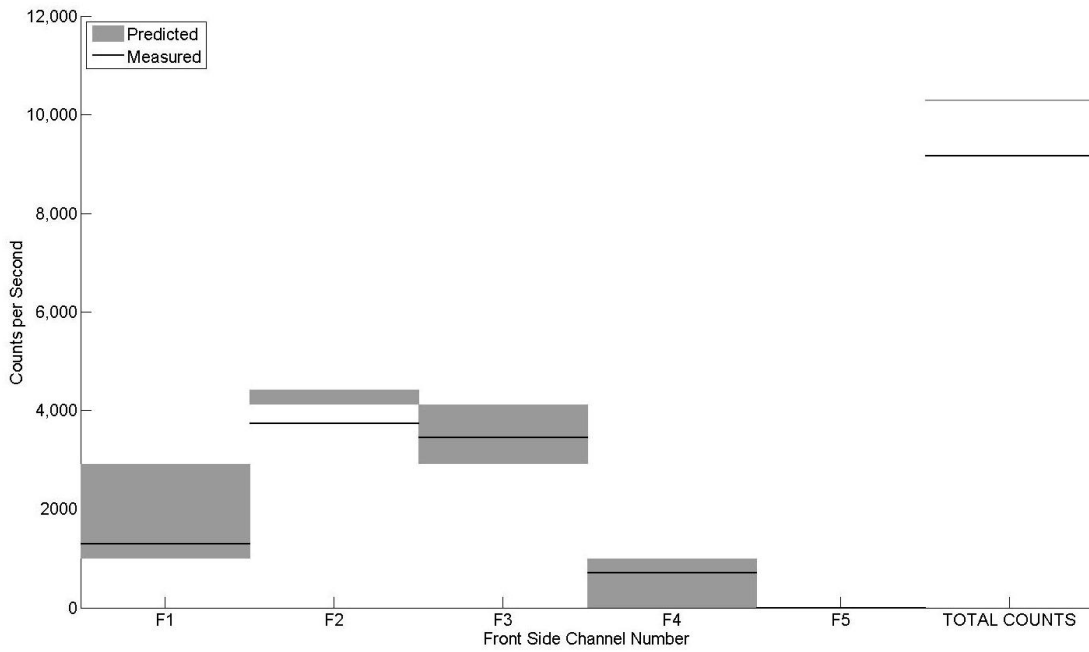


Figure 5.20 Plots showing the front side measured and predicted counts for test #7.

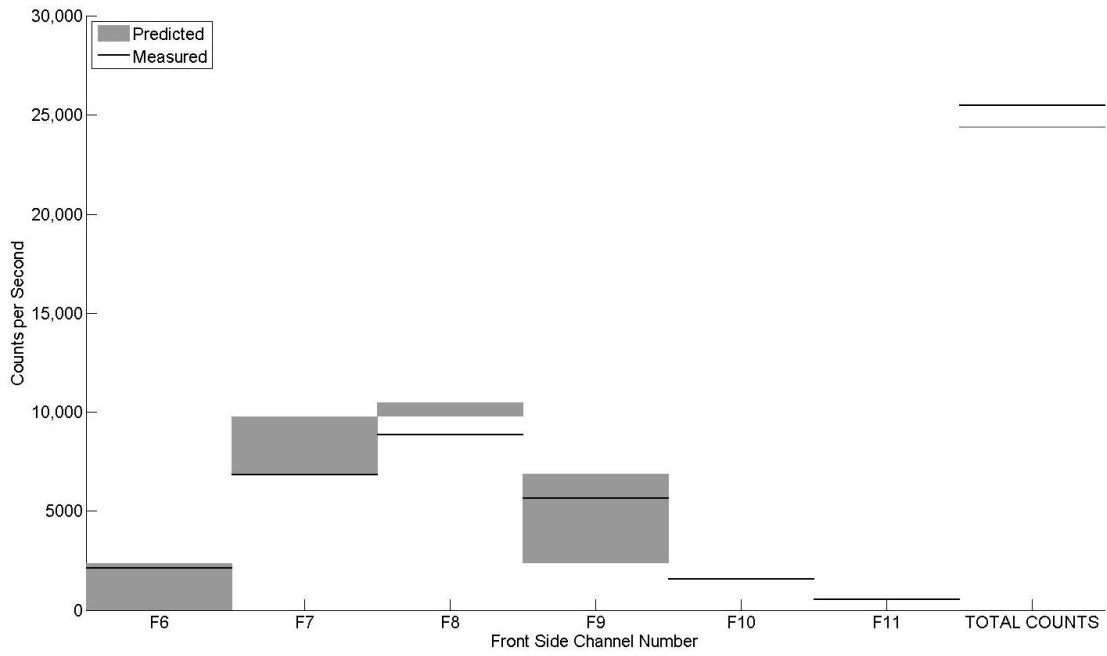


Figure 5.21 Plot showing the front side measured and predicted counts for test #2.

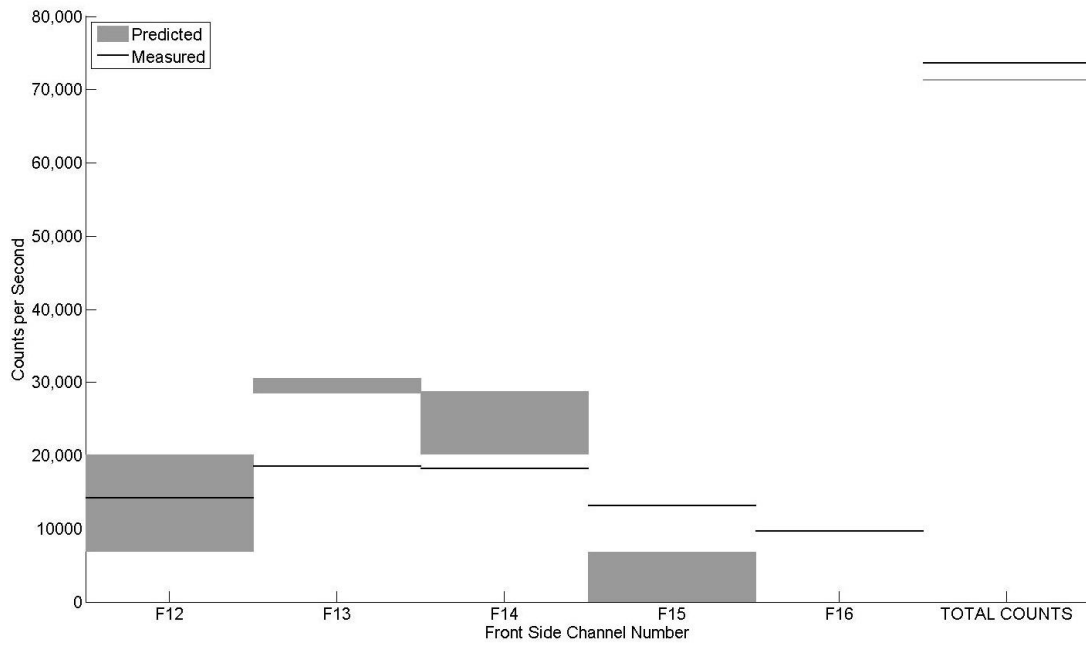


Figure 5.22 Plots showing the front side measured and predicted counts for test #8.

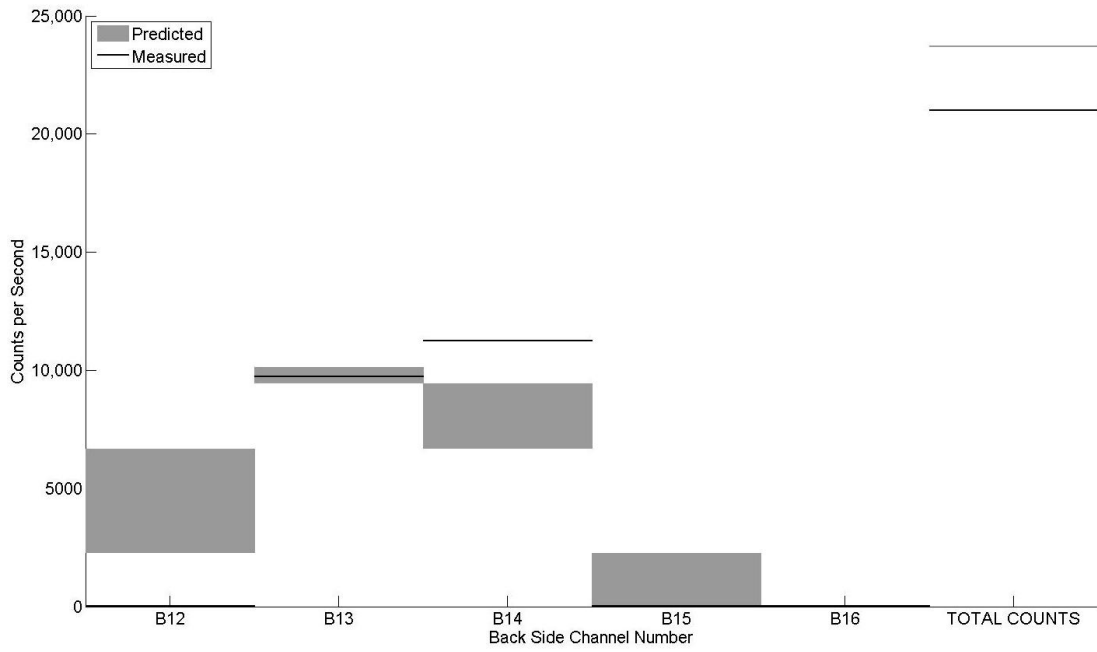


Figure 5.23 Plot showing the back side measured and predicted counts for test #7.

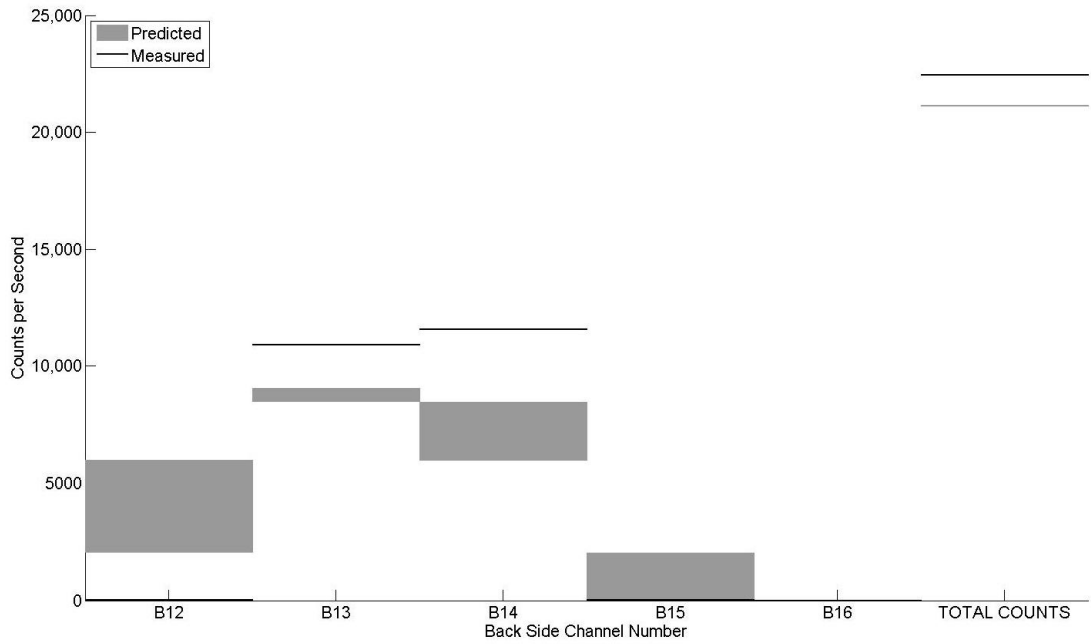


Figure 5.24 Plot showing the back side measured and predicted counts for test #2.

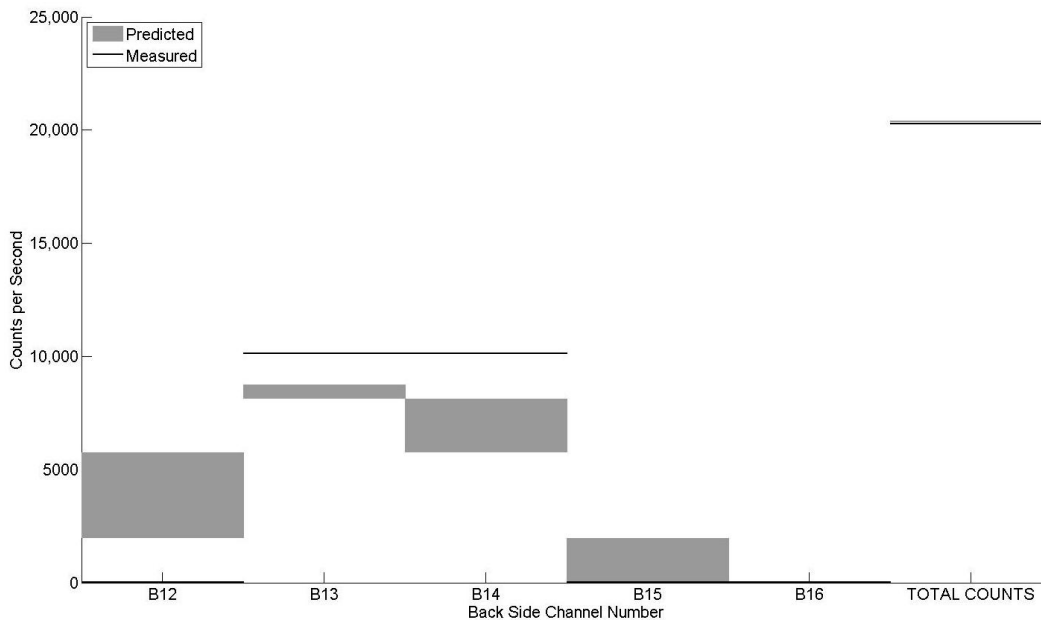


Figure 5.25 Plot showing the back side measured and predicted counts for test #8.

Overall, the developed model appears to be a close representation of the actual number of counts. The total number of counts measured and predicted for all of these tests is the most accurate prediction made by the model. The total predicted counts are always within 10% of the actual total counts measured during the testing. The prediction of the front side counts on the lower and medium gain channels is also quite accurate. The plots in Figure 5.20 and Figure 5.21 reflect this accuracy, since the measured data usually falls within the range produced by the model. The model does not predict the back side counts quite as accurately, but is still a close representation of this back side data.

To further verify the model, one of the radiation tests that used the small aperture shield (40 mils) is now analyzed using the exact same approach as before. The test run selected for this analysis is test # 19. Figure 26 shows the measured results for this

particular test. Table 5.18 shows the counts observed on the different sensor channels for this test.

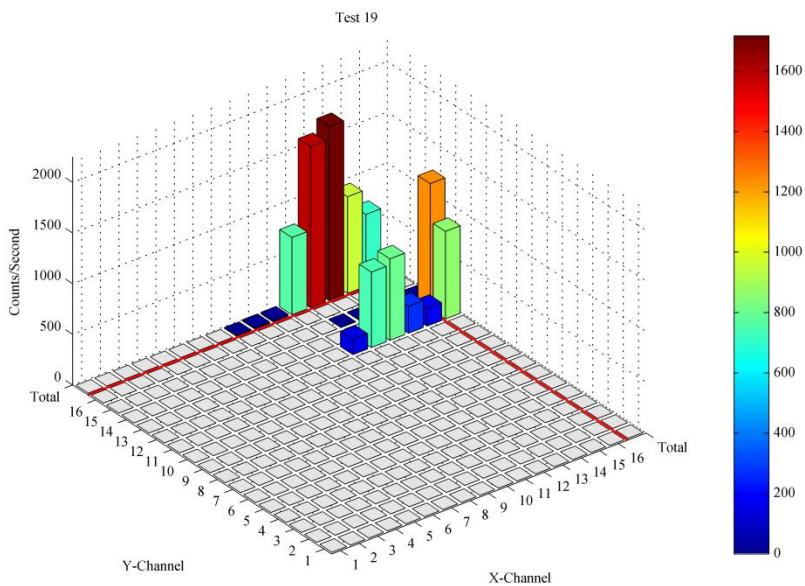


Figure 5.26 Radiation test data for test run #19.

For this smaller hole, the two potential locations of the beam spot are shown in Figure 5.27.

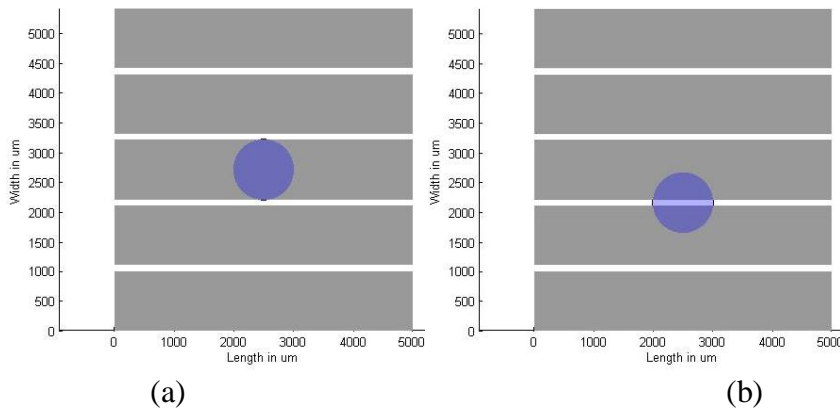


Figure 5.27 Diagrams showing the two potential locations of the small aperture beam spot (a) centered on a channel (b) centered on the gap between two adjacent channels.

TABLE 5.18  
AVERAGE COUNTS PER SECOND FOR TEST #19

Sensor Channels	Average Counts per Second
Front Channels	
F12	763
F13	1590
F14	1717
F15	954
F16	709
Total for Front	5733
Back Channels	
B16	0
B15	3
B14	1237
B13	864
B12	0
Total for Back	2086

The beam is either centered entirely on one channel or, on the gap in between two channels. The exact same analysis used for the previous three tests is followed for this test. The total number of ions that hit the sensor for these two different beam spot locations are determined. Once again, the ions are treated as individual events, with each ion hitting the sensor one at a time. For this testing location, the beam is aimed at the high gain channels for both the front and back of the sensor. This means that the output pulse widths used for the prediction of the number of counts are  $30.96 \mu\text{s}$  for the front side of the sensor and  $8.85 \mu\text{s}$  for the back side of the sensor. These pulse widths are scaled by the total number of ions and divided by the sampling rate to produce the predicted counts range. Table 5.19 shows the predicted counts per second for each

channel as well as the measured counts. Figure 5.28 shows this same data for the front side of the sensor with the gray bars representing the predicted range and the black lines representing the measured counts. Figure 5.29 shows this same data for the back side of the sensor.

The counts predicted for this smaller beam spot size (40 mil aperture) are not as accurate as the counts predicted for the large aperture. Some of the ranges are still close, but performance of the sensor with this smaller beam spot size seems to be dominated by diffusion which is not included in the developed model. This potential error is discussed following the plots.

TABLE 5.19  
PREDICTED VERSUS MEASURED COUNTS FOR TEST #19

Radiation Sensor Channel	Predicted Count Range	Measured Counts
Front		
F12	0	763
F13	0 – 1035	1590
F14	1035 – 2097	1717
F15	0	954
F16	0	709
Total	2967	5733
Back		
B16	0	0
B15	0	3
B14	296 – 600	1237
B13	0 – 296	864
B12	0	0
Total	600	2086

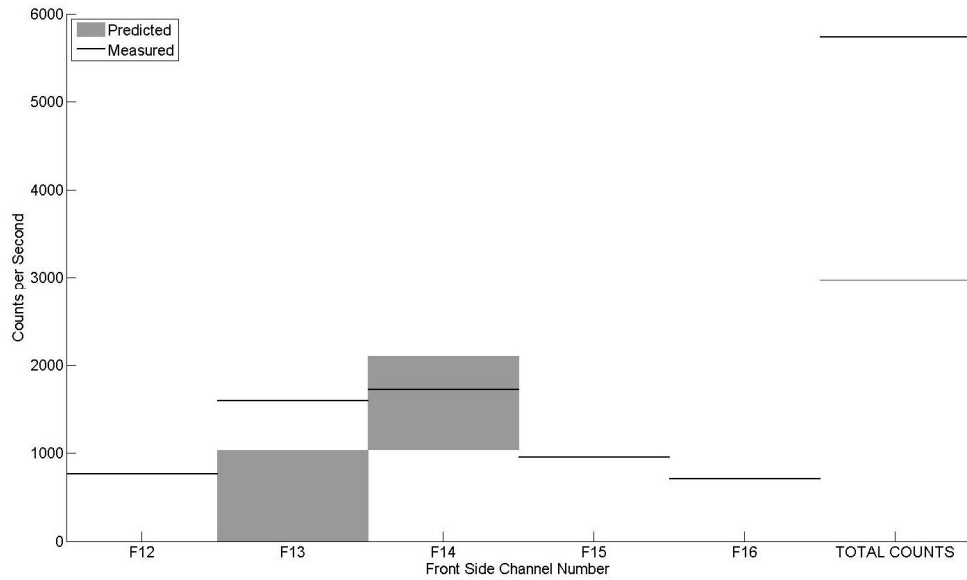


Figure 5.28 Plot showing the front side predicted versus measured counts for test #19.

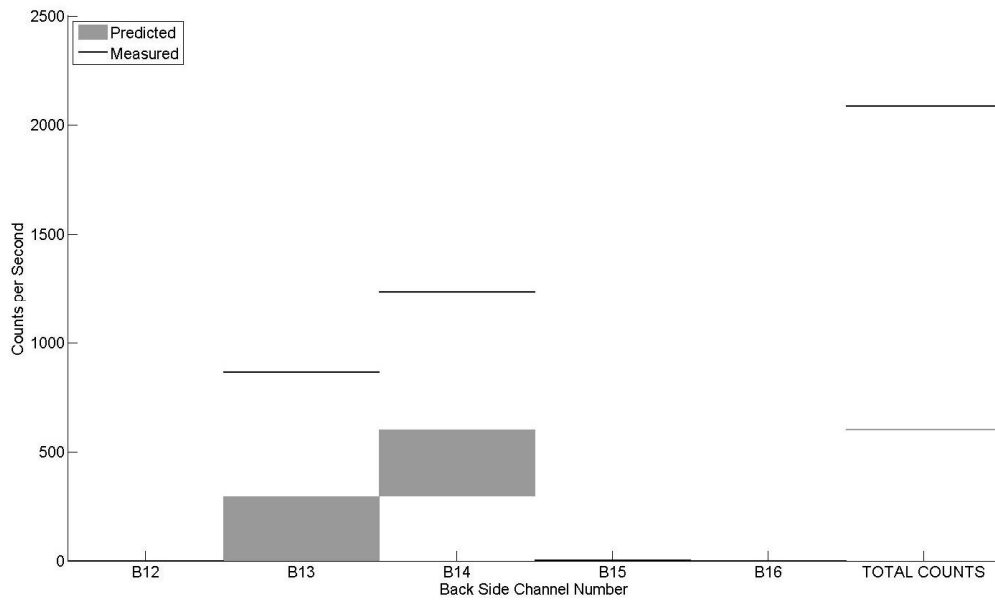


Figure 5.29 Plot showing the back side predicted versus measured counts for test #19.

There are many different reasons that can attribute to this model not predicting the measured number of counts. The first potential area for errors in the predictions comes from some assumptions made about the operation of the radiation sensor. The prediction

model ignores recombination, diffusion, and assumes that only charge produced in the depletion region is collected. After a radiation strike, some of the charge produced will be lost to recombination. This reduces the output signals achieved for a given strike. The amount of charge lost is impossible to determine and this is the reason that this loss mechanism is ignored in the prediction model. Recombination has the potential to reduce the number of counts observed on any of the channels. Adding in a loss factor like this would cause the predictions that over estimated the number of counts to end up being closer to the measured number of counts.

Like recombination, diffusion is definitely occurring inside of the radiation sensor substrate. As previously described, charge created outside of the depletion regions is free to diffuse throughout the sensor. The amount of charge that diffuses in any direction is unknown but is going to be a product of the amount of charge produced. Two directions of diffusion that occur inside of the sensor have the potential to produce errors in the predicted counts. These two diffusion directions are vertically and laterally.

Lateral diffusion is the reason that some of the channels that have 0 predicted counts do not have 0 measured counts. The charge produced elsewhere in the sensor was able to diffuse to these channels and be amplified into a measurable output signal. The model produces counts only on the directly hit channels and does not produce any counts for adjacent channels due to diffusion. Without a method to determine the amount of charge that diffuses laterally, this metric is difficult to incorporate into the model and will therefore always produce some error in the predicted counts.

Vertical diffusion is the reason that the counts measured on the back side exceed the counts predicted by the model. For the model, the back side channels are produced only by the charge collection in the back side depletion region. Since the ions do not pass completely through the sensor, there is going to be some amount of vertical diffusion. This means that charge produced outside of the back side depletion regions will diffuse into these regions and be collected. As with the lateral diffusion, the amount of charge that undergoes this vertical diffusion is unknown. Ignoring this extra charge collected on the back side is the reason that the model predicts lower counts than the number actually observed on the individual channels. The model does, however, predict the total counts across all back side channels very accurately.

There are also a couple sources of error that come from the treatment of the ion beam in the model. First, the average fluence is used to determine the number of ions that hit the radiation sensor. This average is probably a good representation of the fluence, but at any given sample during the testing this value could be higher or lower. A change in this fluence alters the number of ions that hit the radiation sensor. The second source of error in the beam line calculations comes from the assumption of perfect alignment. Perfect alignment is achieved when the beam line is exactly perpendicular to the front surface of the radiation sensor. The setup was carefully assembled in order to get it as close to perpendicular as possible, but there is definitely a small amount of loss incorporated here due to misalignment. Any combination of these errors can combine to produce a prediction that does not match the measured counts.

Despite these errors, the model does predict the number of counts reasonable accurately. The model displays the best performance when predicting the total number of counts seen in a testing region for both the front and back sides of the sensor. These predictions are all close to the measured values for the total counts in a testing region.

CHAPTER SIX – CONCLUSION AND REDCOMMENDATION  
FOR FUTURE WORK

Conclusion

The goal of this design was to develop a radiation sensor capable of spatially detecting a strike from a high energy source. The sensor produces two outputs that can be used as coordinates for the radiation strike. These coordinates are then fed into a computer system that avoids the radiation strike location and repairs any circuits in this area. In this way, a fault tolerant system can be developed that can spatially sense any incoming strikes that can cause potential damage to the system.

The end design proved to be effective at determining the location of a high energy radiation strike. The sensor was capable of detecting radiation particles with an energy that could cause damage in a digital system. The sensor was able to output top and bottom signals produced by the ionization of the silicon substrate. These output signals were then input into an electronics chain. The electronics chain proved effective at amplifying and shaping the signals from the sensor into a signal usable by an FPGA computer system. Finally, the designed high speed event detector was able to sample the output of the electronics and establish radiation strike counts for all of the sensor channels. The performance of this system was verified by the testing performed at the Texas A&M University Cyclotron facility. A radiation source was chosen, and the event detector was able to log radiation strikes on various channels as the beam was aimed at

different locations. This data shows the ability to produce the coordinates of the radiation strike.

The final part of the design was the development of a prediction model that could be used to estimate the number of counts expected for a given radiation strike. The model developed proved to be reasonably accurate at predicting the number of counts per channel. The differences were never great enough to completely discredit the model.

Overall, the system operated as anticipated and was able to effectively relay the location of a radiation strike to an FPGA based system.

#### Recommendations for Future Work

There are many areas for additional work in this project. The first of these is more radiation testing at the Cyclotron facility. A great deal of data was collected the first time, but many more experiments exist that can provide vital information about the performance of the sensor system. One of these experiments includes biasing the sensor to determine the performance of a fully depleted sensor. This is one potential solution to the issue of lateral diffuse and recombination. Testing the sensor with the same parameters as before but with an external bias applied can answer many questions.

Another additional experiment to perform is to produce an amplifier board that has the ideal gains for both the front and back side channels. The beam could then be scanned across the sensor while monitoring the outputs of all of the channels. This allows for the characterization of all of the sensor channels instead of just a small

quadrant at a time. This requires the production of a new shield to allow for translation during the test.

One last recommendation for future work involves testing the radiation sensor system in a “real” environment such as a high altitude balloon or a sounding rocket. These two vehicles would allow the sensor to be exposed to high energy particles in the Earth’s upper atmosphere. This would provide insight into the performance of the sensor in the environment for which it was developed.

REFERENCES CITED

- [1] A. Holmes-Siedle, L. Adams. Handbook of Radiation Effects. 2<sup>nd</sup> edition. New York, Oxford University Press, 2002.
- [2] C. Claeys, E. Simoen. Radiation Effects in Advanced Semiconductor Materials and Devices. Berlin Heidelberg, ISBN 3-54043393-7, Springer-Verlag, 2002.
- [3] R. Ladbury. "Radiation Hardening at the System Level." Section IV. *IEEE NSREC Short Course*, 2007.
- [4] "Single Event Upset (SEU)." *Single Event Effects Testing, aerospace.ogr*. 23 March 2012. <<http://www.aeor.org/capabilities/seet/SEupsets.html>>.
- [5] T. Buerkle, B. LaMeres, T. Kaiser, E. Gowens, L. Smoot, T. Heetderks, K. Schipf, L. Clem, S. Schielke, R. Luhr. "Ionizing Radiation Detector for Environmental Awareness in FPGA-Based Flight Computers." *IEEE Sensor*. Unpublished.
- [6] I. R. Williams. "Silicon radiation detectors and some simple applications." *Physics Education*, Vol. 2, 94 – 99.
- [7] C. Da Via, G. Anelli, J. Hasi, P. Jarron, C. Kenney, A. Kok, Sherwood Parker, E. Perozziello, S.J. Watters. "Advances in silicon detectors for particle tracking in extreme radiation environments." *Nuclear Instruments and Methods in Physics Research A*, Vol. 509 (2003), 86 – 91.
- [8] P. Weilhammer. "The Role of Silicon Radiation Sensors and Integrated Front-End Electronics in Medical Imaging Instrumentation." *Advanced Instrumentation Seminars*, 2 May 2007. <[www-group.slac.stanford.edu/ais/publicDocs/presentation67.pdf](http://www-group.slac.stanford.edu/ais/publicDocs/presentation67.pdf)>.
- [9] E. Gowens. "Two Dimensional Radiation Sensor Development for use in Space Bound Reconfigurable Computers." May 2011.
- [10] U.C. Bergmann, H.O.U. Fynbo, O. Tengblad. "Use of Si strip detectors for low-energy particles in compact geometry." *Nuclear Instruments and Methods in Physics Research A*, Vol. 515 (2003), 657 – 664.
- [11] G. Lutz. Semiconductor Radiation Detectors: Device Physics. Springer, 1999.
- [12] L. Rossi, P. Fischer, T. Rohe, N. Wermes. Pixel Detectors: From Fundamentals to Applications. *Particle Acceleration and Detection*. Springer, 2006.
- [13] J. Kemmer, G. Lutz. "New Structures for Position Sensitive Semiconductor Detectors." *Nuclear Instruments and Methods in Physics Research A*, Vol. 273 (1988), 588 – 598,

- [14] S. Seidel. "A Review of Design Considerations for the Sensor Matrix in Semiconductor Pixel Detectors for Tracking in Particle Physics Experiments." *Nuclear Instruments and Methods in Physics Research A*, Vol. 465 (2001), 267 – 296.
- [15] M. Turala. "Silicon Tracking Detectors – Historical Overview." *Nuclear Instruments and Methods in Physics Research A*, Vol. 541 (2005), 1 – 14.
- [16] H. Dijkstra. "Overview of silicon detectors." *Nuclear Instruments and Methods in Physics Research A*, Vol. 478 (2002), 37 – 45.
- [17] M. Xapsos. "A Spatially Restricted Linear Energy Transfer Equation." *Radiation Research*, Vol. 132 (1992), 282 – 287.
- [18] W. Dunn, R. Hugtenburg. "The Interaction of Radiation with Matter: Charged Particle and Electron Interactions." *IEEE Short Course*, 29 Oct.2006.
- [19] "Characteristics and use of Charge amplifier." *Hamamatsu*. Technical Information SD-37, Solid State Division. Oct. 2001.
- [20] "Radiation Effects Facility." *The Cyclotron Institute, Texas A&M University*, <[cyclotron.tamu.edu/ref/index.php](http://cyclotron.tamu.edu/ref/index.php)>.
- [21] S.O. Kasap. Principles of Electronic Materials and Devices. Third edition. New York, McGraw-Hill, 2006.
- [22] S. Dimitrijević. Principles of Semiconductor Devices. New York, Oxford University Press, 2006.
- [23] D. Neaman. Semiconductor Physics and Devices: Basic Principles. Third edition. New York, McGraw-Hill, 2003.

APPENDICES

APPENDIX A

RADITION SENSOR FABRICATION PROCESS

1. Oxidation (Masking Layer for P+ Channels)
  - a. Temperature 1000 °C
  - b. Time 90 minutes
  - c. Type Wet
  - d. Nitrogen Gas Flow 7
  - e. Oxygen Gas Flow 9
2. Photolithography for Front Side P+ Channels
  - a. Photoresist Used S1813
  - b. Sides Coated Both front and back
  - c. Spin Program #9 (5250 rpm for 30 seconds)
  - d. Bake Program #9 (115 °C for 60 seconds)
  - e. Mask Used #1
  - f. Alignment Marks Front
  - g. Patterned Side Front
  - h. Exposure Time 4.5 seconds
  - i. Developer AZ-726 MIF
  - j. Developing Time 60 seconds
  - k. Bake Program #9 (115 °C for 60 seconds)
3. Oxide Etch
  - a. Etchant BOE 6:1
  - b. Etch Rate 900 Å/minutes
  - c. Etch Time ~6 minutes
4. Solvent Clean
  - a. Rinse with Acetone
  - b. Rinse with Isopropanol
  - c. Rinse with Methanol
  - d. Rinse with DI water and dry with Nitrogen
5. RCA Clean
  - a. Piranha Etch (3:1 H<sub>2</sub>O<sub>2</sub>:H<sub>2</sub>SO<sub>4</sub>)
  - b. Temperature Room temperature
  - c. Time 10 minutes
  - d. DI Water Rinse 2 minutes
  - e. BOE 6:1
  - f. Temperature Room temperature
  - g. Time 15 seconds
  - h. DI Water Rinse 2 minutes
  - i. Ionic clean (6:1:1 H<sub>2</sub>O:H<sub>2</sub>O<sub>2</sub>:HCl)
  - j. Temperature 40 °C
  - k. Time 10 minutes
  - l. DI Water Rinse 5 minutes
  - m. Dry with Nitrogen

6. Front Side P+ Diffusion
  - a. Furnace Boron
  - b. Sources Boron – 2 wafers per source
  - c. Doping Side Front
  - d. Temperature 950 °C
  - e. Time 60 minutes
  - f. Nitrogen Gas Flow 7
7. BSG Etch
  - a. Etchant BOE 6:1
  - b. Time ~15 minutes (use visual inspection)
  - c. DI Water Rinse 5 minutes
8. Oxidation (Masking Layer for N+ Channels)
  - a. Temperature 1000 °C
  - b. Time 90 minutes
  - c. Type Wet
  - d. Nitrogen Gas Flow 7
  - e. Oxygen Gas Flow 9
9. Aluminum Deposition
  - a. Deposition Surface Front
  - b. Desired Thickness ~500 nm
  - c. Al Sample Size ~40 cm<sup>2</sup> for 4 wafers
10. Photolithography for Back Side Alignment
  - a. Photoresist Used S1813
  - b. Sides Coated Front
  - c. Spin Program #9 (5250 rpm for 30 seconds)
  - d. Bake Program #9 (115 °C for 60 seconds)
  - e. Mask Used #1
  - f. Alignment Marks Front
  - g. Patterned Side Front
  - h. Exposure Time 4.5 seconds
  - i. Developer AZ-726 MIF
  - j. Developing Time 60 seconds
  - k. Bake Program #9 (115 °C for 60 seconds)
11. Aluminum Etch
  - a. Etchant Aluminum Etch
  - b. Temperature 70 °C
  - c. Time ~2 minutes (use visual inspection)
  - d. DI Water Rinse By hand
12. Solvent Clean
  - a. Rinse with Acetone
  - b. Rinse with Isopropanol
  - c. Rinse with Methanol
  - d. Rinse with DI water and dry with Nitrogen

13. Photolithography for Back Side N+ Channels
  - a. Photoresist Used S1813
  - b. Sides Coated Both front and back
  - c. Spin Program #9 (5250 rpm for 30 seconds)
  - d. Bake Program #9 (115 °C for 60 seconds)
  - e. Mask Used #2
  - f. Alignment Marks Front (IR cameras used)
  - g. Patterned Side Back
  - h. Exposure Time 4.5 seconds
  - i. Developer AZ-726 MIF
  - j. Developing Time 60 seconds
  - k. Bake Program #9 (115 °C for 60 seconds)
14. Oxide Etch
  - a. Etchant BOE 6:1
  - b. Etch Rate 900 Å/minutes
  - c. Etch Time ~6 minutes
15. Solvent Clean
  - a. Rinse with Acetone
  - b. Rinse with Isopropanol
  - c. Rinse with Methanol
  - d. Rinse with DI water and dry with Nitrogen
16. Aluminum Etch
  - a. Etchant Aluminum Etch
  - b. Temperature 70 °C
  - c. Time ~2 minutes (use visual inspection)
  - d. DI Water Rinse By hand
17. RCA Clean
  - a. Piranha Etch (3:1 H<sub>2</sub>O<sub>2</sub>:H<sub>2</sub>SO<sub>4</sub>)
  - b. Temperature Room temperature
  - c. Time 10 minutes
  - d. DI Water Rinse 2 minutes
  - e. BOE 6:1
  - f. Temperature Room temperature
  - g. Time 15 seconds
  - h. DI Water Rinse 2 minutes
  - i. Ionic clean (6:1:1 H<sub>2</sub>O:H<sub>2</sub>O<sub>2</sub>:HCl)
  - j. Temperature 40 °C
  - k. Time 10 minutes
  - l. DI Water Rinse 5 minutes
  - m. Dry with Nitrogen

18. Back Side N+ Diffusion
  - a. Furnace Phosphorous
  - b. Sources Phosphorous – 2 wafers per source
  - c. Doping Side Back
  - d. Temperature 950 °C
  - e. Time 30 minutes
  - f. Nitrogen Gas Flow 7
19. PSG Etch
  - a. Etchant BOE 6:1
  - b. Time ~15 minutes (use visual inspection)
  - c. DI Water Rinse 5 minutes
20. Oxidation (Masking Layer for P+ Barriers)
  - a. Temperature 1000 °C
  - b. Time 90 minutes
  - c. Type Wet
  - d. Nitrogen Gas Flow 7
  - e. Oxygen Gas Flow 9
21. Photolithography for Back Side P+ Barriers
  - a. Photoresist Used S1813
  - b. Sides Coated Both front and back
  - c. Spin Program #9 (5250 rpm for 30 seconds)
  - d. Bake Program #9 (115 °C for 60 seconds)
  - e. Mask Used #3
  - f. Alignment Marks Back
  - g. Patterned Side Back
  - h. Exposure Time 4.5 seconds
  - i. Developer AZ-726 MIF
  - j. Developing Time 60 seconds
  - k. Bake Program #9 (115 °C for 60 seconds)
22. Oxide Etch
  - a. Etchant BOE 6:1
  - b. Etch Rate 900 Å/minutes
  - c. Etch Time ~6 minutes
23. Solvent Clean
  - a. Rinse with Acetone
  - b. Rinse with Isopropanol
  - c. Rinse with Methanol
  - d. Rinse with DI water and dry with Nitrogen

24. RCA Clean
- Piranha Etch (3:1 H<sub>2</sub>O<sub>2</sub>:H<sub>2</sub>SO<sub>4</sub>)
  - Temperature Room temperature
  - Time 10 minutes
  - DI Water Rinse 2 minutes
  - BOE 6:1
  - Temperature Room temperature
  - Time 15 seconds
  - DI Water Rinse 2 minutes
  - Ionic clean (6:1:1 H<sub>2</sub>O:H<sub>2</sub>O<sub>2</sub>:HCl)
  - Temperature 40 °C
  - Time 10 minutes
  - DI Water Rinse 5 minutes
  - Dry with Nitrogen
25. Back Side P+ Barrier Diffusion
- Furnace Boron
  - Sources Boron – 2 wafers per source
  - Side Facing Sources Back
  - Temperature 950 °C
  - Time 30 minutes
  - Nitrogen Flow 7
26. BSG Etch
- Etchant BOE 6:1
  - Time ~15 minutes (use visual inspection)
  - DI Water Rinse 5 minutes
27. Oxidation (Masking Layer for N+ Barriers)
- Temperature 1000 °C
  - Time 90 minutes
  - Type Wet
  - Nitrogen Gas Flow 7
  - Oxygen Gas Flow 9
28. Photolithography for Front Side N+ Barriers
- Photoresist Used S1813
  - Sides Coated Both front and back
  - Spin Program #9 (5250 rpm for 30 seconds)
  - Bake Program #9 (115 °C for 60 seconds)
  - Mask Used #8
  - Alignment Marks Front
  - Patterned Side Front
  - Exposure Time 4.5 seconds
  - Developer AZ-726 MIF
  - Developing Time 60 seconds
  - Bake Program #9 (115 °C for 60 seconds)

29. Oxide Etch
- a. Etchant BOE 6:1
  - b. Etch Rate 900 Å/minutes
  - c. Etch Time ~6 minutes
20. Solvent Clean
- a. Rinse with Acetone
  - b. Rinse with Isopropanol
  - c. Rinse with Methanol
  - d. Rinse with DI water and dry with Nitrogen
31. RCA Clean
- a. Piranha Etch (3:1 H<sub>2</sub>O<sub>2</sub>:H<sub>2</sub>SO<sub>4</sub>)
  - b. Temperature Room temperature
  - c. Time 10 minutes
  - d. DI Water Rinse 2 minutes
  - e. BOE 6:1
  - f. Temperature Room temperature
  - g. Time 15 seconds
  - h. DI Water Rinse 2 minutes
  - i. Ionic clean (6:1:1 H<sub>2</sub>O:H<sub>2</sub>O<sub>2</sub>:HCl)
  - j. Temperature 40 °C
  - k. Time 10 minutes
  - l. DI Water Rinse 5 minutes
  - m. Dry with Nitrogen
32. Front Side N+ Barrier Diffusion
- a. Furnace Phosphorous
  - b. Sources Phosphorous – 2 wafers per source
  - c. Side Facing Sources Front
  - d. Temperature 950 °C
  - e. Time 30 minutes
  - f. Nitrogen Flow 7
33. PSG Etch
- a. Etchant BOE 6:1
  - b. Time ~15 minutes (use visual inspection)
  - c. DI Water Rinse 5 minutes
34. Oxidation (Contacts)
- a. Temperature 1000 °C
  - b. Time 60 minutes
  - c. Type Dry
  - d. Nitrogen Gas Flow 7
  - e. Oxygen Gas Flow 9

35. Photolithography for Front Side Contacts
- a. Photoresist Used S1813
  - b. Sides Coated Both front and back
  - c. Spin Program #9 (5250 rpm for 30 seconds)
  - d. Bake Program #9 (115 °C for 60 seconds)
  - e. Mask Used #4
  - f. Alignment Marks Front
  - g. Patterned Side Front
  - h. Exposure Time 4.5 seconds
36. Photolithography for Back Side Contacts
- a. Mask Used #5
  - b. Alignment Marks Back
  - c. Patterned Side Back
  - d. Exposure Time 4.5 seconds
  - e. Developer AZ-726 MIF
  - f. Developing Time 60 seconds
  - g. Bake Program #9 (115 °C for 60 seconds)
    - i. Do Steps 35 and 36 at the same time
37. Oxide Etch
- a. Etchant BOE 6:1
  - b. Etch Rate 900 Å/minutes
  - c. Etch Time ~6 minutes
38. Solvent Clean
- a. Rinse with Acetone
  - b. Rinse with Isopropanol
  - c. Rinse with Methanol
  - d. Rinse with DI water and dry with Nitrogen
39. Aluminum Deposition
- a. Deposition Surface Front
  - b. Desired Thickness ~500 nm
  - c. Al Sample Size ~40 cm<sup>2</sup> for 4 wafers
40. Aluminum Deposition
- a. Deposition Surface Back
  - b. Desired Thickness ~500 nm
  - c. Al Sample Size ~40 cm<sup>2</sup> for 4 wafers
41. Photolithography for Front Side Metal
- a. Photoresist Used S1813
  - b. Sides Coated Both front and back
  - c. Spin Program #9 (5250 rpm for 30 seconds)
  - d. Bake Program #9 (115 °C for 60 seconds)
  - e. Mask Used #6
  - f. Alignment Marks Front
  - g. Patterned Side Front
  - h. Exposure Time 4.5 seconds

42. Photolithography for Back Side Metal
- a. Mask Used #7
  - b. Alignment Marks Back
  - c. Patterned Side Back
  - d. Exposure Time 4.5 seconds
  - e. Developer AZ-726 MIF
  - f. Developing Time 60 seconds
  - g. Bake Program #9 (115 °C for 60 seconds)
    - i. Do Steps 41 and 42 at the same time
43. Aluminum Etch
- a. Etchant Aluminum Etch
  - b. Temperature 70 °C
  - c. Time ~2 minutes (use visual inspection)
  - d. DI Water Rinse By hand
44. Solvent Clean
- a. Rinse with Acetone
  - b. Rinse with Isopropanol
  - c. Rinse with Methanol
  - d. Rinse with DI water and dry with Nitrogen
45. Anneal
- a. Furnace Boron
  - b. Sources NONE
  - c. Temperature 400 °C
  - d. Time 30 minutes
  - e. Nitrogen Gas Flow 7

APPENDIX B

CYCLOTRON TESTING BEAM PARAMETERS

## Available Beams

	Ion	Mass (amu)	A MeV	Total Energy (MeV)	Energy at Bragg Peak (MeV)	Range in Si ( $\mu\text{m}$ )	Range at Bragg ( $\mu\text{m}$ )	Range to Bragg Peak ( $\mu\text{m}$ )	Initial LET (vacuum)	Initial LET (air)	LET at Bragg Peak
15 A MeV	$^4\text{He}$	4.003	15	60	0,4	1423	2	1421	0,11	0,11	1,5
	$^{14}\text{N}$	14.003	15	210	7	428	7	421	1,3	1,3	6,7
	$^{20}\text{Ne}$	19.992	15	300	14	316	8	308	2,5	2,6	9,6
	$^{40}\text{Ar}$	39.962	15	599	29	229	9	220	7,7	8,0	20,1
	$^{63}\text{Cu}$	62.930	15	944	90	172	16	156	17,8	18,7	34,0
	$^{84}\text{Kr}$	83.912	15	1259	152	170	21	149	25,4	26,6	41,4
	$^{109}\text{Ag}$	108.905	15	1634	248	156	26	130	38,5	40,3	54,8
	$^{129}\text{Xe}$	128.905	15	1934	339	156	31	124	47,3	49,3	63,4
	$^{141}\text{Pr}$	140.908	15	2114	441	154	37	117	53,8	56,0	69,6
	$^{165}\text{Ho}$	164.930	15	2474	608	156	44	112	64,3	66,7	79,2
	$^{181}\text{Ta}$	180.948	15	2714	702	155	46	109	72,2	74,8	86,4
$^{197}\text{Au}$	196.967	15	2954	902	155	53	102	80,2	82,8	93,5	
25 A MeV	$^4\text{He}$	4.003	24,8	99	0,4	3449	2	3447	0,07	0,07	1,5
	$^{14}\text{N}$	14.003	24,8	347	7	1009	7	1002	0,9	0,9	6,7
	$^{22}\text{Ne}$	21.991	24,8	545	14	799	8	791	1,7	1,8	9,7
	$^{40}\text{Ar}$	39.962	24,8	991	29	493	9	484	5,4	5,5	20,1
	$^{84}\text{Kr}$	83.912	24,8	2081	152	332	21	311	19,3	19,8	41,4
	$^{129}\text{Xe}$	128.905	24,8	3197	335	286	31	255	37,9	38,9	63,4
40 A MeV	$^{14}\text{N}$	14.003	40	560	7	2334	7	2327	0,6	0,6	6,7
	$^{20}\text{Ne}$	19.992	40	800	14	1655	8	1647	1,2	1,2	9,7
	$^{40}\text{Ar}$	39.962	40	1598	29	1079	9	1070	3,8	3,8	20,1
	$^{78}\text{Kr}$	77.920	40	3117	140	622	20	602	14,2	14,4	41,4
	Proton	1.007	40	40	0,1	8148	1,2	8147	0,012	0,012	0,56

Figure B.1 Beam list provided by the testing facility at Texas A&amp;M University [19].

APPENDIX C

SRIM OUTPUT TEXT TILE EXAMPLE

Disk File Name = SRIM Outputs\Krypton in Silicon

Ion = Krypton [36] , Mass = 83.912 amu

Target Density = 2.3212E+00 g/cm<sup>3</sup> = 4.9770E+22 atoms/cm<sup>3</sup>

=====  
Target Composition  
=====

Atom Name	Atom Numb	Atomic Percent	Mass Percent
-----------	-----------	----------------	--------------

Si	14	100.00	100.00
----	----	--------	--------

=====  
Bragg Correction = 0.00%

Stopping Units = MeV / (mg/cm<sup>2</sup>)

See bottom of Table for other Stopping units

Ion Energy	dE/dx Elec.	dE/dx Nuclear	Projected Range	Long. Stragglng	Lateral Stragglng
1.00 eV	1.298E-01	1.836E+00	35 A	15 A	11 A
1.10 keV	1.361E-01	1.917E+00	37 A	15 A	11 A
1.20 keV	1.421E-01	1.994E+00	38 A	16 A	12 A
1.30 keV	1.479E-01	2.066E+00	40 A	17 A	12 A
1.40 keV	1.535E-01	2.134E+00	41 A	17 A	12 A
1.50 keV	1.589E-01	2.199E+00	42 A	18 A	13 A
1.60 keV	1.641E-01	2.261E+00	44 A	18 A	13 A
1.70 keV	1.692E-01	2.319E+00	45 A	19 A	14 A
1.80 keV	1.741E-01	2.376E+00	46 A	19 A	14 A
2.00 keV	1.835E-01	2.481E+00	49 A	20 A	15 A
2.25 keV	1.946E-01	2.603E+00	52 A	21 A	15 A
2.50 keV	2.052E-01	2.714E+00	55 A	22 A	16 A
2.75 keV	2.152E-01	2.816E+00	58 A	23 A	17 A
3.00 keV	2.247E-01	2.911E+00	60 A	24 A	18 A
3.25 keV	2.339E-01	3.000E+00	63 A	25 A	18 A
3.50 keV	2.427E-01	3.083E+00	66 A	26 A	19 A
3.75 keV	2.513E-01	3.161E+00	68 A	27 A	20 A
4.00 keV	2.595E-01	3.234E+00	70 A	27 A	20 A
4.50 keV	2.752E-01	3.370E+00	75 A	29 A	22 A
5.00 keV	2.901E-01	3.492E+00	80 A	30 A	23 A
5.50 keV	3.043E-01	3.604E+00	84 A	32 A	24 A
6.00 keV	3.178E-01	3.706E+00	88 A	33 A	25 A
6.50 keV	3.308E-01	3.801E+00	93 A	35 A	26 A
7.00 keV	3.433E-01	3.888E+00	97 A	36 A	27 A
8.00 keV	3.670E-01	4.046E+00	105 A	38 A	29 A
9.00 keV	3.893E-01	4.184E+00	112 A	41 A	31 A

10.00 keV	4.103E-01	4.307E+00	120 A	43 A	33 A
11.00 keV	4.303E-01	4.416E+00	127 A	45 A	34 A
12.00 keV	4.495E-01	4.516E+00	134 A	47 A	36 A
13.00 keV	4.678E-01	4.606E+00	141 A	49 A	38 A
14.00 keV	4.855E-01	4.688E+00	148 A	51 A	39 A
15.00 keV	5.025E-01	4.763E+00	155 A	53 A	41 A
16.00 keV	5.190E-01	4.832E+00	161 A	55 A	43 A
17.00 keV	5.350E-01	4.896E+00	168 A	57 A	44 A
18.00 keV	5.505E-01	4.956E+00	174 A	59 A	46 A
20.00 keV	5.803E-01	5.062E+00	187 A	63 A	49 A
22.50 keV	6.155E-01	5.176E+00	203 A	67 A	52 A
25.00 keV	6.488E-01	5.273E+00	218 A	71 A	55 A
27.50 keV	6.804E-01	5.356E+00	233 A	75 A	59 A
30.00 keV	7.107E-01	5.428E+00	248 A	79 A	62 A
32.50 keV	7.397E-01	5.490E+00	262 A	83 A	65 A
35.00 keV	7.676E-01	5.544E+00	277 A	87 A	68 A
37.50 keV	7.946E-01	5.591E+00	291 A	91 A	71 A
40.00 keV	8.206E-01	5.633E+00	305 A	95 A	74 A
45.00 keV	8.704E-01	5.701E+00	333 A	102 A	80 A
50.00 keV	9.175E-01	5.753E+00	361 A	109 A	86 A
55.00 keV	9.623E-01	5.793E+00	388 A	116 A	92 A
60.00 keV	1.005E+00	5.822E+00	415 A	123 A	97 A
65.00 keV	1.046E+00	5.844E+00	442 A	130 A	103 A
70.00 keV	1.086E+00	5.858E+00	469 A	137 A	108 A
80.00 keV	1.161E+00	5.872E+00	522 A	150 A	118 A
90.00 keV	1.231E+00	5.870E+00	574 A	163 A	129 A
100.00 keV	1.298E+00	5.856E+00	627 A	176 A	139 A
110.00 keV	1.361E+00	5.834E+00	679 A	188 A	149 A
120.00 keV	1.421E+00	5.805E+00	731 A	201 A	158 A
130.00 keV	1.479E+00	5.772E+00	783 A	213 A	168 A
140.00 keV	1.535E+00	5.736E+00	835 A	225 A	177 A
150.00 keV	1.589E+00	5.697E+00	887 A	237 A	187 A
160.00 keV	1.641E+00	5.656E+00	940 A	249 A	196 A
170.00 keV	1.652E+00	5.613E+00	992 A	260 A	205 A
180.00 keV	1.539E+00	5.570E+00	1045 A	272 A	214 A
200.00 keV	1.407E+00	5.482E+00	1154 A	297 A	233 A
225.00 keV	1.358E+00	5.371E+00	1296 A	329 A	256 A
250.00 keV	1.384E+00	5.261E+00	1440 A	360 A	279 A
275.00 keV	1.449E+00	5.154E+00	1585 A	392 A	303 A
300.00 keV	1.534E+00	5.050E+00	1732 A	423 A	326 A
325.00 keV	1.625E+00	4.949E+00	1880 A	454 A	350 A
350.00 keV	1.717E+00	4.852E+00	2028 A	484 A	374 A
375.00 keV	1.807E+00	4.759E+00	2176 A	514 A	398 A
400.00 keV	1.891E+00	4.669E+00	2324 A	543 A	422 A

450.00 keV	2.044E+00	4.500E+00	2623 A	601 A	470 A
500.00 keV	2.175E+00	4.344E+00	2923 A	658 A	518 A
550.00 keV	2.289E+00	4.199E+00	3226 A	713 A	565 A
600.00 keV	2.389E+00	4.065E+00	3531 A	767 A	613 A
650.00 keV	2.479E+00	3.941E+00	3838 A	819 A	660 A
700.00 keV	2.563E+00	3.825E+00	4148 A	871 A	707 A
800.00 keV	2.721E+00	3.616E+00	4773 A	974 A	801 A
900.00 keV	2.875E+00	3.432E+00	5405 A	1074 A	894 A
1.00 MeV	3.031E+00	3.269E+00	6040 A	1169 A	986 A
1.10 MeV	3.192E+00	3.123E+00	6677 A	1261 A	1076 A
1.20 MeV	3.360E+00	2.991E+00	7313 A	1349 A	1166 A
1.30 MeV	3.533E+00	2.872E+00	7946 A	1433 A	1254 A
1.40 MeV	3.712E+00	2.764E+00	8574 A	1513 A	1340 A
1.50 MeV	3.895E+00	2.665E+00	9195 A	1590 A	1424 A
1.60 MeV	4.082E+00	2.574E+00	9810 A	1662 A	1507 A
1.70 MeV	4.272E+00	2.490E+00	1.04 um	1731 A	1587 A
1.80 MeV	4.464E+00	2.412E+00	1.10 um	1797 A	1665 A
2.00 MeV	4.850E+00	2.272E+00	1.22 um	1922 A	1814 A
2.25 MeV	5.332E+00	2.121E+00	1.36 um	2062 A	1988 A
2.50 MeV	5.807E+00	1.992E+00	1.49 um	2187 A	2148 A
2.75 MeV	6.271E+00	1.880E+00	1.62 um	2297 A	2297 A
3.00 MeV	6.720E+00	1.782E+00	1.75 um	2395 A	2434 A
3.25 MeV	7.153E+00	1.695E+00	1.87 um	2484 A	2561 A
3.50 MeV	7.570E+00	1.617E+00	1.98 um	2564 A	2679 A
3.75 MeV	7.970E+00	1.546E+00	2.09 um	2637 A	2789 A
4.00 MeV	8.354E+00	1.483E+00	2.20 um	2703 A	2892 A
4.50 MeV	9.078E+00	1.372E+00	2.41 um	2828 A	3080 A
5.00 MeV	9.750E+00	1.279E+00	2.60 um	2935 A	3246 A
5.50 MeV	1.038E+01	1.199E+00	2.79 um	3028 A	3395 A
6.00 MeV	1.096E+01	1.129E+00	2.97 um	3110 A	3530 A
6.50 MeV	1.152E+01	1.068E+00	3.14 um	3183 A	3653 A
7.00 MeV	1.205E+01	1.014E+00	3.30 um	3249 A	3765 A
8.00 MeV	1.305E+01	9.228E-01	3.62 um	3377 A	3965 A
9.00 MeV	1.398E+01	8.480E-01	3.91 um	3484 A	4138 A
10.00 MeV	1.486E+01	7.857E-01	4.19 um	3575 A	4290 A
11.00 MeV	1.570E+01	7.328E-01	4.45 um	3654 A	4424 A
12.00 MeV	1.650E+01	6.872E-01	4.71 um	3724 A	4544 A
13.00 MeV	1.727E+01	6.475E-01	4.95 um	3785 A	4653 A
14.00 MeV	1.801E+01	6.126E-01	5.18 um	3841 A	4751 A
15.00 MeV	1.871E+01	5.817E-01	5.41 um	3891 A	4842 A
16.00 MeV	1.939E+01	5.540E-01	5.63 um	3936 A	4925 A
17.00 MeV	2.005E+01	5.291E-01	5.84 um	3977 A	5001 A
18.00 MeV	2.067E+01	5.065E-01	6.04 um	4016 A	5073 A
20.00 MeV	2.185E+01	4.672E-01	6.44 um	4102 A	5201 A

22.50 MeV	2.319E+01	4.266E-01	6.90 um	4206 A	5341 A
25.00 MeV	2.439E+01	3.930E-01	7.35 um	4295 A	5463 A
27.50 MeV	2.549E+01	3.648E-01	7.77 um	4373 A	5571 A
30.00 MeV	2.648E+01	3.406E-01	8.18 um	4443 A	5667 A
32.50 MeV	2.738E+01	3.198E-01	8.57 um	4507 A	5755 A
35.00 MeV	2.820E+01	3.015E-01	8.95 um	4565 A	5834 A
37.50 MeV	2.895E+01	2.854E-01	9.32 um	4618 A	5908 A
40.00 MeV	2.964E+01	2.710E-01	9.69 um	4668 A	5976 A
45.00 MeV	3.087E+01	2.466E-01	10.39 um	4811 A	6099 A
50.00 MeV	3.193E+01	2.265E-01	11.07 um	4937 A	6209 A
55.00 MeV	3.286E+01	2.096E-01	11.73 um	5053 A	6307 A
60.00 MeV	3.367E+01	1.953E-01	12.37 um	5159 A	6396 A
65.00 MeV	3.439E+01	1.829E-01	13.00 um	5257 A	6479 A
70.00 MeV	3.503E+01	1.721E-01	13.62 um	5350 A	6555 A
80.00 MeV	3.613E+01	1.542E-01	14.82 um	5649 A	6694 A
90.00 MeV	3.704E+01	1.399E-01	15.99 um	5917 A	6817 A
100.00 MeV	3.780E+01	1.282E-01	17.14 um	6161 A	6929 A
110.00 MeV	3.844E+01	1.184E-01	18.26 um	6387 A	7032 A
120.00 MeV	3.898E+01	1.101E-01	19.37 um	6598 A	7128 A
130.00 MeV	3.944E+01	1.030E-01	20.47 um	6796 A	7218 A
140.00 MeV	3.984E+01	9.676E-02	21.55 um	6984 A	7303 A
150.00 MeV	4.018E+01	9.130E-02	22.62 um	7164 A	7384 A
160.00 MeV	4.047E+01	8.646E-02	23.69 um	7336 A	7461 A
170.00 MeV	4.073E+01	8.214E-02	24.75 um	7502 A	7534 A
180.00 MeV	4.092E+01	7.827E-02	25.80 um	7662 A	7605 A
200.00 MeV	4.080E+01	7.157E-02	27.90 um	8244 A	7741 A
225.00 MeV	4.077E+01	6.475E-02	30.54 um	9074 A	7901 A
250.00 MeV	4.066E+01	5.918E-02	33.18 um	9836 A	8054 A
275.00 MeV	4.046E+01	5.455E-02	35.83 um	1.05 um	8200 A
300.00 MeV	4.020E+01	5.062E-02	38.50 um	1.12 um	8341 A
325.00 MeV	3.989E+01	4.726E-02	41.18 um	1.19 um	8479 A
350.00 MeV	3.954E+01	4.434E-02	43.89 um	1.25 um	8614 A
375.00 MeV	3.916E+01	4.178E-02	46.63 um	1.31 um	8747 A
400.00 MeV	3.876E+01	3.951E-02	49.39 um	1.37 um	8879 A
450.00 MeV	3.791E+01	3.569E-02	55.00 um	1.58 um	9138 A
500.00 MeV	3.703E+01	3.257E-02	60.75 um	1.78 um	9396 A
550.00 MeV	3.614E+01	2.998E-02	66.63 um	1.97 um	9653 A
600.00 MeV	3.525E+01	2.779E-02	72.66 um	2.15 um	9912 A
650.00 MeV	3.437E+01	2.592E-02	78.85 um	2.32 um	1.02 um
700.00 MeV	3.351E+01	2.429E-02	85.19 um	2.49 um	1.04 um
800.00 MeV	3.186E+01	2.162E-02	98.37 um	3.12 um	1.10 um
900.00 MeV	3.032E+01	1.949E-02	112.22 um	3.68 um	1.15 um
1.00 GeV	2.889E+01	1.777E-02	126.77 um	4.22 um	1.21 um
1.10 GeV	2.756E+01	1.634E-02	142.04 um	4.75 um	1.27 um

1.20 GeV	2.633E+01	1.513E-02	158.03 um	5.26 um	1.34 um
1.30 GeV	2.519E+01	1.410E-02	174.75 um	5.77 um	1.41 um
1.40 GeV	2.413E+01	1.321E-02	192.22 um	6.28 um	1.48 um
1.50 GeV	2.316E+01	1.243E-02	210.44 um	6.79 um	1.55 um
1.60 GeV	2.226E+01	1.174E-02	229.41 um	7.31 um	1.63 um
1.70 GeV	2.143E+01	1.112E-02	249.13 um	7.82 um	1.71 um
1.80 GeV	2.066E+01	1.057E-02	269.60 um	8.35 um	1.79 um
1.83 GeV	2.047E+01	1.042E-02	275.73 um	8.39 um	1.81 um

-----  
 Multiply Stopping by            for Stopping Units

2.3211E+01	eV / Angstrom
2.3211E+02	keV / micron
2.3211E+02	MeV / mm
1.0000E+00	keV / (ug/cm2)
1.0000E+00	MeV / (mg/cm2)
1.0000E+03	keV / (mg/cm2)
4.6637E+01	eV / (1E15 atoms/cm2)
5.9669E-02	L.S.S. reduced units

=====  
 (C) 1984,1989,1992,1998,2008 by J.P. Biersack and J.F. Ziegler

APPENDIX D

TEST RUN DATA

Run number : 1  
 Run file name : Montana Mar 2012.#00  
 Run start date and time : 12/03/06 09:16:48  
 Run end date and time : 12/03/06 09:27:01  
 Duration of the run : 00:10:13 (+ 0 days)  
 Number of events : 0

Selected beam : 24.8 MeV/u Kr  
 Al degrader thickness (mil) : 0.000  
 Number of layers (layer file name) : 3 (MSU\_60)  
 Beam energy (MeV/amu) : 21.8  
 Beam energy (MeV) : 1830  
 Target material : silicon  
 Nominal LET (MeVcm<sup>2</sup>/mg) : 20.8  
 Nominal range (um) : 278.4  
 Effective LET (MeVcm<sup>2</sup>/mg) : 20.8  
 Effective range (um) : 278.4  
 DUT location : In-air  
 Position set name : Current

Effective fluence (ions/cm<sup>2</sup>) : 1.260E+006  
 Dose (rad) : 4.199E+002  
 Live time (s) : 599.067  
 Dead time (s) : 5.05  
 Average flux (ions/(cm<sup>2</sup>s)) : 2.103E+003  
 Average flux error (%) : 0.14  
 Overall uniformity (%) : 97  
 Overall central shift (%) : 2  
 Calibration factor : 1.01779

DUT X coordinate : 0.295 in  
 DUT Y coordinate : -0.119 in  
 DUT Z coordinate : -15.838 cm  
 DUT tilt angle : 0.000 deg  
 Roll angle : -82.225 deg  
 Unused coordinate : 0.100 in  
 Selected Al degrader number : -0.000 steps  
 Degradation rotation angle : 0.000 deg  
 Detector bias (V) : 361 311 331 361 331

Layer summary:

silicon ROT 0 um  
 aramica ROT 1 mil  
 air gas ROT 60 mm

Run number : 2  
 Run file name : Montana Mar 2012.#01  
 Run start date and time : 12/03/06 09:39:29  
 Run end date and time : 12/03/06 09:52:40  
 Duration of the run : 00:13:11 (+ 0 days)  
 Number of events : 0

Selected beam : 24.8 MeV/u Kr  
 Al degrader thickness (mil) : 0.000  
 Number of layers (layer file name) : 3 (MSU\_60)  
 Beam energy (MeV/amu) : 21.8  
 Beam energy (MeV) : 1830  
 Target material : silicon  
 Nominal LET (MeVcm<sup>2</sup>/mg) : 20.8  
 Nominal range (um) : 278.4  
 Effective LET (MeVcm<sup>2</sup>/mg) : 20.8  
 Effective range (um) : 278.4  
 DUT location : In-air  
 Position set name : Current

Effective fluence (ions/cm<sup>2</sup>) : 1.258E+006  
 Dose (rad) : 4.192E+002  
 Live time (s) : 600.133  
 Dead time (s) : 181.8  
 Average flux (ions/(cm<sup>2</sup>s)) : 2.096E+003  
 Average flux error (%) : 0.14  
 Overall uniformity (%) : 97  
 Overall central shift (%) : 2  
 Calibration factor : 1.02028

DUT X coordinate : 0.295 in  
 DUT Y coordinate : -0.119 in  
 DUT Z coordinate : -15.838 cm  
 DUT tilt angle : 0.000 deg  
 Roll angle : -82.225 deg  
 Unused coordinate : 0.100 in  
 Selected Al degrader number : -0.000 steps  
 Degradation rotation angle : 0.000 deg  
 Detector bias (V) : 361 311 331 361 331

Layer summary:

silicon ROT 0 um  
 aramica ROT 1 mil  
 air gas ROT 60 mm

Run number : 3  
 Run file name : Montana Mar 2012.#02  
 Run start date and time : 12/03/06 10:00:07  
 Run end date and time : 12/03/06 10:12:31  
 Duration of the run : 00:12:24 (+ 0 days)  
 Number of events : 0

Selected beam : 24.8 MeV/u Kr  
 Al degrader thickness (mil) : 0.000  
 Number of layers (layer file name) : 3 (MSU\_60)  
 Beam energy (MeV/amu) : 21.8  
 Beam energy (MeV) : 1830  
 Target material : silicon  
 Nominal LET (MeVcm<sup>2</sup>/mg) : 20.8  
 Nominal range (um) : 278.4  
 Effective LET (MeVcm<sup>2</sup>/mg) : 20.8  
 Effective range (um) : 278.4  
 DUT location : In-air  
 Position set name : Current

Effective fluence (ions/cm<sup>2</sup>) : 1.302E+006  
 Dose (rad) : 4.340E+002  
 Live time (s) : 599.717  
 Dead time (s) : 136  
 Average flux (ions/(cm<sup>2</sup>s)) : 2.172E+003  
 Average flux error (%) : 0.14  
 Overall uniformity (%) : 92  
 Overall central shift (%) : 5  
 Calibration factor : 0.99316

DUT X coordinate : 0.295 in  
 DUT Y coordinate : -0.119 in  
 DUT Z coordinate : -15.838 cm  
 DUT tilt angle : 0.000 deg  
 Roll angle : -82.225 deg  
 Unused coordinate : 0.100 in  
 Selected Al degrader number : -0.000 steps  
 Degradation rotation angle : 0.000 deg  
 Detector bias (V) : 361 311 331 361 331

Layer summary:

silicon ROT 0 um  
 aramica ROT 1 mil  
 air gas ROT 60 mm

Run number : 4  
 Run file name : Montana Mar 2012.#03  
 Run start date and time : 12/03/06 10:17:02  
 Run end date and time : 12/03/06 10:28:05  
 Duration of the run : 00:11:03 (+ 0 days)  
 Number of events : 0

Selected beam : 24.8 MeV/u Kr  
 Al degrader thickness (mil) : 0.000  
 Number of layers (layer file name) : 3 (MSU\_60)  
 Beam energy (MeV/amu) : 21.8  
 Beam energy (MeV) : 1830  
 Target material : silicon  
 Nominal LET (MeVcm<sup>2</sup>/mg) : 20.8  
 Nominal range (um) : 278.4  
 Effective LET (MeVcm<sup>2</sup>/mg) : 20.8  
 Effective range (um) : 278.4  
 DUT location : In-air  
 Position set name : Current

Effective fluence (ions/cm<sup>2</sup>) : 1.352E+006  
 Dose (rad) : 4.505E+002  
 Live time (s) : 600.167  
 Dead time (s) : 56.9833  
 Average flux (ions/(cm<sup>2</sup>s)) : 2.253E+003  
 Average flux error (%) : 0.14  
 Overall uniformity (%) : 93  
 Overall central shift (%) : 5  
 Calibration factor : 0.997006

DUT X coordinate : 0.295 in  
 DUT Y coordinate : -0.119 in  
 DUT Z coordinate : -15.838 cm  
 DUT tilt angle : 0.000 deg  
 Roll angle : -82.225 deg  
 Unused coordinate : 0.100 in  
 Selected Al degrader number : -0.000 steps  
 Degradation rotation angle : 0.000 deg  
 Detector bias (V) : 361 311 331 361 331

Layer summary:

silicon ROT 0 um  
 aramica ROT 1 mil  
 air gas ROT 60 mm

Run number : 5  
 Run file name : Montana Mar 2012.#04  
 Run start date and time : 12/03/06 10:32:15  
 Run end date and time : 12/03/06 10:47:39  
 Duration of the run : 00:15:24 (+ 0 days)  
 Number of events : 0

Selected beam : 24.8 MeV/u Kr  
 Al degrader thickness (mil) : 0.000  
 Number of layers (layer file name) : 3 (MSU\_60)  
 Beam energy (MeV/amu) : 21.8  
 Beam energy (MeV) : 1830  
 Target material : silicon  
 Nominal LET (MeVcm<sup>2</sup>/mg) : 20.8  
 Nominal range (um) : 278.4  
 Effective LET (MeVcm<sup>2</sup>/mg) : 20.8  
 Effective range (um) : 278.4  
 DUT location : In-air  
 Position set name : Current

Effective fluence (ions/cm<sup>2</sup>) : 1.261E+006  
 Dose (rad) : 4.201E+002  
 Live time (s) : 556.733  
 Dead time (s) : 360.683  
 Average flux (ions/(cm<sup>2</sup>s)) : 2.264E+003  
 Average flux error (%) : 0.14  
 Overall uniformity (%) : 93  
 Overall central shift (%) : 3  
 Calibration factor : 0.997006

DUT X coordinate : 0.295 in  
 DUT Y coordinate : -0.119 in  
 DUT Z coordinate : -15.838 cm  
 DUT tilt angle : 0.000 deg  
 Roll angle : -82.225 deg  
 Unused coordinate : 0.100 in  
 Selected Al degrader number : -0.000 steps  
 Degradation rotation angle : 0.000 deg  
 Detector bias (V) : 361 311 331 361 331

Layer summary:

silicon ROT 0 um  
 aramica ROT 1 mil  
 air gas ROT 60 mm

Run number : 6  
 Run file name : Montana Mar 2012.#05  
 Run start date and time : 12/03/06 11:01:57  
 Run end date and time : 12/03/06 11:02:49  
 Duration of the run : 00:00:52 (+ 0 days)  
 Number of events : 0

Selected beam : 24.8 MeV/u Kr  
 Al degrader thickness (mil) : 0.000  
 Number of layers (layer file name) : 3 (MSU\_60)  
 Beam energy (MeV/amu) : 21.8  
 Beam energy (MeV) : 1830  
 Target material : silicon  
 Nominal LET (MeVcm<sup>2</sup>/mg) : 20.8  
 Nominal range (um) : 278.4  
 Effective LET (MeVcm<sup>2</sup>/mg) : 20.8  
 Effective range (um) : 278.4  
 DUT location : In-air  
 Position set name : Current

Effective fluence (ions/cm<sup>2</sup>) : 1.198E+005  
 Dose (rad) : 3.994E+001  
 Live time (s) : 44.95  
 Dead time (s) : 0  
 Average flux (ions/(cm<sup>2</sup>s)) : 2.666E+003  
 Average flux error (%) : 0.46  
 Overall uniformity (%) : 93  
 Overall central shift (%) : 5  
 Calibration factor : 0.993115

DUT X coordinate : 0.295 in  
 DUT Y coordinate : -0.119 in  
 DUT Z coordinate : -15.838 cm  
 DUT tilt angle : 0.000 deg  
 Roll angle : -82.225 deg  
 Unused coordinate : 0.100 in  
 Selected Al degrader number : -0.000 steps  
 Degradation rotation angle : 0.000 deg  
 Detector bias (V) : 361 311 331 361 331

Layer summary:

silicon ROT 0 um  
 aramica ROT 1 mil  
 air gas ROT 60 mm

Run number : 7  
 Run file name : Montana Mar 2012.#06  
 Run start date and time : 12/03/06 11:12:20  
 Run end date and time : 12/03/06 11:22:39  
 Duration of the run : 00:10:19 (+ 0 days)  
 Number of events : 0

Selected beam : 24.8 MeV/u Kr  
 Al degrader thickness (mil) : 0.000  
 Number of layers (layer file name) : 3 (MSU\_60)  
 Beam energy (MeV/amu) : 21.8  
 Beam energy (MeV) : 1830  
 Target material : silicon  
 Nominal LET (MeVcm<sup>2</sup>/mg) : 20.8  
 Nominal range (um) : 278.4  
 Effective LET (MeVcm<sup>2</sup>/mg) : 20.8  
 Effective range (um) : 278.4  
 DUT location : In-air  
 Position set name : Current

Effective fluence (ions/cm<sup>2</sup>) : 1.409E+006  
 Dose (rad) : 4.697E+002  
 Live time (s) : 599.7  
 Dead time (s) : 12.15  
 Average flux (ions/(cm<sup>2</sup>s)) : 2.350E+003  
 Average flux error (%) : 0.13  
 Overall uniformity (%) : 87  
 Overall central shift (%) : 9  
 Calibration factor : 0.993115

DUT X coordinate : 0.295 in  
 DUT Y coordinate : -0.119 in  
 DUT Z coordinate : -17.016 cm  
 DUT tilt angle : 0.000 deg  
 Roll angle : -82.225 deg  
 Unused coordinate : 0.100 in  
 Selected Al degrader number : -0.000 steps  
 Degradation rotation angle : 0.000 deg  
 Detector bias (V) : 361 311 331 361 331

Layer summary:

silicon ROT 0 um  
 aramica ROT 1 mil  
 air gas ROT 60 mm

Run number : 8  
 Run file name : Montana Mar 2012.#07  
 Run start date and time : 12/03/06 11:26:14  
 Run end date and time : 12/03/06 11:36:46  
 Duration of the run : 00:10:32 (+ 0 days)  
 Number of events : 0

Selected beam : 24.8 MeV/u Kr  
 Al degrader thickness (mil) : 0.000  
 Number of layers (layer file name) : 3 (MSU\_60)  
 Beam energy (MeV/amu) : 21.8  
 Beam energy (MeV) : 1830  
 Target material : silicon  
 Nominal LET (MeVcm<sup>2</sup>/mg) : 20.8  
 Nominal range (um) : 278.4  
 Effective LET (MeVcm<sup>2</sup>/mg) : 20.8  
 Effective range (um) : 278.4  
 DUT location : In-air  
 Position set name : Current

Effective fluence (ions/cm<sup>2</sup>) : 1.210E+006  
 Dose (rad) : 4.032E+002  
 Live time (s) : 600.483  
 Dead time (s) : 26.9833  
 Average flux (ions/(cm<sup>2</sup>s)) : 2.015E+003  
 Average flux error (%) : 0.14  
 Overall uniformity (%) : 85  
 Overall central shift (%) : 11  
 Calibration factor : 0.94076

DUT X coordinate : 0.295 in  
 DUT Y coordinate : -0.119 in  
 DUT Z coordinate : -17.016 cm  
 DUT tilt angle : 0.000 deg  
 Roll angle : -82.225 deg  
 Unused coordinate : 0.100 in  
 Selected Al degrader number : -0.000 steps  
 Degradation rotation angle : 0.000 deg  
 Detector bias (V) : 361 311 331 361 331

Layer summary:

silicon ROT 0 um  
 aramica ROT 1 mil  
 air gas ROT 60 mm

Run number : 9  
 Run file name : Montana Mar 2012.#08  
 Run start date and time : 12/03/06 11:40:38  
 Run end date and time : 12/03/06 11:53:43  
 Duration of the run : 00:13:05 (+ 0 days)  
 Number of events : 0

Selected beam : 24.8 MeV/u Kr  
 Al degrader thickness (mil) : 0.000  
 Number of layers (layer file name) : 3 (MSU\_60)  
 Beam energy (MeV/amu) : 21.8  
 Beam energy (MeV) : 1830  
 Target material : silicon  
 Nominal LET (MeVcm<sup>2</sup>/mg) : 20.8  
 Nominal range (um) : 278.4  
 Effective LET (MeVcm<sup>2</sup>/mg) : 20.8  
 Effective range (um) : 278.4  
 DUT location : In-air  
 Position set name : Current

Effective fluence (ions/cm<sup>2</sup>) : 1.267E+006  
 Dose (rad) : 4.221E+002  
 Live time (s) : 599.717  
 Dead time (s) : 178.133  
 Average flux (ions/(cm<sup>2</sup>s)) : 2.112E+003  
 Average flux error (%) : 0.14  
 Overall uniformity (%) : 89  
 Overall central shift (%) : 6  
 Calibration factor : 0.965609

DUT X coordinate : 0.295 in  
 DUT Y coordinate : -0.119 in  
 DUT Z coordinate : -17.016 cm  
 DUT tilt angle : 0.000 deg  
 Roll angle : -82.225 deg  
 Unused coordinate : 0.100 in  
 Selected Al degrader number : -0.000 steps  
 Degradation rotation angle : 0.000 deg  
 Detector bias (V) : 361 311 331 361 331

Layer summary:

silicon ROT 0 um  
 aramica ROT 1 mil  
 air gas ROT 60 mm

Run number : 10  
 Run file name : Montana Mar 2012.#09  
 Run start date and time : 12/03/06 11:58:22  
 Run end date and time : 12/03/06 12:13:20  
 Duration of the run : 00:14:58 (+ 0 days)  
 Number of events : 0

Selected beam : 24.8 MeV/u Kr  
 Al degrader thickness (mil) : 0.000  
 Number of layers (layer file name) : 3 (MSU\_60)  
 Beam energy (MeV/amu) : 21.8  
 Beam energy (MeV) : 1830  
 Target material : silicon  
 Nominal LET (MeVcm<sup>2</sup>/mg) : 20.8  
 Nominal range (um) : 278.4  
 Effective LET (MeVcm<sup>2</sup>/mg) : 20.8  
 Effective range (um) : 278.4  
 DUT location : In-air  
 Position set name : Current

Effective fluence (ions/cm<sup>2</sup>) : 1.276E+006  
 Dose (rad) : 4.253E+002  
 Live time (s) : 599.75  
 Dead time (s) : 292.983  
 Average flux (ions/(cm<sup>2</sup>s)) : 2.128E+003  
 Average flux error (%) : 0.14  
 Overall uniformity (%) : 88  
 Overall central shift (%) : 6  
 Calibration factor : 0.965609

DUT X coordinate : 0.295 in  
 DUT Y coordinate : -0.119 in  
 DUT Z coordinate : -17.016 cm  
 DUT tilt angle : 0.000 deg  
 Roll angle : -82.225 deg  
 Unused coordinate : 0.100 in  
 Selected Al degrader number : -0.000 steps  
 Degradation rotation angle : 0.000 deg  
 Detector bias (V) : 361 311 331 361 331

Layer summary:

silicon ROT 0 um  
 aramica ROT 1 mil  
 air gas ROT 60 mm

Run number : 11  
 Run file name : Montana Mar 2012.#0a  
 Run start date and time : 12/03/06 12:18:47  
 Run end date and time : 12/03/06 12:23:52  
 Duration of the run : 00:05:05 (+ 0 days)  
 Number of events : 0

Selected beam : 24.8 MeV/u Kr  
 Al degrader thickness (mil) : 0.000  
 Number of layers (layer file name) : 3 (MSU\_60)  
 Beam energy (MeV/amu) : 21.8  
 Beam energy (MeV) : 1830  
 Target material : silicon  
 Nominal LET (MeVcm<sup>2</sup>/mg) : 20.8  
 Nominal range (um) : 278.4  
 Effective LET (MeVcm<sup>2</sup>/mg) : 20.8  
 Effective range (um) : 278.4  
 DUT location : In-air  
 Position set name : Current

Effective fluence (ions/cm<sup>2</sup>) : 5.629E+005  
 Dose (rad) : 1.876E+002  
 Live time (s) : 299.683  
 Dead time (s) : 0  
 Average flux (ions/(cm<sup>2</sup>s)) : 1.878E+003  
 Average flux error (%) : 0.21  
 Overall uniformity (%) : 86  
 Overall central shift (%) : 10  
 Calibration factor : 0.965609

DUT X coordinate : 0.295 in  
 DUT Y coordinate : -0.119 in  
 DUT Z coordinate : -17.016 cm  
 DUT tilt angle : 0.000 deg  
 Roll angle : -82.225 deg  
 Unused coordinate : 0.100 in  
 Selected Al degrader number : -0.000 steps  
 Degradation rotation angle : 0.000 deg  
 Detector bias (V) : 361 311 331 361 331

Layer summary:

silicon ROT 0 um  
 aramica ROT 1 mil  
 air gas ROT 60 mm

Run number : 12  
 Run file name : Montana Mar 2012.#0b  
 Run start date and time : 12/03/06 12:28:51  
 Run end date and time : 12/03/06 12:34:27  
 Duration of the run : 00:05:36 (+ 0 days)  
 Number of events : 0

Selected beam : 24.8 MeV/u Kr  
 Al degrader thickness (mil) : 0.000  
 Number of layers (layer file name) : 3 (MSU\_60)  
 Beam energy (MeV/amu) : 21.8  
 Beam energy (MeV) : 1830  
 Target material : silicon  
 Nominal LET (MeVcm<sup>2</sup>/mg) : 20.8  
 Nominal range (um) : 278.4  
 Effective LET (MeVcm<sup>2</sup>/mg) : 20.8  
 Effective range (um) : 278.4  
 DUT location : In-air  
 Position set name : Current

Effective fluence (ions/cm<sup>2</sup>) : 5.773E+005  
 Dose (rad) : 1.924E+002  
 Live time (s) : 299.85  
 Dead time (s) : 29.05  
 Average flux (ions/(cm<sup>2</sup>s)) : 1.925E+003  
 Average flux error (%) : 0.21  
 Overall uniformity (%) : 85  
 Overall central shift (%) : 11  
 Calibration factor : 0.961317

DUT X coordinate : 0.295 in  
 DUT Y coordinate : -0.119 in  
 DUT Z coordinate : -17.016 cm  
 DUT tilt angle : 0.000 deg  
 Roll angle : -82.225 deg  
 Unused coordinate : 0.100 in  
 Selected Al degrader number : -0.000 steps  
 Degradation rotation angle : 0.000 deg  
 Detector bias (V) : 361 311 331 361 331

Layer summary:

silicon ROT 0 um  
 aramica ROT 1 mil  
 air gas ROT 60 mm

Run number : 13  
 Run file name : Montana Mar 2012.#0c  
 Run start date and time : 12/03/06 12:38:32  
 Run end date and time : 12/03/06 12:43:41  
 Duration of the run : 00:05:09 (+ 0 days)  
 Number of events : 0

Selected beam : 24.8 MeV/u Kr  
 Al degrader thickness (mil) : 0.000  
 Number of layers (layer file name) : 3 (MSU\_60)  
 Beam energy (MeV/amu) : 21.8  
 Beam energy (MeV) : 1830  
 Target material : silicon  
 Nominal LET (MeVcm<sup>2</sup>/mg) : 20.8  
 Nominal range (um) : 278.4  
 Effective LET (MeVcm<sup>2</sup>/mg) : 20.8  
 Effective range (um) : 278.4  
 DUT location : In-air  
 Position set name : Current

Effective fluence (ions/cm<sup>2</sup>) : 7.495E+005  
 Dose (rad) : 2.497E+002  
 Live time (s) : 300.3  
 Dead time (s) : 0  
 Average flux (ions/(cm<sup>2</sup>s)) : 2.496E+003  
 Average flux error (%) : 0.18  
 Overall uniformity (%) : 95  
 Overall central shift (%) : 3  
 Calibration factor : 0.953902

DUT X coordinate : 0.295 in  
 DUT Y coordinate : -0.119 in  
 DUT Z coordinate : -17.016 cm  
 DUT tilt angle : 0.000 deg  
 Roll angle : -82.225 deg  
 Unused coordinate : 0.100 in  
 Selected Al degrader number : -0.000 steps  
 Degradation rotation angle : 0.000 deg  
 Detector bias (V) : 361 311 331 361 331

Layer summary:

silicon ROT 0 um  
 aramica ROT 1 mil  
 air gas ROT 60 mm

Run number : 14  
 Run file name : Montana Mar 2012.#0d  
 Run start date and time : 12/03/06 12:49:19  
 Run end date and time : 12/03/06 12:53:55  
 Duration of the run : 00:04:36 (+ 0 days)  
 Number of events : 0

Selected beam : 24.8 MeV/u Kr  
 Al degrader thickness (mil) : 0.000  
 Number of layers (layer file name) : 3 (MSU\_60)  
 Beam energy (MeV/amu) : 21.8  
 Beam energy (MeV) : 1830  
 Target material : silicon  
 Nominal LET (MeVcm<sup>2</sup>/mg) : 20.8  
 Nominal range (um) : 278.4  
 Effective LET (MeVcm<sup>2</sup>/mg) : 20.8  
 Effective range (um) : 278.4  
 DUT location : In-air  
 Position set name : Current

Effective fluence (ions/cm<sup>2</sup>) : 1.814E+005  
 Dose (rad) : 6.044E+001  
 Live time (s) : 69.0167  
 Dead time (s) : 196.867  
 Average flux (ions/(cm<sup>2</sup>s)) : 2.628E+003  
 Average flux error (%) : 0.37  
 Overall uniformity (%) : 87  
 Overall central shift (%) : 3  
 Calibration factor : 0.983094

DUT X coordinate : 0.295 in  
 DUT Y coordinate : -0.119 in  
 DUT Z coordinate : -17.016 cm  
 DUT tilt angle : 0.000 deg  
 Roll angle : -82.225 deg  
 Unused coordinate : 0.100 in  
 Selected Al degrader number : -0.000 steps  
 Degradation rotation angle : 0.000 deg  
 Detector bias (V) : 361 311 331 361 331

Layer summary:

silicon ROT 0 um  
 aramica ROT 1 mil  
 air gas ROT 60 mm

Run number : 15  
 Run file name : Montana Mar 2012.#0e  
 Run start date and time : 12/03/06 14:21:10  
 Run end date and time : 12/03/06 14:26:46  
 Duration of the run : 00:05:36 (+ 0 days)  
 Number of events : 0

Selected beam : 24.8 MeV/u Kr  
 Al degrader thickness (mil) : 0.000  
 Number of layers (layer file name) : 3 (MSU\_60)  
 Beam energy (MeV/amu) : 21.8  
 Beam energy (MeV) : 1830  
 Target material : silicon  
 Nominal LET (MeVcm<sup>2</sup>/mg) : 20.8  
 Nominal range (um) : 278.4  
 Effective LET (MeVcm<sup>2</sup>/mg) : 20.8  
 Effective range (um) : 278.4  
 DUT location : In-air  
 Position set name : Current

Effective fluence (ions/cm<sup>2</sup>) : 5.193E+005  
 Dose (rad) : 1.731E+002  
 Live time (s) : 299.883  
 Dead time (s) : 28.0167  
 Average flux (ions/(cm<sup>2</sup>s)) : 1.732E+003  
 Average flux error (%) : 0.22  
 Overall uniformity (%) : 92  
 Overall central shift (%) : 5  
 Calibration factor : 1.01809

DUT X coordinate : 0.295 in  
 DUT Y coordinate : -0.119 in  
 DUT Z coordinate : -17.016 cm  
 DUT tilt angle : 0.000 deg  
 Roll angle : -82.225 deg  
 Unused coordinate : 0.100 in  
 Selected Al degrader number : -0.000 steps  
 Degradation rotation angle : 0.000 deg  
 Detector bias (V) : 361 311 331 361 331

Layer summary:

silicon ROT 0 um  
 aramica ROT 1 mil  
 air gas ROT 60 mm

Run number : 16  
 Run file name : Montana Mar 2012.#0f  
 Run start date and time : 12/03/06 14:31:28  
 Run end date and time : 12/03/06 14:36:36  
 Duration of the run : 00:05:08 (+ 0 days)  
 Number of events : 0

Selected beam : 24.8 MeV/u Kr  
 Al degrader thickness (mil) : 0.000  
 Number of layers (layer file name) : 3 (MSU\_60)  
 Beam energy (MeV/amu) : 21.8  
 Beam energy (MeV) : 1830  
 Target material : silicon  
 Nominal LET (MeVcm<sup>2</sup>/mg) : 20.8  
 Nominal range (um) : 278.4  
 Effective LET (MeVcm<sup>2</sup>/mg) : 20.8  
 Effective range (um) : 278.4  
 DUT location : In-air  
 Position set name : Current

Effective fluence (ions/cm<sup>2</sup>) : 4.086E+005  
 Dose (rad) : 1.362E+002  
 Live time (s) : 300.5  
 Dead time (s) : 0  
 Average flux (ions/(cm<sup>2</sup>s)) : 1.360E+003  
 Average flux error (%) : 0.25  
 Overall uniformity (%) : 88  
 Overall central shift (%) : 9  
 Calibration factor : 1.01809

DUT X coordinate : 0.295 in  
 DUT Y coordinate : -0.119 in  
 DUT Z coordinate : -17.016 cm  
 DUT tilt angle : 0.000 deg  
 Roll angle : -82.225 deg  
 Unused coordinate : 0.100 in  
 Selected Al degrader number : -0.000 steps  
 Degradation rotation angle : 0.000 deg  
 Detector bias (V) : 361 311 331 361 331

Layer summary:

silicon ROT 0 um  
 aramica ROT 1 mil  
 air gas ROT 60 mm

Run number : 17  
 Run file name : Montana Mar 2012.#0g  
 Run start date and time : 12/03/06 14:40:43  
 Run end date and time : 12/03/06 14:45:50  
 Duration of the run : 00:05:07 (+ 0 days)  
 Number of events : 0

Selected beam : 24.8 MeV/u Kr  
 Al degrader thickness (mil) : 0.000  
 Number of layers (layer file name) : 3 (MSU\_60)  
 Beam energy (MeV/amu) : 21.8  
 Beam energy (MeV) : 1830  
 Target material : silicon  
 Nominal LET (MeVcm<sup>2</sup>/mg) : 20.8  
 Nominal range (um) : 278.4  
 Effective LET (MeVcm<sup>2</sup>/mg) : 20.8  
 Effective range (um) : 278.4  
 DUT location : In-air  
 Position set name : Current

Effective fluence (ions/cm<sup>2</sup>) : 3.923E+005  
 Dose (rad) : 1.307E+002  
 Live time (s) : 300  
 Dead time (s) : 0.0333333  
 Average flux (ions/(cm<sup>2</sup>s)) : 1.308E+003  
 Average flux error (%) : 0.25  
 Overall uniformity (%) : 87  
 Overall central shift (%) : 10  
 Calibration factor : 0.987587

DUT X coordinate : 0.295 in  
 DUT Y coordinate : -0.119 in  
 DUT Z coordinate : -17.016 cm  
 DUT tilt angle : 0.000 deg  
 Roll angle : -82.225 deg  
 Unused coordinate : 0.100 in  
 Selected Al degrader number : -0.000 steps  
 Degradation rotation angle : 0.000 deg  
 Detector bias (V) : 361 311 331 361 331

Layer summary:

silicon ROT 0 um  
 aramica ROT 1 mil  
 air gas ROT 60 mm

Run number : 18  
 Run file name : Montana Mar 2012.#0h  
 Run start date and time : 12/03/06 14:55:42  
 Run end date and time : 12/03/06 15:00:59  
 Duration of the run : 00:05:17 (+ 0 days)  
 Number of events : 0

Selected beam : 24.8 MeV/u Kr  
 Al degrader thickness (mil) : 0.000  
 Number of layers (layer file name) : 3 (MSU\_60)  
 Beam energy (MeV/amu) : 21.8  
 Beam energy (MeV) : 1830  
 Target material : silicon  
 Nominal LET (MeVcm<sup>2</sup>/mg) : 20.8  
 Nominal range (um) : 278.4  
 Effective LET (MeVcm<sup>2</sup>/mg) : 20.8  
 Effective range (um) : 278.4  
 DUT location : In-air  
 Position set name : Current

Effective fluence (ions/cm<sup>2</sup>) : 4.467E+005  
 Dose (rad) : 1.488E+002  
 Live time (s) : 300.45  
 Dead time (s) : 10  
 Average flux (ions/(cm<sup>2</sup>s)) : 1.487E+003  
 Average flux error (%) : 0.24  
 Overall uniformity (%) : 91  
 Overall central shift (%) : 6  
 Calibration factor : 1.01758

DUT X coordinate : 0.295 in  
 DUT Y coordinate : -0.119 in  
 DUT Z coordinate : -17.016 cm  
 DUT tilt angle : 0.000 deg  
 Roll angle : -82.225 deg  
 Unused coordinate : 0.100 in  
 Selected Al degrader number : -0.000 steps  
 Degradation rotation angle : 0.000 deg  
 Detector bias (V) : 361 311 331 361 331

Layer summary:

silicon ROT 0 um  
 aramica ROT 1 mil  
 air gas ROT 60 mm

Run number : 19  
 Run file name : Montana Mar 2012.#0i  
 Run start date and time : 12/03/06 15:04:58  
 Run end date and time : 12/03/06 15:12:40  
 Duration of the run : 00:07:42 (+ 0 days)  
 Number of events : 0

Selected beam : 24.8 MeV/u Kr  
 Al degrader thickness (mil) : 0.000  
 Number of layers (layer file name) : 3 (MSU\_60)  
 Beam energy (MeV/amu) : 21.8  
 Beam energy (MeV) : 1830  
 Target material : silicon  
 Nominal LET (MeVcm<sup>2</sup>/mg) : 20.8  
 Nominal range (um) : 278.4  
 Effective LET (MeVcm<sup>2</sup>/mg) : 20.8  
 Effective range (um) : 278.4  
 DUT location : In-air  
 Position set name : Current

Effective fluence (ions/cm<sup>2</sup>) : 3.491E+005  
 Dose (rad) : 1.163E+002  
 Live time (s) : 278.583  
 Dead time (s) : 176.917  
 Average flux (ions/(cm<sup>2</sup>s)) : 1.253E+003  
 Average flux error (%) : 0.27  
 Overall uniformity (%) : 92  
 Overall central shift (%) : 4  
 Calibration factor : 1.0344

DUT X coordinate : 0.295 in  
 DUT Y coordinate : -0.119 in  
 DUT Z coordinate : -17.016 cm  
 DUT tilt angle : 0.000 deg  
 Roll angle : -82.225 deg  
 Unused coordinate : 0.100 in  
 Selected Al degrader number : -0.000 steps  
 Degradation rotation angle : 0.000 deg  
 Detector bias (V) : 361 311 331 361 331

Layer summary:

silicon ROT 0 um  
 aramica ROT 1 mil  
 air gas ROT 60 mm

APPENDIX E

RADIATION TESTING PLOTS

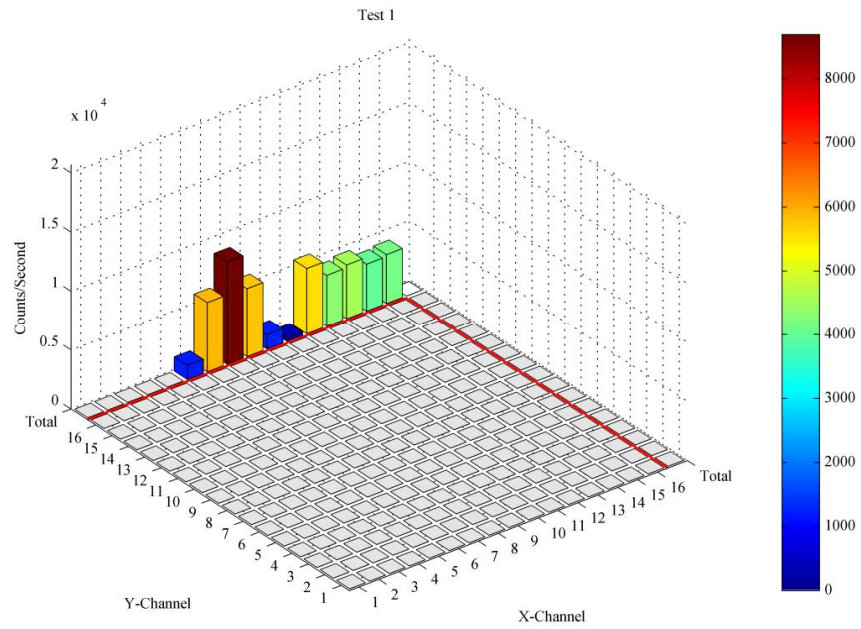


Figure E.1 Test #1 counts (125 mil aperture aimed at middle).

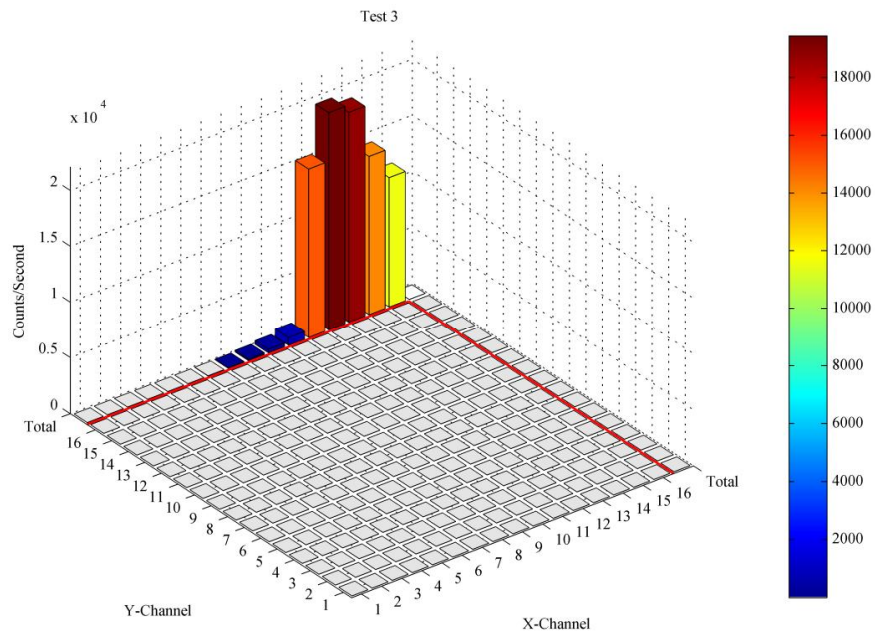


Figure E.2 Test #3 counts (125 mil aperture aimed at the right side, middle).

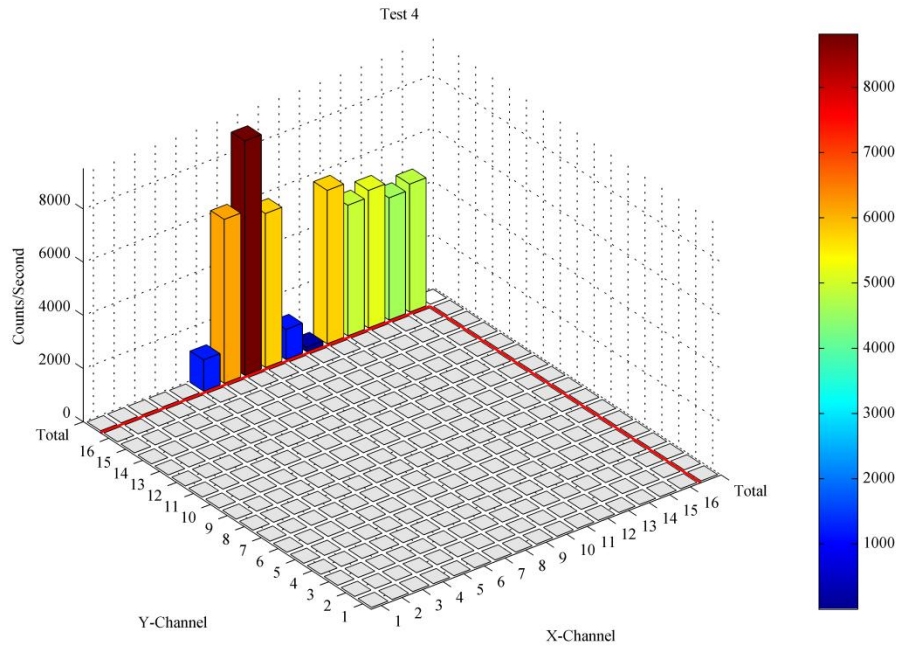
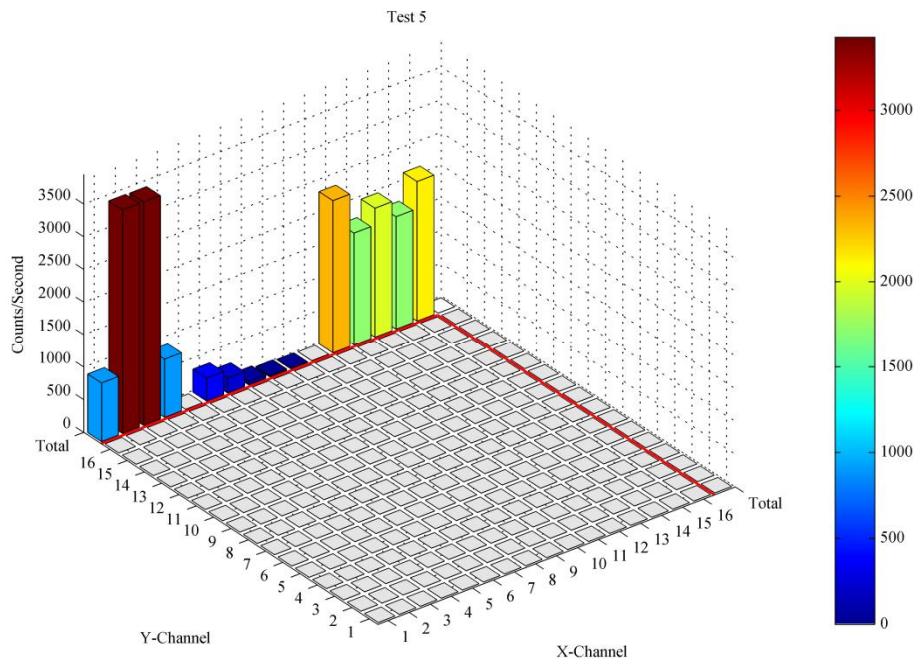


Figure E.3 Test #4 counts (125 mil aperture aimed at the bottom middle).



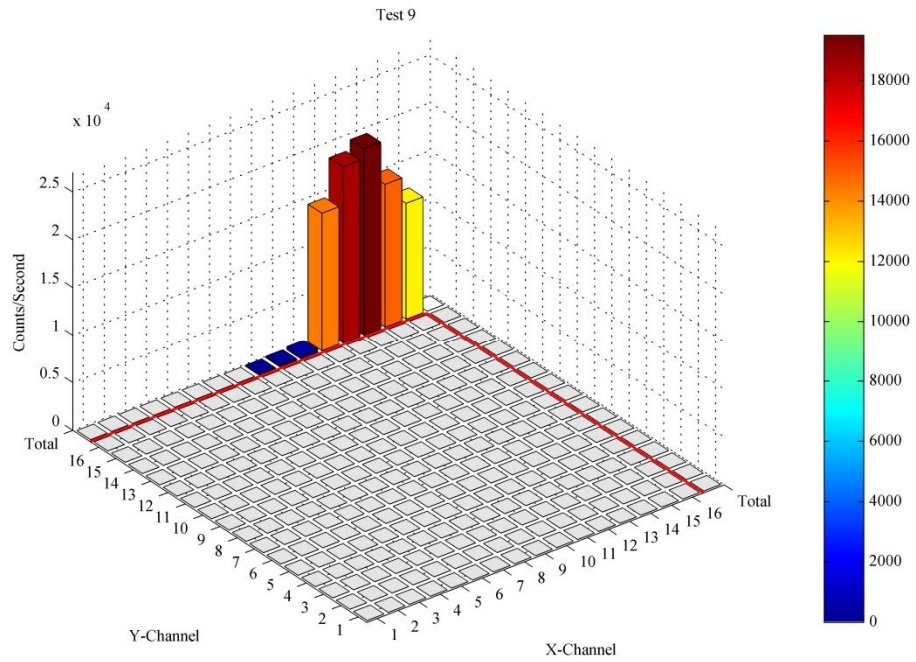


Figure E.5 Test #9 counts (125 mil aperture aimed at the lower right corner).

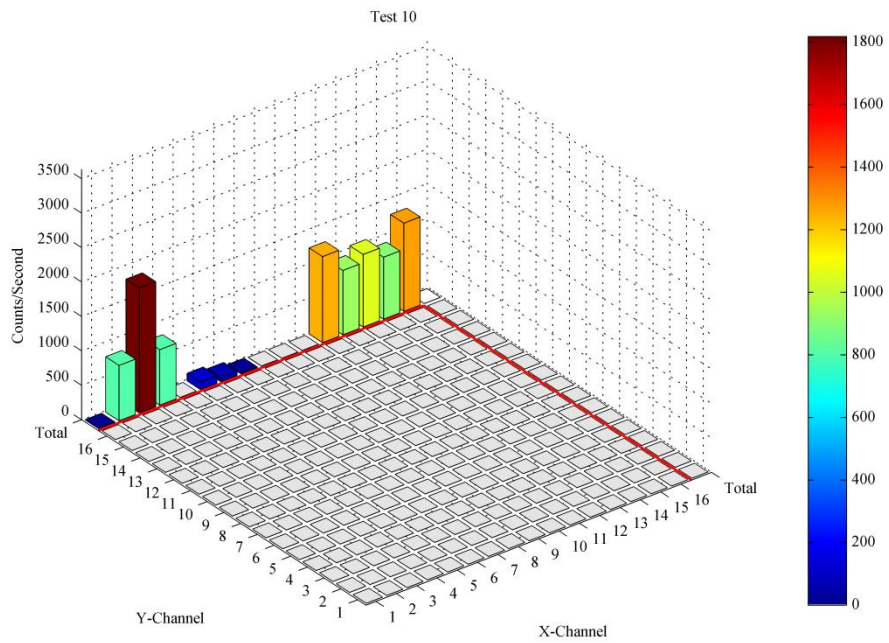


Figure E.6 Test #10 counts (125 mil aperture aimed at the lower left corner).

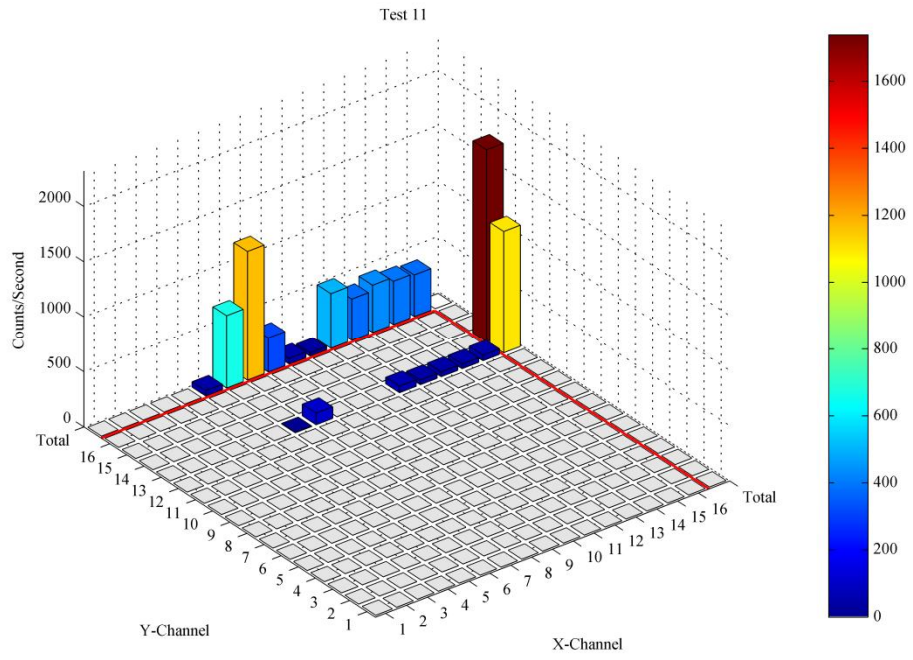


Figure E.7 Test #11 counts (40 mil aperture aimed at the middle).

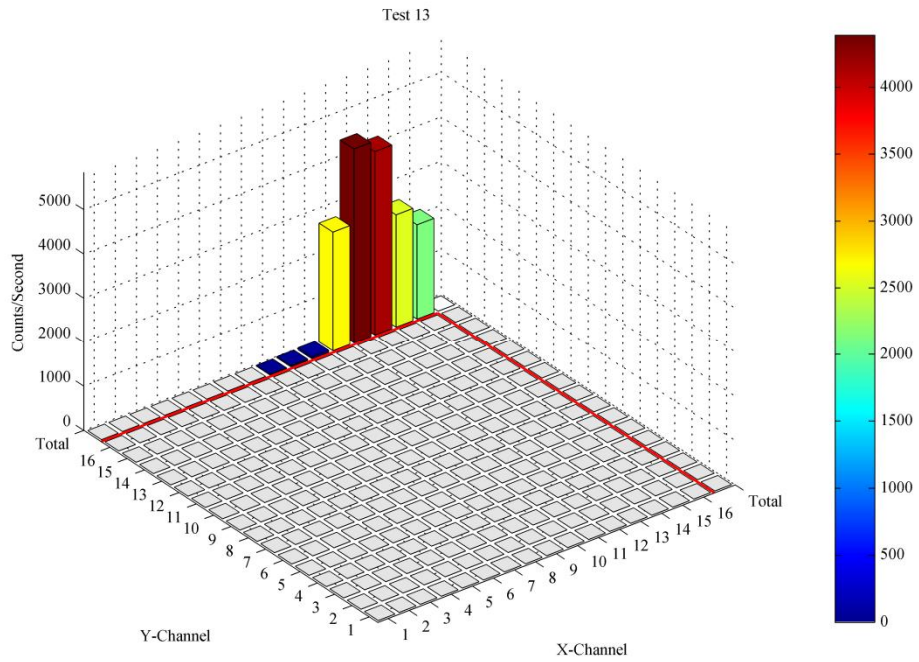
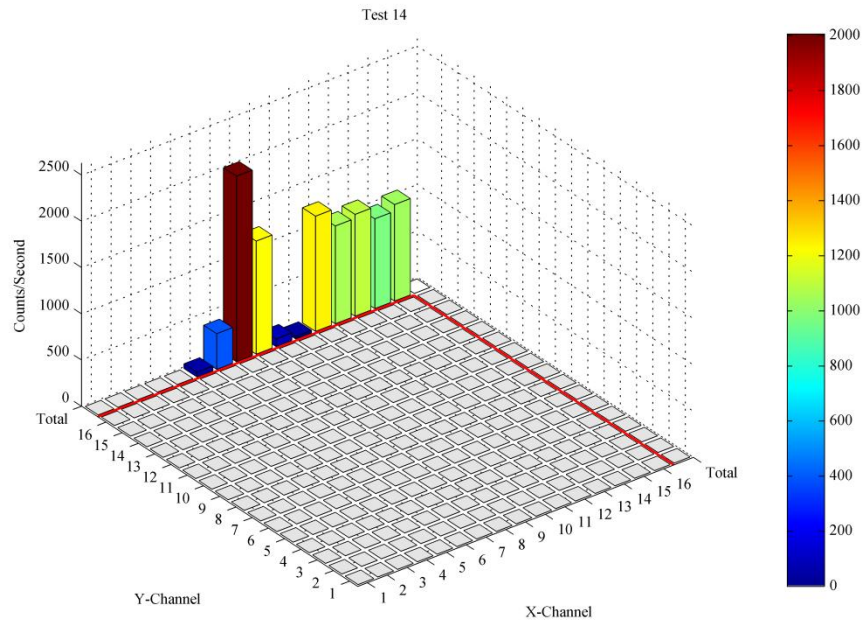


Figure E.8 Test #13 counts (40 mil aperture aimed at the right side middle).



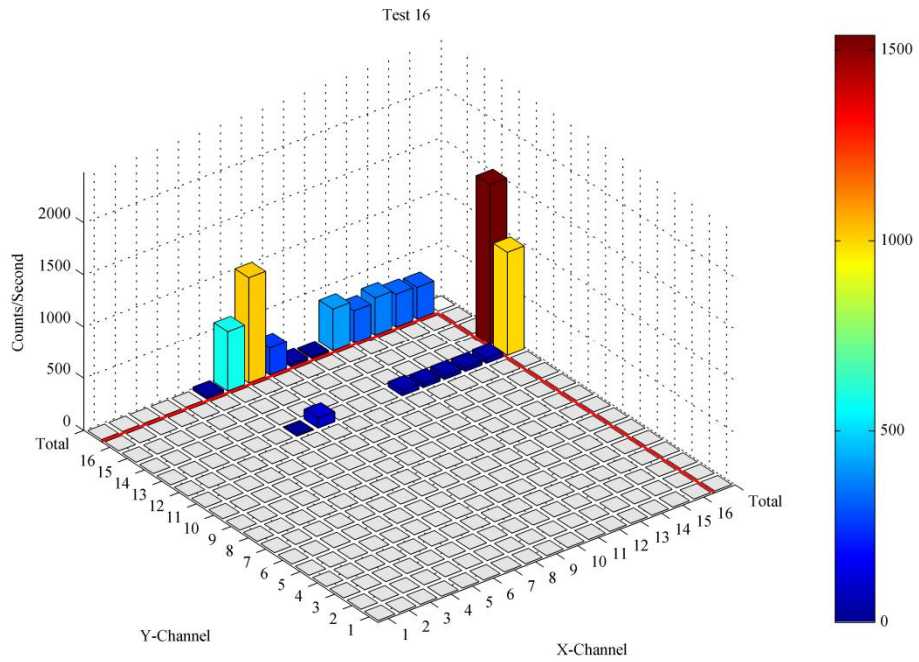


Figure E.11 Test #16 counts (40 mil aperture aimed at the top middle).

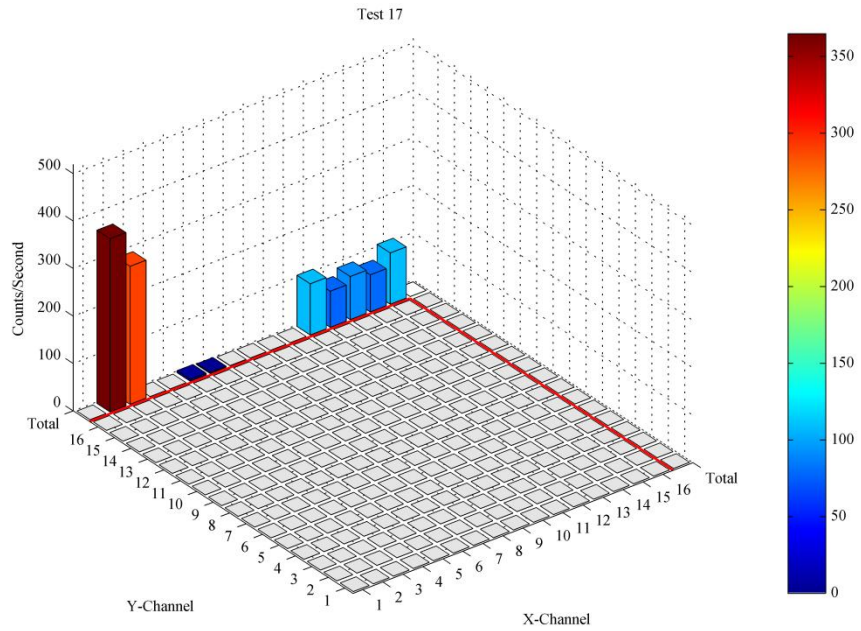


Figure E.12 Test #17 counts (40 mil aperture aimed at the left side middle).

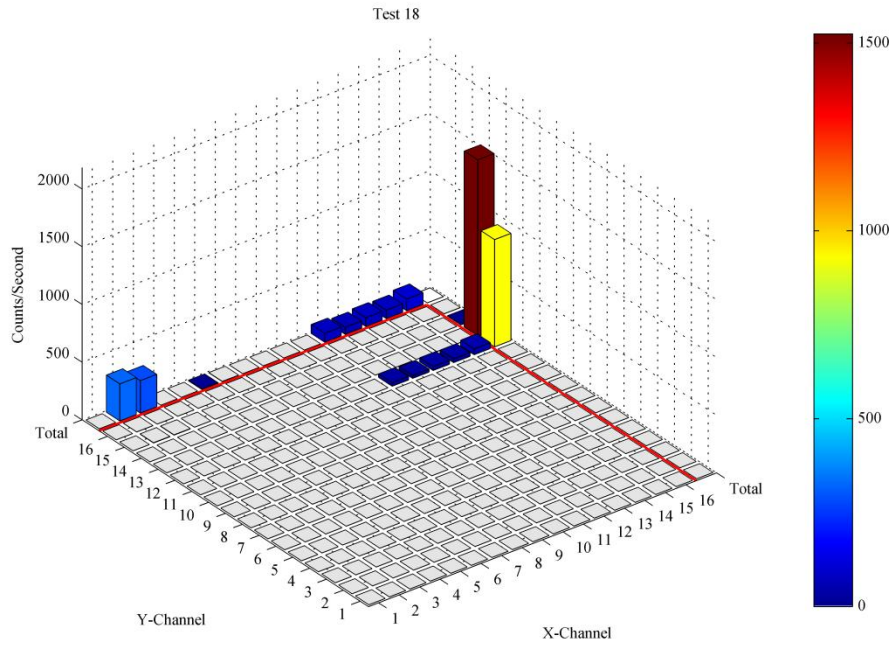


Figure E.13 Test #18 counts (40 mil aperture aimed at the top left corner).

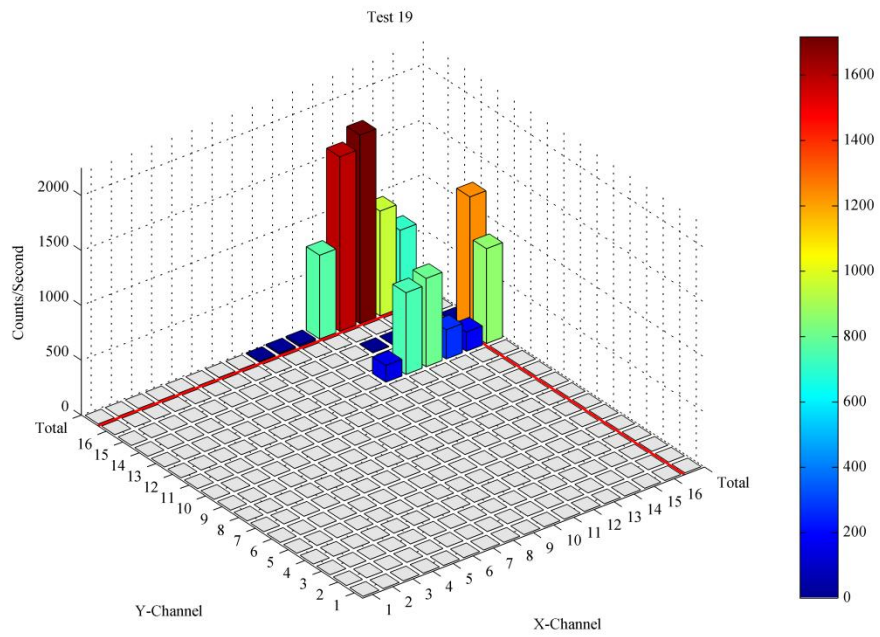


Figure E.14 Test #19 counts (40 mil aperture aimed at the top right corner).